Some Magnetic Reflections on Wave Dynamics

Alexy D. Karenowska
Magdalen College
University of Oxford

A thesis submitted for the degree of

Doctor of Philosophy

Hilary Term 2011

Acknowledgements

Some very special thanks are due.

Firstly, to my supervisor Prof. John Gregg for his enthusiasm, support, and confidence. And for the many opportunities he has given me over what have been a little over three years of quite spectacularly rewarding good fun.

To Prof. Dr. Burkard Hillebrands whose inspiration, warmth, and generosity has been so instrumental in shaping my research and my future.

To the Hillebrands group at the University of Kaiserslautern. A more welcoming group of people I could not hope to meet. Most especially, I would like to thank Dr. Andrii Chumak and Dr. Oleksandr Serga from whom I have learned so much over the last eighteen months.

To Prof. Andrei Slavin, Dr. Mikhail Kostylev, and Dr. Vasil Tiberkevich for their particular support in connection with all things magnonic crystal.

To Prof. Stephen Blundell, my head of Sub-department, for his support and guidance.

To Dr. Geoffrey Brooker for some of the most illuminating cups of coffee I have had the good fortune to drink.

And finally, to my parents and to T.K. There is no scale big enough to measure my gratitude to these three people.

Alexy Karenowska, March 2011.

To the memory of A. and I. L. Davison, and the ducks.

Some Magnetic Reflections on Wave Dynamics

A thesis submitted for the degree of Doctor of Philosophy

Alexy D. Karenowska, Magdalen College

Hilary Term 2011

Abstract

This thesis reports on two recent results in the fields of experimental spin- and general wave dynamics.

Chapter 1 presents an introduction to the dynamics of magnetostatic spin waves: propagating microwave-frequency magnetic disturbances which can be observed in ordered magnetic materials.

Chapter 2 builds on the general theoretical description of magnetostatic spin-wave propagation considered in chapter 1 to present a detailed technical background to the experimental investigations at the core of the thesis. The experimental materials and techniques employed are discussed, and the magnonic crystal—the spin-wave embodiment of a general type of wave transmission structure known as an artificial crystal—is introduced.

Chapter 3 describes an experimental investigation concerning spin-wave self-oscillators or 'active rings'. In the work, a spin-wave active ring incorporating a magnonic crystal is considered. It is demonstrated that the ring can be forced to excite preferentially at a mode determined by—and therefore readily predicted from—the geometrical properties of the crystal.

Chapter 4 describes an entirely general mechanism of spectral conversion and time reversal (that is, the conversion between a time-dependent signal $A(t)$ and a time-reversed version of that signal $A(-t)$) in a dynamic artificial crystal system. The physical basis of the mechanism is discussed, and theoretical predictions are shown to be in agreement with experimental measurements performed using a dynamic magnonic crystal.

Concluding remarks are presented in a final short chapter, chapter 5.

Contents

Preface

Notation

Throughout the text, vectors are represented by bold italic Latin characters ($\boldsymbol{a}$), unit vectors by bold upright hatted Latin characters ($\hat{\mathbf{a}}$), matrices by bold upright capital Latin characters ($\mathbf{A}$), and tensor quantities by bold upright Greek letters ($\boldsymbol{\alpha}$). The symbol $\mathbf{I}$ is reserved for the identity matrix, the symbol $\boldsymbol{r}$ for the general position vector $\boldsymbol{r} = x\hat{\mathbf{i}} + y\hat{\mathbf{j}} + z\hat{\mathbf{k}}$, and the symbol $\boldsymbol{k}$ for wavevector $\boldsymbol{k} = k_x\hat{\mathbf{i}} + k_y\hat{\mathbf{j}} + k_z\hat{\mathbf{k}}$ (so that the wavenumber $k = \sqrt{k_x^2 + k_y^2 + k_z^2}$).

Where Cartesian co-ordinates are used, unit vectors in the x-, y-, and z-directions are denoted by $\hat{\mathbf{i}}$, $\hat{\mathbf{j}}$, and $\hat{\mathbf{k}}$. In cylindrical and spherical co-ordinates, the elevation angle θ (unit vector $\hat{\boldsymbol{\theta}}$) is measured increasing from Oz to the xy plane, the azimuthal angle φ (unit vector $\hat{\boldsymbol{\varphi}}$) from O$x$ to Oy.

To $\boldsymbol{B}$ or to $\boldsymbol{H}$: A prefatory note

The spin waves described in the following are small-signal magnetic excitations which propagate in magnetically ordered materials.

When describing spin-wave systems we have a choice: we can do so in terms of magnetic flux density $\boldsymbol{B}$, or magnetic field $\boldsymbol{H}$. The two quantities are related by $\boldsymbol{B} = \mu_0 (\boldsymbol{H} + \boldsymbol{M})$ where μ_0 is the permeability of free space, and $\boldsymbol{M}$ the magnetization vector in the region over which $\boldsymbol{B}$ acts. In materials having no spontaneous magnetization (i.e. $\boldsymbol{M} = 0$ for $\boldsymbol{H} = 0$[1]) the expression above can also be written $\boldsymbol{B} = \mu_0 (\mathbf{I} + \chi_\mathrm{m}) \boldsymbol{H}$, where χ_m is the magnetic susceptibility tensor.

The form of the relation between $\boldsymbol{B}$, $\boldsymbol{H}$, $\boldsymbol{M}$, and χ_m is a vestige of the early days of magnetism when $\boldsymbol{H}$ was thought of as a field which arose from and acted on magnetic 'poles', in much the same way an electric field is created by and influences charges (c.f. $\boldsymbol{D} = \epsilon_0 \boldsymbol{E} + \boldsymbol{P} = \epsilon_0 (\mathbf{I} + \chi_\mathrm{e}) \boldsymbol{E}$, where $\boldsymbol{E}$ is electric field, $\boldsymbol{D}$ electric displacement, χ_e electrical susceptibility, and $\boldsymbol{P}$ polarization). Our modern understanding of magnetic fields as phenomena brought about by moving charges makes it more natural to treat $\boldsymbol{B}$ as the fundamental field quantity (in other words, to draw a parallel between $\boldsymbol{B}$ and $\boldsymbol{E}$, not $\boldsymbol{H}$ and $\boldsymbol{E}$). In view of this, it might be argued that we should use $\boldsymbol{B}$ and not $\boldsymbol{H}$ as the independent variable in any analysis of a magnetic system. Unfortunately however, if we do so we find that since magnetic susceptibility relates $\boldsymbol{H}$ and $\boldsymbol{M}$, not $\boldsymbol{B}$ and $\boldsymbol{M}$, in all but the trivial case of $\chi_\mathrm{m} = 0$, considerable mathematical awkwardness can result.

In what follows we adopt a position of compromise: we specify the magnetic fields which we *apply to* magnetic samples in terms of $\boldsymbol{B}$ and, unless to do so would compromise clarity, refer to $\boldsymbol{B}$ as 'magnetic field'. However, where we are concerned with descriptions of magnetic environments *inside* magnetic samples which involve manipulations of non-trivial susceptibility tensors, we put aside progressive sentiments in the interests of mathematical elegance, and work in terms of $\boldsymbol{H}$.

[1]For elucidation see Eqn. (1.1), page 10.

Fundamental constants

c	speed of light in free space	$3 \times 10^{8}\,\mathrm{m\,s^{-1}}$
e	proton charge	$1.6022 \times 10^{-19}\,\mathrm{C}$
q_{e}	electron charge	$-1.6022 \times 10^{-19}\,\mathrm{C}$
m_{e}	electron rest mass	$9.109 \times 10^{-31}\,\mathrm{kg}$
h	Planck's constant	$6.626 \times 10^{-34}\,\mathrm{J\,s}$
$\hbar = h/2\pi$		$1.0546 \times 10^{-34}\,\mathrm{J\,s}$
k_{B}	Boltzmann's constant	$1.3807 \times 10^{-23}\,\mathrm{J\,K^{-1}}$
ϵ_0	permittivity of free space	$8.854 \times 10^{-12}\,\mathrm{F\,m^{-1}}$
μ_{B}	Bohr magneton	$9.274 \times 10^{-24}\,\mathrm{A\,m^{2}}$ (or $\mathrm{J\,T^{-1}}$)
μ_0	permeability of free space	$4\pi \times 10^{-7}\,\mathrm{H\,m^{-1}}$

Introduction

> The investigation of the truth is in a way difficult and in a way easy. An indication is that no one can worthily reach it nor does everyone completely miss it ... but the difficulty of grasping the whole and not merely a part shows how difficult it is. And perhaps its difficulty exists in two ways, not in the things but in us as responsible for them. For just as bats' eyes are towards daylight, so in our soul is the mind towards those things that are clearest of all.

Aristotle, *The Metaphysics*, Trans. H. Lawson-Tancred, (1998).

This thesis is concerned with wave dynamics in magnetic systems. More specifically, it focuses on aspects of the dynamics of spin-wave signals: magnetic excitations which propagate at microwave frequencies in magnetically ordered materials.

The study of spin waves in magnetic thin films and nanostructures—a field which has latterly come to be known as magnonics[2] [1]—provides a valuable window into the underlying mechanisms of static and dynamic magnetism and is increasingly widely recognized as an area of science with much to contribute to the technological aspirations of spintronics [1–3]. Spintronics [3–7], or 'spin-transfer electronics', is the field of research devoted to the realization of new or enhanced electronic functionality

[2] After the spin-wave quantum, the magnon.

through the use of 'spin'—the quantum mechanical currency of magnetism—to code, store, and transfer information. The advance of spintronic technologies reliant on the injection and transport of spin-polarized charge currents is obstructed by the short spin diffusion lengths which typify metal and semiconductor systems [3–5,8]. The spin wave's ability to carry spin angular momentum over macroscopic distances without charge transfer potentially gives life to a new generation of spintronic devices which operate with complete freedom from this constraint. Moreover, the relatively slow group velocities of spin waves (typically of order one ten-thousandth of the speed of light) and their short wavelengths (nanometres to centimetres) make them well suited to the demands of nanoscale device development [9, 10].

However, above and beyond its status as an interesting piece of *spin* physics; the spin wave is also a very special manifestation of *wave* physics. In comparison with the waves which inhabit more familiar physical domains, for example light, radio waves, and acoustic vibrations, the dynamic properties of spin waves propagating in thin-film magnetic systems are singularly unusual. The dispersion characteristics of the waves show pronounced directional anisotropy, and can be radically modified via the application of small magnetic fields. Moreover, non-linear dynamic effects can be produced at power levels many orders of magnitude below those required for observing the corresponding phenomena elsewhere.

At the core of this thesis are two experimental investigations. Though independent and self-contained, both involve aspects of wave dynamics in thin-film spin-wave transmission systems incorporating structures known as magnonic crystals. A magnonic crystal is a spin-wave 'artificial crystal'; a man-made magnetic structure which features an 'artificial lattice' formed by mesoscale spatially periodic modulations in its magnetic properties. In describing the results of these investigations we hope to bring into focus their relevance both as specific developments in the field of spin-wave dynamics and magnonics, and, more generally, as illustrations of the mind broadening perspective on the wave paradigm which—through its eccentricities—the spin wave has to offer us.

The thesis is divided into five chapters. Chapter 1 considers the general theory of spin-wave propagation in thin-film magnetic systems. Building on this background, chapter 2 presents a technical introduction to the experimental studies presented in chapters 3 and 4. Chapter 5—a short concluding chapter—briefly reviews the work as a whole.

Chapter 1

Principles of magnetostatic spin-wave dynamics

Introduction

A spin wave is an eigenexcitation of the electronic spin lattice of a magnetically ordered solid.[1] The spin-wave quasi-particle—the magnon—is a boson which carries a quantum of energy $\hbar\omega$ and possesses a spin $\hbar$.

Incoherent, thermal spin-wave excitations exist in any magnetically ordered system with a temperature above absolute zero. The phenomena at the focus of this thesis however are not thermal spin waves, but externally excited spin-wave *signals*: coherent magnons which propagate over distances which are large in comparison with their characteristic wavelength. Our particular concern is the propagation of magnetostatic[2] spin waves in thin-film ferri- and ferromagnetic media.[3]

[1] In fact the term 'spin wave' is used in connection with several classes of magnetic excitation. This thesis is concerned with *electronic* spin waves. Although there is some conceptual overlap between these excitations and other dynamic magnetic phenomena to which the spin-wave label is applied—for example nuclear spin waves [11], and the spin excitations which arise from quantum symmetries in low-dimensional magnetic systems [12]—their underlying physics is distinct.

[2] The use of this term can be a source of confusion since the description magneto*static* seems in direct conflict with the concept of a magnetic *wave*. The term is really a shorthand for 'almost-magnetostatic'. As will be discussed in this chapter, magnetostatic spin waves are small-signal variations in the magnetization of a magnetic material.

[3] For absolute clarity a few extra words should be said. As will be discussed in §1.5, the elect-

In this first chapter, we provide an introduction to the physics of magnetostatic spin waves: small-signal microwave-frequency magnetic excitations with dynamics governed by the magnetic dipolar interaction. We begin by identifying the particular subset of magnetic environments which support their propagation, progress through a general discussion of their dynamics, and finally consider the specificities of their dispersion in thin-film magnetic systems.

1.1 The manifestation of magnetism

All materials belong to one of two magnetic camps: those which do not contain atoms, ions, or molecules with permanent magnetic moments, and those which do. Those which do may sub-divided into two further groups according to whether or not their permanent moments order spontaneously,[4] that is, even without encouragement from an applied magnetic field. A final level of detail categorizes the small group of materials which exhibit spontaneous magnetic order according to the particular form that this order takes.

Magnetism in meso- and macroscopic pieces of solid material is an electronic conspiracy. Although protons and neutrons—and therefore atomic nuclei—possess magnetic moments, those which arise from the orbital and spin angular momenta of electrons are approximately three orders of magnitude larger and are the driving force behind all types of long-range magnetic order.

Electronic magnetism (henceforth, 'magnetism') is a symptom of quantum mechanical correlations which exist between electron spin states. Permanent magnetic moments are associated with systems of atoms or molecules which, when assembled,

ronic spin-wave spectrum is traditionally divided into two: a short-wavelength region of waves with dynamics dominated by the magnetic exchange interaction and longer-wavelength band of dipolar waves. In the past, some considered only the first category of exchange-dominated excitations to be true 'spin waves' and used the term 'magnetostatic waves' to describe the second. Here—in line with modern convention—we treat both as fully paid-up members of the spin-wave club and refer to the latter class as 'magnetostatic spin waves'.

[4] Below a certain critical temperature.

have electronic configurations that include unpaired electrons; that is, electrons possessing a spin and/or orbital angular momentum which is not compensated by a partner electron of the opposite spin. However, the interplay between the electronic structure of real magnetic materials and their magnetic properties is one of formidable complexity. If we wish to model the magnetic behaviour of a new material there is no universal theory of electronic magnetism to which we can appeal. Instead, we must intuit—or else try to deduce—which of a number of possible approaches is most appropriate.

Conceptually, we can make a clear distinction between two different accounts (or models) of permanent magnetic-moment formation in magnetic substances. In the local-moment account, the permanent moments are those of spatially localized electrons which can be considered to 'belong' to individual orbital energy levels of specific atoms. Band magnetism on the other hand, involves the moments of spatially delocalized[5] itinerant electrons which occupy not distinct energy levels, but interaction-broadened energy bands. As we might anticipate, the band model is of greatest relevance to metallic and intermetallic systems, while the local-moment picture is widely applicable to magnetic insulators. However, the two models are by no means mutually exclusive, making a neat division of magnetic substances into 'band' and 'local-moment' types impossible.[6]

The spin waves which interest us are particular to magnetic systems containing permanent magnetic moments. Fortunately for the spin-wave dynamicist, the overwhelming majority of spin-wave phenomena[7] can be understood using models of the magnetic materials in which they propagate which hold independently of the mechanism by which their magnetic moments arise from their electronic structure.

[5] Or at least imperfectly spatially localized.

[6] For very readable introductions to the origins of electronic magnetism, the reader is referred to Refs. [13] and [14].

[7] That is, phenomena related to the dynamics of propagating, externally excited spin-wave signals.

1.1.1 Describing the behaviour of magnetic materials

As a first step toward an understanding of the spin wave, we identify the formalisms used to quantify and categorize electronic magnetism and magnetic order.

The magnetic moment per unit volume or magnetization $\boldsymbol{M}$ of a material subject to a magnetic field[8] $\boldsymbol{H}$ is determined by its spontaneous magnetization $\boldsymbol{M}_{\mathrm{sp}}$ and its magnetic susceptibility $\boldsymbol{\chi}_{\mathrm{m}}$,

$$\boldsymbol{M} = \boldsymbol{M}_{\mathrm{sp}} + \boldsymbol{\chi}_{\mathrm{m}}\boldsymbol{H}, \tag{1.1}$$

where $\boldsymbol{M}$, $\boldsymbol{H}$, and $\boldsymbol{M}_{\mathrm{sp}}$ are three dimensional vectors, and $\boldsymbol{\chi}_{\mathrm{m}}$ is a 3×3 tensor. Magnetic field, magnetization, and magnetic flux density $\boldsymbol{B}$ are related by

$$\boldsymbol{B} = \mu_0 \left(\boldsymbol{H} + \boldsymbol{M}\right), \tag{1.2}$$

where $\mu_0 = 4\pi \times 10^{-7}\,\mathrm{H\,m^{-1}}$ is the permeability of free space. Equation (1.2) can also be written

$$\boldsymbol{B} = \boldsymbol{\mu}\boldsymbol{H}, \tag{1.3}$$

where $\boldsymbol{\mu}$ the permeability tensor which for $\boldsymbol{M}_{\mathrm{sp}} = 0$ is given by

$$\boldsymbol{\mu} = \mu_0 \left(\mathbf{I} + \boldsymbol{\chi}_{\mathrm{m}}\right). \tag{1.4}$$

In general, the magnetic response of a piece of magnetic material is both directionally dependent and non-linear; in other words, the susceptibility tensor is asymmetric and its elements vary with $\boldsymbol{H}$.

When considering the origins and implications of asymmetry in $\boldsymbol{\chi}_{\mathrm{m}}$ it is helpful to distinguish between two sources: intrinsic asymmetry, and that which (as a consequence of the aforementioned non-linearity) may be brought about by an applied $\boldsymbol{B}$.

Intrinsic asymmetry in $\boldsymbol{\chi}_{\mathrm{m}}$ arises from the fact that the energy required to magnet-

[8] See prefatory note, pages 1–2.

ize a magnetic sample is influenced by its shape and underlying magnetic structure. The difference between the energy required to align $\boldsymbol{M}$ parallel to the directions associated with highest and lowest energy expenditures (the 'hard' and 'easy' axes respectively) is termed the magnetic anisotropy energy.

The total magnetic anisotropy energy is commonly dominated by two contributions: magnetocrystalline anisotropy and shape anisotropy. Magnetocrystalline anisotropy is related to the atomic- or molecular-scale geometry of the material from which a magnetic sample is composed; for example, almost all crystalline materials have a susceptibility which depends on the direction of the applied magnetic field relative to the crystal axes. Shape anisotropy on the other hand arises from any effect (e.g. through boundary conditions) of the macroscopic structure (e.g. thin film, sphere, or cube) of the sample on its $\boldsymbol{M}$ or internal field. In certain materials and/or geometries, the anisotropy energy can also be influenced by factors such as surface effects [15] and/or externally applied strains and stresses.

In principle, we can incorporate intrinsic anisotropy into a model of a magnetic sample directly via the susceptibility tensor. However, in practice it is often preferred to perform the accounting using anisotropy fields: equivalent additive contributions to the total magnetic field vector $\boldsymbol{H}$. This approach has the advantage that changes in the geometry of the sample can be accommodated by modifying a three-dimensional vector, rather than the nine elements of a 3×3 tensor.

The second type of asymmetry in $\boldsymbol{\chi}_{\mathrm{m}}$ alluded to above—the field induced variety—plays a central role in the physics of spin-wave phenomena; we shall return to it later.

1.1.2 Classes of magnetic order

In the absence of anisotropy, the magnetization acquired by a magnetic material in response to an applied static uniaxial magnetic field is parallel to that field. When the amplitude of the field is small, the induced magnetization ΔM_0 is characterized

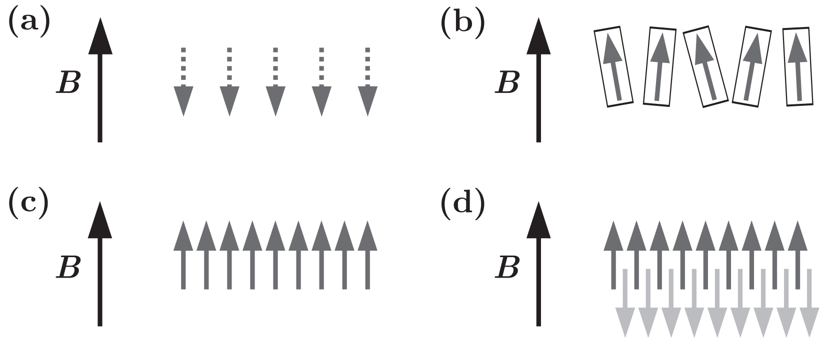

Figure 1.1: The magnetic characteristics of a material are dependent on the arrangement of and interaction between the magnetic moments of its constituent atoms, ions, or molecules, represented by the grey arrows in diagrams (a) to (d). (a) Diamagnetic materials do not contain permanent magnetic moments, their induced magnetization opposes an applied magnetic field. (b) Paramagnets contain permanent magnetic moments which do not spontaneously order, but will partially align with an applied magnetic field. (c) Ferromagnetic materials exhibit spontaneous long-range magnetic order, their magnetic behaviour can be understood with reference to a *spin lattice* of strongly coupled permanent magnetic moments. (d) Ferrimagnets, like ferromagnets, contain permanent magnetic moments and can be modelled in terms of a spin lattice comprising two anti-aligned sub-lattices. When the material is exposed to a magnetic field, the induced magnetic moments arising from these sub-lattices oppose and the resulting behaviour depends on their relative magnitude.

by a field-independent 'initial' susceptibility $\chi_{\mathrm{m0}} = \Delta M_0/\Delta H_0$.

Four general classes of magnetic behaviour may be identified with reference to the distinctions described in the first paragraph of §1.1 and the value of χ_{m0}:

- **Diamagnetism.** Materials which do not possess permanent magnetic moments are characterized by a negative initial susceptibility $\chi_{\mathrm{m0}} < 0$ and are known as diamagnets (Fig. 1.1(a)). Though quantum mechanical in origin, diamagnetism can be thought of as a microscopic manifestation of Lenz's law: in the presence of an applied magnetic field, the motion of electrons orbiting a material's atomic nuclei is perturbed in such a way as to produce a net opposing magnetization. Compared with other types of magnetism which involve the interplay between permanent magnetic moments, diamagnetism is a weak effect.

- **Paramagnetism.** Paramagnets contain permanent magnetic moments which do not spontaneously order but may be drawn into partial alignment by an applied magnetic field. Paramagnetic materials have a positive initial susceptibility $\chi_{\mathrm{m0}} > 0$ (Fig. 1.1(b)).

- **Ferromagnetism.** Ferromagnetic materials contain permanent magnetic moments which—below a certain critical temperature—exhibit spontaneous long-range order (Fig. 1.1(c)). The physical effect responsible for this order is the magnetic exchange interaction; a quantum mechanical phenomenon which emerges from the rules which govern the symmetries of overlapping electron wavefunctions. The magnetic behaviour of a ferromagnet can be thought of as arising from a *spin lattice* of strongly coupled permanent electronic moments. Like paramagnets, ferromagnets have a positive initial susceptibility ($\chi_{\mathrm{m0}} > 0$).

- **Ferrimagnetism.** Ferrimagnets, like ferromagnets, contain permanent magnetic moments, and can be understood with reference to a coupled spin lattice. The spin lattice of a ferrimagnetic material has a sub-structure comprising two anti-aligned sub-lattices[9] (Fig. 1.1(d)). The induced magnetic moments arising from these sub-lattices oppose and the resulting behaviour depends on their relative magnitude. In the special case of identical sub-lattices, no net moment results and the material is said to be antiferromagnetic.

It is magnetic systems which exhibit the final two classes of magnetic order described above: ferromagnets and (non-antiferromagnetic) ferrimagnets which provide the physical stage upon which the magnetostatic spin-wave phenomena that we shall consider play out.

[9] Note that true anti-alignment (i.e. sub-lattices whose magnetization vectors are π radians apart) is a special case. More generally, the local magnetization vectors of the sub-lattices are separated by some angle $\xi \leq \pi$. Lattice geometries vary from the simple case of two inter-locking cubic structures to complex symmetries in which the magnetizations of the sub-lattices twist along helical paths through the material.

1.2 The ferro- and ferrimagnetic spin-wave environments

As described in §1.1.2, the magnetic behaviour of ferro- and ferrimagnets can be understood with reference to a spin lattice of coupled permanent magnetic moments. In this section we shall explore the spin-lattice concept in more detail and use it to obtain a qualitative picture of spin-wave propagation.

1.2.1 The spin lattice

A spin lattice is a magnetic model of a ferro- or ferrimagnetic material comprising a three-dimensional array of magnetic moments. The symmetry of the lattice (i.e the spatial arrangement of the lattice sites) is determined by the physical structure of the particular material to which it corresponds. The moment associated with each lattice site may be that of a single electron (a 'spin'), or several (a 'macro-spin'). The moments on the spin lattice are coupled via two magnetic mechanisms: the dipolar interaction and the exchange interaction.

The exchange interaction is an orientation dependent contribution to the energy of coupled moments which comes about as a result of the restrictions imposed by quantum mechanics on the symmetries of overlapping electron wavefunctions. The strength of the exchange interaction is quantified in terms of a material dependent parameter known as the exchange stiffness.[10] Exchange is by far the dominant interaction between moments occupying adjacent sites on the spin lattice and underwrites its spontaneous magnetic order.

The dipolar interaction energy between two moments $\bar{\boldsymbol{\mu}}_i$ and $\bar{\boldsymbol{\mu}}_j$ separated by a

[10] The exchange stiffness has units of energy per unit length.

vector distance $\boldsymbol{R}_{ij}$ is given by

$$E_{\mathrm{d}} = \frac{\mu_0}{4\pi R_{ij}^3}\left(\bar{\boldsymbol{\mu}}_i \cdot \bar{\boldsymbol{\mu}}_j - \frac{3}{R_{ij}^2}\left(\bar{\boldsymbol{\mu}}_i \cdot \boldsymbol{R}_{ij}\right)\left(\bar{\boldsymbol{\mu}}_j \cdot \boldsymbol{R}_{ij}\right)\right).$$

This energy is small; as a guide, for moments of magnitude one Bohr magneton (a single electron dipole moment $\mu_{\mathrm{B}} = e\hbar/2m_{\mathrm{e}}$) separated by a distance of $1\,\text{Å}$, it is of order $10^{-23}\,\mathrm{J}$, which equates to roughly $1\,\mathrm{K}$ in temperature. However, in comparison with the exchange interaction, which is generally only significant between nearest-neighbour lattice sites, the dipolar interaction is a relatively long-range effect. The magnetostatic spin-wave excitations of interest to us have wavelengths which are approximately five orders of magnitude larger than the characteristic dimension of the spin lattice. As a result, although the exchange interaction plays a crucial role in the organization of the magnetic environment in which the waves propagate, it is this dipolar interaction which dominates their dynamics.

1.2.2 Domain formation, magnetic saturation, and a qualitative description of the spin wave

In §1.1.1, we introduced magnetic anisotropy: a directional dependence in the energy expenditure associated with magnetizing a given piece of magnetic material. Were anisotropy the only cost consideration relevant to the magnetization process, we might expect all pieces of ferro- and ferrimagnetic material having finite anisotropy to spontaneously magnetize uniformly along their easy axis. However, a given orientation $\boldsymbol{M}$ also has an energy overhead by virtue of the magnetic field it produces outside of the material (Fig. 1.2(a)). In the absence of an applied or anisotropy field of sufficient strength to provide this energy, ferro- and ferrimagnets split into domains; mesoscopic regions of material having net magnetic moments oriented in different directions (Fig. 1.2(b)). Adjacent domains are separated by domain walls: narrow regions of

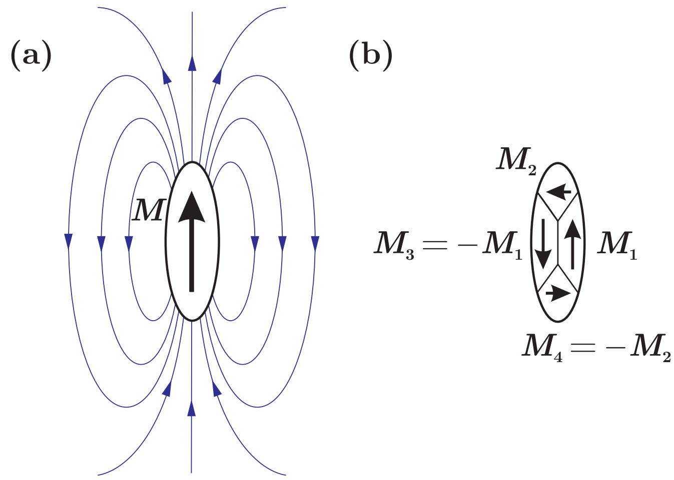

Figure 1.2: (a) A thin ellipsoidal sample of ferro- or ferrimagnetic material having negligible magnetocrystalline anisotropy has, by virtue of shape anisotropy, an easy direction along its major axis. However, the energy gain from spontaneous magnetization of the sample along this direction may be outweighed by the energy cost of the associated magnetic field. (b) In the absence of an applied or anisotropy field of sufficient strength to 'repay' the field energy associated with magnetization along its easy axis, a ferro- or ferrimagnet splits into domains: mesoscopic regions of material having net magnetic moments oriented in different directions. In the 'closure' type domain structure depicted here, the external field is reduced to zero.

material over which the magnetization vector rotates. There is a per-unit-area energy outlay associated with the formation of a domain wall which is dependent upon the magnetic anisotropy and exchange stiffness of the magnetic sample it inhabits; the balance between the domain-wall energy, the anisotropy energy, and the field energy determines the detailed domain structure.

If a sample of ferro- or ferrimagnetic material having negligible shape and magnetocrystalline anisotropies is exposed to a small static magnetic field B_{app},[11] its magnetic response parallel to the field direction is, as outlined in §1.1.2, characterized by an initial field-independent susceptibility $\chi_{\text{m}0}$. Under these conditions, the magnetization ΔM_0 acquired by the sample is due to a small reversible net growth in domains with moments oriented near-parallel to the applied field. If the amplitude of

[11] Note that B_{app} here is the magnetic flux density *applied* to the magnetic material which, depending on the geometry, may or may not be equal to the magnetic flux density B inside it.

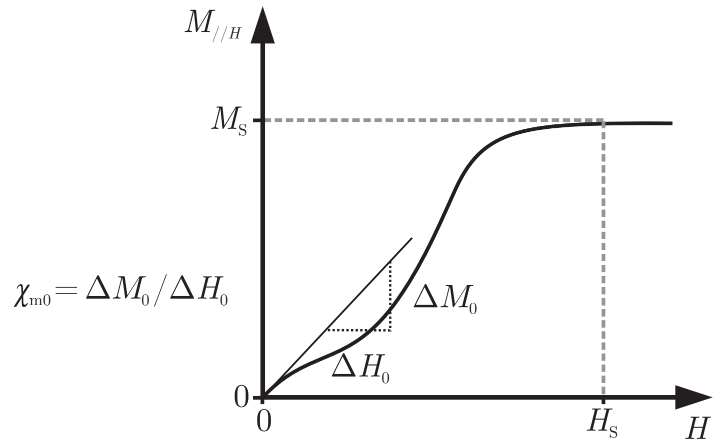

Figure 1.3: If a small uniaxial magnetic field B_{app} is applied to a sample of ferro- or ferrimagnetic material (see Fig. 1.1) having negligible shape and magnetocrystalline anisotropies, its magnetic response in the direction of the field is approximately linear, independent of B_{app}, and characterized by an 'initial' susceptibility $\chi_{m0} = \Delta M_0/\Delta H_0$. As B (and therefore H) inside the sample increases, energy consuming reorientation and reorganization of the domain structure occurs and the susceptibility is substantially modified from this initial value. Eventually a state of saturation $B = B_S$, $H = H_S$ is reached at which the material is mono-domained and has a magnetization M_S in the field direction. These conditions result in a small-signal magnetic response with a strong directional dependence.

B_{app} (and therefore of B and H inside the sample) is increased, the domain structure undergoes more significant transformation and the susceptibility becomes both substantially modified from the initial value, and strongly field-dependent. Eventually a condition of saturation $B = B_S$, $H = H_S$ is reached in which the material consists of a single domain. The net magnetization takes a maximum value M_S parallel to the field so that—though it remains finite in directions away from the direction of the applied field—the differential susceptibility $\mathrm{d}M/\mathrm{d}H$ along the field direction is reduced to zero. This is an example of the field-induced anisotropy in χ_m alluded to in §1.1.1. The corresponding state of the spin lattice is one in which—throughout the whole volume of the material—the moments on the lattice sites are aligned with the applied field.

The magnetostatic spin-wave signals with which we are concerned are perturbations to the magnetization of a magnetically saturated material. The waves are

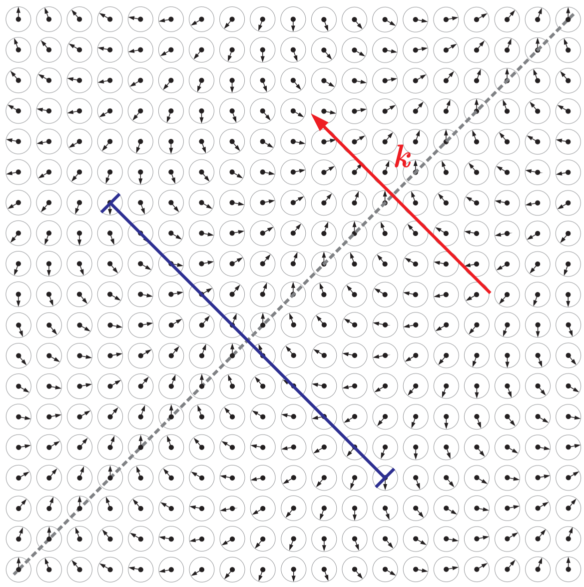

Figure 1.4: A magnetostatic spin-wave is a spatial and temporal variation in the phase of magnetic precession across a spin lattice. In this schematic the small arrowed dots represent precessing magnetic moments. The dotted grey line is a wavefront i.e. a line of constant phase. The blue bar indicates the spin-wave wavelength and the red arrow the direction of the wavevector $\boldsymbol{k}$.

characterized by small-signal variations in magnetization which can be described in terms of a precession of the magnetic moments on the spin lattice about the saturation direction. A bulk (or $k = 0$) magnetostatic spin-wave mode corresponds to a condition known as ferromagnetic resonance (FMR) characterized by in-phase precession of individual spins on the lattice sites about the applied magnetic field—i.e. a small-signal variation in the components of the magnetization perpendicular to the zero differential susceptibility direction. Finite k excitations are those in which the phase of the precession varies over the lattice. This concept is illustrated schematically in Fig. 1.4, where precessing moments are represented by small arrowed dots (note that the arrowed dots are not intended to represent individual sites on the spin lattice, were this the case the wavelength of the wave would be grossly under-represented).

1.3 Elementary magnetic dynamics

In the previous section we arrived at a qualitative description of a magnetostatic spin wave. Here, we move towards a description of its physics by examining the general principles of electron spin dynamics.

1.3.1 Single-spin dynamics

Questions about the dynamics of an isolated electron spin can only be meaningfully posed in the language of quantum mechanics. As we have established however, a spin wave is not a phenomenon associated with an isolated spin, but with the collective dynamics of a spin lattice: a large spin or macro-spin *ensemble*. This distinction allows us—provided we exercise a little caution—to describe a spin-wave excitation by treating each participant spin as a quasi-classical object. As well as providing a route to quantitative results which are consistent with physical reality, this approach also offers conceptual traction on a piece of physics which—when approached from a purely quantum mechanical perspective—presents a formidable challenge to our intuitions. In line with the standard treatment (see for example Ref. [16]), we shall compare the dynamics of a single electron spin having angular momentum $\boldsymbol{J}$ and a magnetic moment $\bar{\boldsymbol{\mu}}$ subject to a magnetic field $\boldsymbol{B}$, with those of a classical spinning top.

1.3.1.1 The spinning top

The rate of change of angular momentum of a mechanical spinning top of angular momentum $\boldsymbol{J}_\mathrm{t}$ (magnitude $|\boldsymbol{J}_\mathrm{t}| = J_\mathrm{t}$) is equal to the torque due to the effect of gravity $\boldsymbol{g}$ on its mass m

$$\boldsymbol{\tau}_\mathrm{t} = \frac{\mathrm{d}\boldsymbol{J}_\mathrm{t}}{\mathrm{d}t} = \boldsymbol{r} \wedge m\boldsymbol{g} \tag{1.5}$$

which has magnitude

$$\tau_\mathrm{t} = m|\boldsymbol{r}||\boldsymbol{g}|\sin\theta = mrg\sin\theta, \tag{1.6}$$

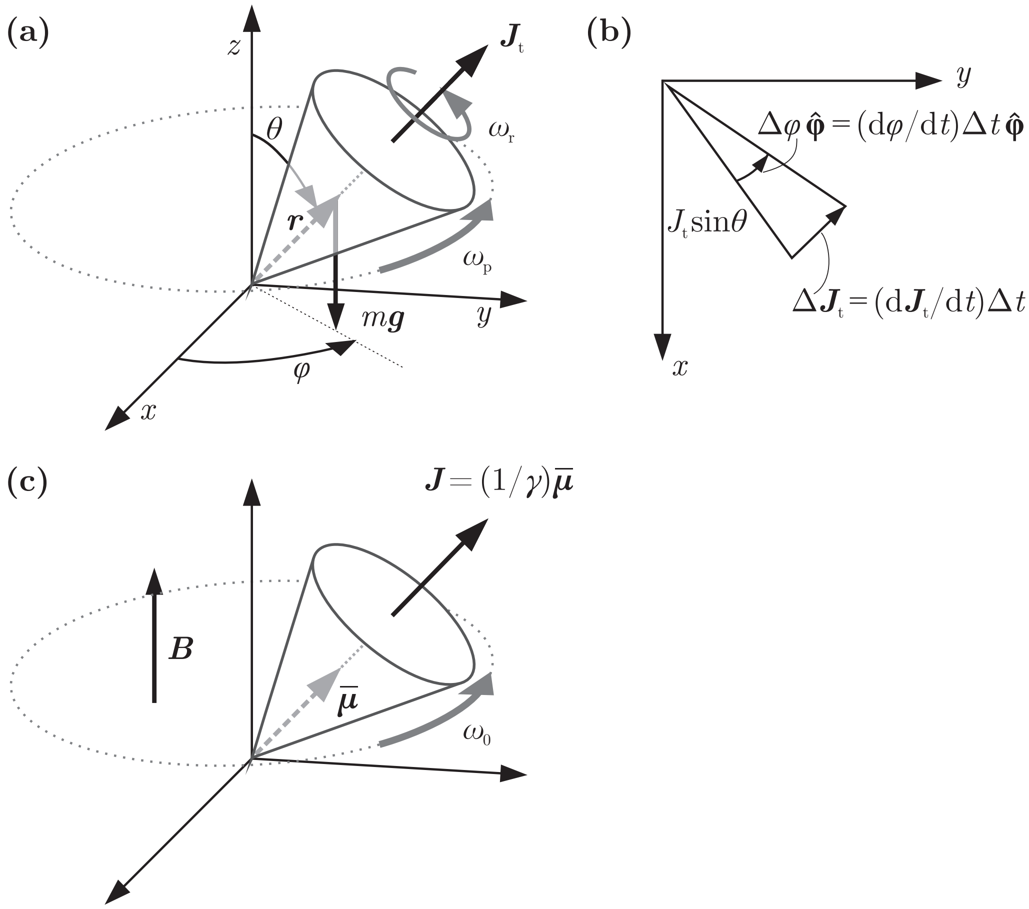

Figure 1.5: (a) A spinning top, mass m, represented by the conical volume in the diagram, experiences a force due to gravity $\boldsymbol{g}$ which acts vertically downward through its centre of mass. The centre of mass is located at a point identified by the vector $\boldsymbol{r}$ relative to the origin of the co-ordinate system. The top spins at an angular rate ω_r about its own axis and precesses about the z-axis at an angular frequency ω_p at a constant angle θ. The vector $\boldsymbol{r}$ is always parallel or antiparallel to the angular momentum vector of the top $\boldsymbol{J}_\mathrm{t}$. Both $\boldsymbol{J}_\mathrm{t}$ and $\boldsymbol{r}$ have constant magnitudes, constant z-components, and vary in x- and y- as $\sin\theta\cos\varphi$ and $\sin\theta\sin\varphi$ respectively. (b) The precessional frequency $\omega_\mathrm{p} = \mathrm{d}\varphi/\mathrm{d}t$ can be derived by considering how the system evolves in a small increment of time Δt. (c) In the magnetic case, the top in (a) is replaced by a magnetic moment $\bar{\boldsymbol{\mu}}$ having angular momentum $\boldsymbol{J}$. The moment experiences a torque $\bar{\boldsymbol{\mu}}\wedge\boldsymbol{B}$, under the influence of a magnetic field $\boldsymbol{B}$, and precesses at an angular frequency ω_0. The precession is clockwise (ω_0 negative) about the z-axis when the vectors $\bar{\boldsymbol{\mu}}$ and $\boldsymbol{J}$ are parallel (γ positive) and counter-clockwise (ω_0 positive) when they are antiparallel (γ negative).

where the vector $\boldsymbol{r}$ (length r) is between the origin of the co-ordinate system and top's centre of mass, and the angle θ is that between $\boldsymbol{r}$ and the vertical (Fig. 1.5(a)). Considering the evolution of the system in a small increment of time Δt, we can relate $\mathrm{d}\boldsymbol{J}_{\mathrm{t}}/\mathrm{d}t$ to the top's precessional frequency $\omega_{\mathrm{p}} = \mathrm{d}\varphi/\mathrm{d}t$ with the aid of the geometrical construction shown in Fig. 1.5(b)

$$\frac{\mathrm{d}\boldsymbol{J}_{\mathrm{t}}}{\mathrm{d}t} = J_{\mathrm{t}} \sin\theta \frac{\mathrm{d}\varphi}{\mathrm{d}t}\hat{\boldsymbol{\varphi}} \tag{1.7}$$

so that, from Eqns. (1.5) and (1.6),

$$\omega_{\mathrm{p}} = \frac{mrg}{J_{\mathrm{t}}}. \tag{1.8}$$

Since $\boldsymbol{J}_{\mathrm{t}}$ and $\boldsymbol{r}$ are either parallel or antiparallel, Eqn. (1.8) allows us to write Eqn. (1.5) in the form

$$\frac{\mathrm{d}\boldsymbol{J}_{\mathrm{t}}}{\mathrm{d}t} = \boldsymbol{\Omega}_{\mathrm{t}} \wedge \boldsymbol{J}_{\mathrm{t}}, \tag{1.9}$$

where

$$\boldsymbol{\Omega}_{\mathrm{t}} = \omega_{\mathrm{p}} \frac{\boldsymbol{r}\cdot\boldsymbol{J}_{\mathrm{t}}}{|\boldsymbol{r}\cdot\boldsymbol{J}_{\mathrm{t}}|}\hat{\mathbf{k}}.$$

1.3.1.2 The spinning spin quasi-top

In the magnetic case, we replace the real mechanical top of §1.3.1.1 by a 'spin quasi-top': a magnetic moment $\bar{\boldsymbol{\mu}}$ having angular momentum $\boldsymbol{J}$ under the influence of a magnetic field $\boldsymbol{B}$. As with the angular momentum and position vectors $\boldsymbol{J}_{\mathrm{t}}$ and $\boldsymbol{r}$ in the mechanical case, the vectors $\bar{\boldsymbol{\mu}}$ and $\boldsymbol{J}$ are always either parallel or antiparallel. The effects of gravity can be considered negligible, so that the total torque acting on the magnetic moment is

$$\boldsymbol{\tau} = \frac{\mathrm{d}\boldsymbol{J}}{\mathrm{d}t} = \bar{\boldsymbol{\mu}} \wedge \boldsymbol{B} = \gamma \boldsymbol{J} \wedge \boldsymbol{B}, \tag{1.10}$$

where γ is the gyromagnetic ratio ($\bar{\boldsymbol{\mu}} = \gamma \boldsymbol{J}$).

Following the treatment of the spinning top, we can derive an expression for the precessional frequency ω_0 of the moment

$$\omega_0 = -\gamma B \tag{1.11}$$

where $B = |\boldsymbol{B}|$. Equations (1.10) and (1.11) lead to

$$\frac{\mathrm{d}\boldsymbol{J}}{\mathrm{d}t} = \boldsymbol{\Omega} \wedge \boldsymbol{J} \tag{1.12}$$

where $\boldsymbol{\Omega} = -\gamma \boldsymbol{B}$. Comparing the results of the mechanical and magnetic analyses we note that in the magnetic case the precessional frequency ω_0 is solely determined by the magnetic field; it is independent of the angular momentum $\boldsymbol{J}$. This is due to the fact that, unlike the moment and momentum of the mechanical top, those of the spin system are linearly related.

1.3.1.3 Electronic momenta and the gyromagnetic ratio

The angular momentum $\boldsymbol{J}$ and magnetic moment $\bar{\boldsymbol{\mu}}$ of an electron are—as indicated in the analysis above—related by the gyromagnetic ratio γ,

$$\bar{\boldsymbol{\mu}} = \gamma \boldsymbol{J}. \tag{1.13}$$

In general, the angular momentum $\boldsymbol{J}$ of a bound electron has two components, an orbital contribution $\boldsymbol{L}$ (magnitude $L = |\boldsymbol{L}|$), and an intrinsic spin angular momentum $\boldsymbol{S}$ (magnitude $S = |\boldsymbol{S}|$). Orbital angular momentum is equivalent to the quasi-classical momentum

$$\boldsymbol{L} = \boldsymbol{r} \wedge m_{\mathrm{e}} \boldsymbol{v}_{\mathrm{e}} \tag{1.14}$$

induced by the notional current loop described by the electron (mass m_e, charge q_e) as it orbits the nucleus at radius $r = |\boldsymbol{r}|$ and speed $v_\mathrm{e} = |\boldsymbol{v}_\mathrm{e}|$. The magnetic moment of the loop is

$$\bar{\boldsymbol{\mu}} = i\mathrm{d}\boldsymbol{s} \tag{1.15}$$

where $\mathrm{d}\boldsymbol{s}$ is the elemental area of size πr^2 enclosed by the current $i = q_\mathrm{e} v_\mathrm{e}/2\pi r$. The direction of $\mathrm{d}\boldsymbol{s}$ is determined by the direction of conventional current (i.e. the opposite direction to the associated electron motion) so that Eqn. (1.15) can be written

$$\bar{\boldsymbol{\mu}} = \frac{1}{2} q_\mathrm{e} \boldsymbol{r} \wedge \boldsymbol{v}_\mathrm{e}. \tag{1.16}$$

Combining the result of Eqn. (1.16) with Eqn. (1.14), the orbital gyromagnetic ratio is then

$$\gamma_L = \frac{\bar{\boldsymbol{\mu}}}{\boldsymbol{L}} = \frac{q_\mathrm{e}}{2m_\mathrm{e}} = -14\,\mathrm{GHz\,T^{-1}}. \tag{1.17}$$

The spin angular momentum $\boldsymbol{S}$ eludes description in classical terms, but its gyromagnetic ratio can be shown to be approximately twice the orbital value

$$\gamma_S = 2\gamma_L = \frac{q_\mathrm{e}}{m_\mathrm{e}} = -28\,\mathrm{GHz\,T^{-1}}. \tag{1.18}$$

Returning to Eqn. (1.13), magnetic systems flavoured by both orbital and spin angular momentum are conventionally described in terms of an ‘effective’ gyromagnetic ratio

$$\gamma = g\frac{q_\mathrm{e}}{2m_\mathrm{e}} \tag{1.19}$$

where g is the Landé g-factor, equal to 1 for pure orbital angular momentum, 2 for pure spin. For electrons g is almost always positive and therefore γ is generally negative.

1.3.2 From single-spin to magnetization dynamics

Substituting for $\boldsymbol{J}$ in terms of $\bar{\boldsymbol{\mu}}$ from Eqn. (1.13), the equation of motion for a single quasi-classical spin obtained in §1.3.1.2 (Eqn. (1.12)) can be written

$$\frac{1}{\gamma}\frac{\mathrm{d}\bar{\boldsymbol{\mu}}}{\mathrm{d}t} = \bar{\boldsymbol{\mu}} \wedge \boldsymbol{B}.$$

From this relationship, and the fact that the magnetization produced by an ensemble of identical magnetic moments is equal to the product of their number density and their individual moments

$$\boldsymbol{M} = \overline{N}\bar{\boldsymbol{\mu}},$$

we can write a general expression for the magnetization dynamics of a meso- or macroscopic magnetic system, the Landau–Lifshitz equation:

$$\frac{\mathrm{d}\boldsymbol{M}}{\mathrm{d}t} = \gamma\boldsymbol{M} \wedge \boldsymbol{B}. \tag{1.20}$$

Equation (1.20) implies that once perturbed, the magnetization precesses indefinitely about the field $\boldsymbol{B}$. In real systems, coupling between the spin lattice and the mechanical structure of the material (mediated principally by phonon vibrations and the spin-orbit interaction) causes a loss of energy from the spin system which drives it back towards a relaxed state with $\boldsymbol{M}$ parallel to $\boldsymbol{B}$. Damping can be introduced into the model by adding a term which acts to minimize the precessional angle θ (see Fig. 1.6). Such a phenomenological damping term may be defined in a number of ways but perhaps the most widespread approach (originally proposed by Landau and Lifshitz) is to use the triple product $\boldsymbol{M} \wedge (\boldsymbol{M} \wedge \boldsymbol{B})$ to give a damped equation of the form

$$\frac{\mathrm{d}\boldsymbol{M}}{\mathrm{d}t} = \gamma\boldsymbol{M} \wedge \boldsymbol{B} - \alpha\frac{|\gamma|}{M_{\mathrm{S}}}\boldsymbol{M} \wedge (\boldsymbol{M} \wedge \boldsymbol{B}) \tag{1.21}$$

where α is a material dependent damping constant.

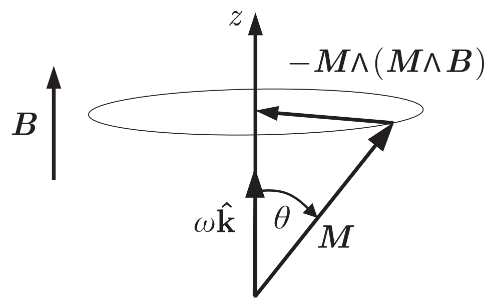

Figure 1.6: All real magnetic systems have intrinsic magnetic damping. This damping comes from a variety of sources but the main contribution in the systems relevant to experimental spin-wave studies is coupling between the magnon and phonon structures of the material brought about by vibrational modulation of the dipolar field of the spin lattice and/or the spin-orbit interaction. Damping causes the spin system to relax to an equilibrium state with the magnetization parallel to the applied field and can be modelled by introducing a phenomenological damping parameter proportional to $-\boldsymbol{M}\wedge(\boldsymbol{M}\wedge\boldsymbol{B})$.

1.3.3 Small-signal characteristics of magnetically saturated media

Building on the analysis of §1.3.2, in this section we determine the physical parameters which characterize the small-signal response of a magnetically saturated ferri- or ferromagnetic medium under conditions relevant to magnetostatic spin-wave propagation. For simplicity we neglect damping and assume zero shape and magnetocrystalline anisotropies.[12]

We divide the magnetic flux, magnetic field, and magnetization inside the material into static and small-signal components:

$$\boldsymbol{B}=\boldsymbol{B}_0+\boldsymbol{b}(t),\qquad \boldsymbol{H}=\boldsymbol{H}_0+\boldsymbol{h}(t),\qquad \boldsymbol{M}=\boldsymbol{M}_0+\boldsymbol{m}(t),$$

with $\boldsymbol{b}=b_x\hat{\mathbf{i}}+b_y\hat{\mathbf{j}}+b_z\hat{\mathbf{k}}$, $\boldsymbol{h}=h_x\hat{\mathbf{i}}+h_y\hat{\mathbf{j}}+h_z\hat{\mathbf{k}}$, $\boldsymbol{m}=m_x\hat{\mathbf{i}}+m_y\hat{\mathbf{j}}+m_z\hat{\mathbf{k}}$, and assume a system biased to or beyond saturation parallel to $\hat{\mathbf{k}}$, i.e. $\boldsymbol{B}_0=B_0\hat{\mathbf{k}}$ with $B_0\geq B_{\mathrm{S}}$, $\boldsymbol{H}_0=H_0\hat{\mathbf{k}}$ with $H_0\geq H_{\mathrm{S}}$, $\boldsymbol{M}_0=M_{\mathrm{S}}\hat{\mathbf{k}}$, and $m_z=0$. Under these conditions, ignoring

[12]It is important to note however that the analysis we present is equally valid for systems having finite magnetic anisotropy; anisotropy may be straightforwardly 'added' through the anisotropy field approach described in §1.1.1.

products of small terms, Eqn. (1.20) becomes

$$\frac{\mathrm{d}\boldsymbol{M}}{\mathrm{d}t} = \gamma \boldsymbol{M} \wedge \boldsymbol{B} = \gamma \left(\boldsymbol{M}_0 \wedge \boldsymbol{B}_0 + \boldsymbol{M}_0 \wedge \boldsymbol{b} + \boldsymbol{m} \wedge \boldsymbol{B}_0 \right). \tag{1.22}$$

The static field and magnetization components are parallel so that the first term in the brackets on the right-hand side of the expression above is zero and the equation can be reduced to

$$\frac{\mathrm{d}\boldsymbol{m}}{\mathrm{d}t} = \gamma \hat{\mathbf{k}} \wedge \left(M_\mathrm{S} \boldsymbol{b} - B_0 \boldsymbol{m} \right). \tag{1.23}$$

For the case that $\boldsymbol{m}(t), \boldsymbol{b}(t) \propto \mathrm{e}^{-\mathrm{i}\omega t}$, Eqn. (1.23) becomes

$$-\mathrm{i}\omega \boldsymbol{m} + \gamma B_0 \hat{\mathbf{k}} \wedge \boldsymbol{m} = \gamma M_\mathrm{S} \hat{\mathbf{k}} \wedge \boldsymbol{b} \tag{1.24}$$

which can be written

$$\frac{1}{\mu_0} \begin{pmatrix} b_x \\ b_y \end{pmatrix} = \frac{1}{\mu_0 \gamma M_\mathrm{S}} \begin{pmatrix} \gamma B_0 & +\mathrm{i}\omega \\ -\mathrm{i}\omega & \gamma B_0 \end{pmatrix} \begin{pmatrix} m_x \\ m_y \end{pmatrix}. \tag{1.25}$$

Substituting for $\boldsymbol{b}$ in terms of $\boldsymbol{h}$ and $\boldsymbol{m}$ $(\boldsymbol{b} = \mu_0 (\boldsymbol{h} + \boldsymbol{m})$, Eqn. (1.2)) into (1.25) we arrive at

$$\begin{pmatrix} h_x \\ h_y \end{pmatrix} = \frac{1}{\omega_\mathrm{M}} \begin{pmatrix} \omega_\mathrm{H} & +\mathrm{i}\omega \\ -\mathrm{i}\omega & \omega_\mathrm{H} \end{pmatrix} \begin{pmatrix} m_x \\ m_y \end{pmatrix} \tag{1.26}$$

where

$$\omega_\mathrm{H} = -\gamma \mu_0 H_0, \tag{1.27a}$$

$$\omega_\mathrm{M} = -\gamma \mu_0 M_\mathrm{S}. \tag{1.27b}$$

We note that since γ is almost always negative in the systems of interest to us (see §1.3.1.3), ω_M and ω_H are both positive. By inverting Eqn. (1.26) we derive a relation of the form

$$\boldsymbol{m} = \tilde{\boldsymbol{\chi}}_{\mathrm{m}} \boldsymbol{h} \tag{1.28}$$

where $\tilde{\boldsymbol{\chi}}_{\mathrm{m}}$ is the small-signal (Polder) susceptibility tensor [17]

$$\tilde{\boldsymbol{\chi}}_{\mathrm{m}} = \begin{pmatrix} \chi_{\mathrm{m}}^{'} & -\mathrm{i}\chi_{\mathrm{m}}^{''} & 0 \\ +\mathrm{i}\chi_{\mathrm{m}}^{''} & \chi_{\mathrm{m}}^{'} & 0 \\ 0 & 0 & 0 \end{pmatrix} \tag{1.29}$$

the components of which are the differential susceptibilities $\mathrm{d}m_i/\mathrm{d}h_j$:

$$\chi_{\mathrm{m}}^{'} = \frac{\omega_{\mathrm{H}}\omega_{\mathrm{M}}}{\omega_{\mathrm{H}}^2 - \omega^2}, \tag{1.30a}$$

$$\chi_{\mathrm{m}}^{''} = \frac{\omega\omega_{\mathrm{M}}}{\omega_{\mathrm{H}}^2 - \omega^2}. \tag{1.30b}$$

Note that the singularities in $\chi_{\mathrm{m}}^{'}$ and $\chi_{\mathrm{m}}^{''}$ at $\omega = \omega_{\mathrm{H}}$ only exist in the (non-physical) case of a magnetic system with zero damping. The resonance at $\omega = \omega_{\mathrm{H}}$ is genuine, but in real magnetic systems it will always be of finite height and width.

Combining Eqn. (1.29) with Eqn. (1.4), we can define a small-signal permeability tensor $\tilde{\boldsymbol{\mu}}$

$$\tilde{\boldsymbol{\mu}} = \mu_0 \left(\mathbf{I} + \tilde{\boldsymbol{\chi}}_{\mathrm{m}}\right) = \mu_0 \begin{pmatrix} 1 + \chi_{\mathrm{m}}^{'} & -\mathrm{i}\chi_{\mathrm{m}}^{''} & 0 \\ +\mathrm{i}\chi_{\mathrm{m}}^{''} & 1 + \chi_{\mathrm{m}}^{'} & 0 \\ 0 & 0 & 1 \end{pmatrix} \tag{1.31}$$

and hence relate $\boldsymbol{b}$ to $\boldsymbol{m}$ through a small-signal version of Eqn. (1.3)

$$\boldsymbol{b} = \tilde{\boldsymbol{\mu}} \boldsymbol{h}. \tag{1.32}$$

1.4 Maxwell's equations in the magnetostatic limit

In this section, we turn to the Maxwell equations to understand the dynamic properties of spatially and temporally varying magnetic excitations in an environment characterized by the small-signal parameters derived in §1.3.3. We arrive at a description of a magnetostatic spin wave as a solution to these equations in the so-called 'magnetostatic limit'.

In their most general form, Maxwell's four relations are:

$$\nabla \wedge \boldsymbol{H} = \boldsymbol{J}_{\mathrm{c}} + \frac{\partial \boldsymbol{D}}{\partial t}, \tag{1.33}$$

$$\nabla \wedge \boldsymbol{E} = -\frac{\partial \boldsymbol{B}}{\partial t}, \tag{1.34}$$

$$\nabla \cdot \boldsymbol{D} = \rho, \tag{1.35}$$

$$\nabla \cdot \boldsymbol{B} = 0, \tag{1.36}$$

where the magnetic quantities are as already defined and $\boldsymbol{J}_{\mathrm{c}}$ is current density, ρ is charge density, $\boldsymbol{D}$ is electric displacement and $\boldsymbol{E}$ is electric field. In a linear medium $\boldsymbol{D}$ and $\boldsymbol{E}$ are related by

$$\boldsymbol{D} = \epsilon_0 \left(\mathbf{I} + \boldsymbol{\chi}_{\mathrm{e}}\right) \boldsymbol{E} \tag{1.37}$$

where $\epsilon_0 \equiv (1/\mu_0 c^2) \simeq 8.854 \times 10^{-12}\,\mathrm{F\,m^{-1}}$ is permittivity of free space, and $\boldsymbol{\chi}_{\mathrm{e}}$ the electrical susceptibility tensor. The equation above can also be written in terms of a permittivity tensor $\boldsymbol{\epsilon}$:

$$\boldsymbol{D} = \boldsymbol{\epsilon}\boldsymbol{E}. \tag{1.38}$$

In line with the analysis of §1.3.3 we shall assume that all fields may be separated into static ($\boldsymbol{B}_0$, $\boldsymbol{H}_0$, $\boldsymbol{D}_0$, $\boldsymbol{E}_0$) and small-signal components ($\boldsymbol{b}(t)$, $\boldsymbol{h}(t)$, $\boldsymbol{d}(t)$, $\boldsymbol{e}(t)$) and focus our attention on the latter.

We simplify our analysis by restricting the electrical properties of the wave medium to the subset which are of particular relevance to the experimental investigations of later chapters; electrically isotropic, source free insulating media. We define a scalar permittivity

$$\boldsymbol{\epsilon} = \epsilon \mathbf{I} \tag{1.39}$$

and assume that this holds both for small and large signals. Under these conditions Eqns. (1.33) to (1.36) become

$$\nabla \wedge \boldsymbol{h} = \epsilon \frac{\partial \boldsymbol{e}}{\partial t}, \tag{1.40}$$

$$\nabla \wedge \boldsymbol{e} = -\mu_0 \frac{\partial}{\partial t} \left(\boldsymbol{h} + \boldsymbol{m} \right), \tag{1.41}$$

$$\nabla \cdot \epsilon \boldsymbol{e} = 0, \tag{1.42}$$

$$\nabla \cdot \mu_0 \left(\boldsymbol{h} + \boldsymbol{m} \right) = 0. \tag{1.43}$$

where we have used Eqn. (1.2) to substitute[13] for $\boldsymbol{b}$ in terms of $\boldsymbol{h}$ and $\boldsymbol{m}$. For plane wave solutions of the form $\mathrm{e}^{\mathrm{i}\boldsymbol{k}\cdot\boldsymbol{r}-\mathrm{i}\omega t}$, the differential operator $\nabla = \mathrm{i}\boldsymbol{k}$ so that Eqns. (1.40) to (1.43) reduce to

$$\boldsymbol{k} \wedge \boldsymbol{h} = -\omega \epsilon \boldsymbol{e}, \tag{1.44}$$

$$\boldsymbol{k} \wedge \boldsymbol{e} = \omega \mu_0 \left(\boldsymbol{h} + \boldsymbol{m} \right), \tag{1.45}$$

$$\boldsymbol{k} \cdot \epsilon \boldsymbol{e} = 0, \tag{1.46}$$

$$\boldsymbol{k} \cdot \mu_0 \left(\boldsymbol{h} + \boldsymbol{m} \right) = 0. \tag{1.47}$$

Equations. (1.44) and (1.45) can be combined to yield

$$\boldsymbol{k} \wedge \left(\boldsymbol{k} \wedge \boldsymbol{h} \right) = -\omega^2 \mu_0 \epsilon \left(\boldsymbol{h} + \boldsymbol{m} \right). \tag{1.48}$$

Following the treatment of Stancil [16], the vector cross products can be removed by

[13] See prefatory note, pages 1–2.

defining a skew-symmetric matrix $\mathbf{K}$

$$\mathbf{K} = \begin{pmatrix} 0 & -k_z & k_y \\ k_z & 0 & -k_x \\ -k_y & k_x & 0 \end{pmatrix} \tag{1.49}$$

such that for a general vector $\boldsymbol{a}$, $\mathbf{K}\boldsymbol{a} = \boldsymbol{k} \wedge \boldsymbol{a}$, and $\mathbf{KK} = \boldsymbol{k}\boldsymbol{k}^{\mathrm{T}} - k^2\mathbf{I}$, so that

$$\left(\boldsymbol{k}\boldsymbol{k}^{\mathrm{T}} - k^2\mathbf{I}\right)\boldsymbol{h} = -\omega^2\mu_0\epsilon\left(\boldsymbol{h} + \boldsymbol{m}\right) = -\omega^2\epsilon\tilde{\boldsymbol{\mu}}\boldsymbol{h}. \tag{1.50}$$

We now consider two possible solutions to Eqn. (1.50).

• **Solution 1:** $\boldsymbol{m} = 0$

If the small-signal magnetization $\boldsymbol{m} = 0$ (i.e. $\tilde{\boldsymbol{\chi}}_{\mathrm{m}} = 0$), Eqn. (1.47) implies $\boldsymbol{k} \cdot \boldsymbol{h} = 0$ and thus Eqn. (1.50) leads to

$$k = k_0 = \omega\sqrt{\mu_0\epsilon}, \tag{1.51}$$

which is the familiar dispersion relation for plane electromagnetic waves in an isotropic, source free, electrically insulating medium.

• **Solution 2:** $\boldsymbol{m} \neq 0$

This second family of solutions is the one which is of interest to us in the context of spin-wave dynamics. When the small-signal magnetization is non-zero Eqn. (1.50) can be written

$$\left(\boldsymbol{k}\boldsymbol{k}^{\mathrm{T}} - k^2\mathbf{I} + \omega^2\epsilon\tilde{\boldsymbol{\mu}}\right)\boldsymbol{h} = 0. \tag{1.52}$$

The equation above is of the form $\mathbf{A}\boldsymbol{h} = 0$, non-trivial solutions therefore satisfy $\det\mathbf{A} = 0$, which in the case that a saturating (or super-saturating) magnetic field is present parallel to $\hat{\mathbf{k}}$ is (from Eqn. (1.31))

$$\begin{pmatrix} k_0^2\left(1+\chi_{\mathrm{m}}^{'}\right)-k_y^2-k_z^2 & k_xk_y-\mathrm{i}k_0^2\chi_{\mathrm{m}}^{''} & k_xk_z \\ k_yk_x+\mathrm{i}k_0^2\chi_{\mathrm{m}}^{''} & k_0^2\left(1+\chi_{\mathrm{m}}^{'}\right)-k_x^2-k_z^2 & k_yk_z \\ k_zk_x & k_zk_y & k_0^2-k_x^2-k_y^2 \end{pmatrix} = 0. \tag{1.53}$$

We shall explore this solution by first investigating a particular case: one in which the wave propagates parallel to the bias field i.e. $\boldsymbol{k} = k_z\hat{\mathbf{k}}$. Under these conditions, Eqn. (1.53) simplifies significantly:

$$\begin{pmatrix} k_0^2\left(1+\chi_{\mathrm{m}}^{'}\right)-k_z^2 & -\mathrm{i}k_0^2\chi_{\mathrm{m}}^{''} & 0 \\ +\mathrm{i}k_0^2\chi_{\mathrm{m}}^{''} & k_0^2\left(1+\chi_{\mathrm{m}}^{'}\right)-k_z^2 & 0 \\ 0 & 0 & k_0^2 \end{pmatrix} = 0. \tag{1.54}$$

Solving the determinant equation above leads to a quartic expression for k_z, the roots of which are

$$k_{z+}^2 = k_0^2\left(1+\chi_{\mathrm{m}}^{'}+\chi_{\mathrm{m}}^{''}\right), \tag{1.55a}$$

$$k_{z-}^2 = k_0^2\left(1+\chi_{\mathrm{m}}^{'}-\chi_{\mathrm{m}}^{''}\right). \tag{1.55b}$$

Equations (1.55) can be written explicitly in terms of ω_{H} and ω_{M} (substituting from Eqns. (1.30)):

$$k_{z+}^2 = k_0^2\left(1+\frac{\omega_{\mathrm{M}}}{\omega_{\mathrm{H}}-\omega}\right), \tag{1.56a}$$

$$k_{z-}^2 = k_0^2\left(1+\frac{\omega_{\mathrm{M}}}{\omega_{\mathrm{H}}+\omega}\right). \tag{1.56b}$$

Functions k_{z+} and k_{z-} are plotted in Fig. 1.7, in blue and red respectively, for the case $\omega_{\mathrm{H}}/\omega_{\mathrm{M}} = 1$, $\omega^* = \omega/\omega_{\mathrm{M}}$, and $k_z^* = k_z\omega^*/k_0$. The black dashed line plotted on the same axes is the dispersion relation for plane electromagnetic waves (Eqn. (1.51)).

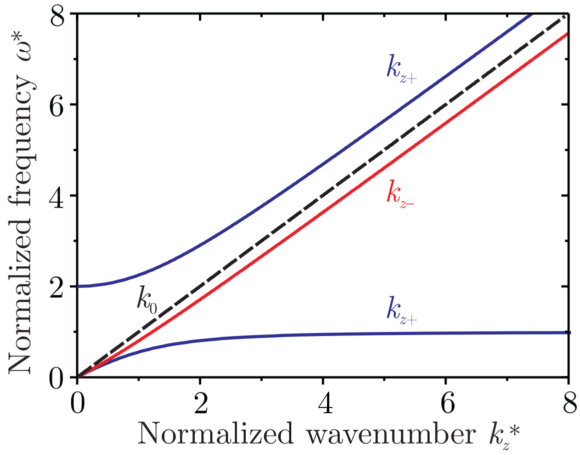

Figure 1.7: Dispersion relations of Eqns. (1.56a) (blue) and (1.56b) (red) for $\omega_\mathrm{H}/\omega_\mathrm{M} = 1$ normalized to $\omega^* = \omega/\omega_\mathrm{M}$ and $k_z^* = k_z\omega^*/k_0$. The black dashed line is the electromagnetic solution (Eqn. (1.51)).

The functions have several interesting features. Firstly, we note that the k_{z+} solution interacts more strongly with the medium than the k_{z-} solution, which is not substantially different from the k_0 case. This difference arises because the electric and magnetic fields associated with the two differ in polarization. Those corresponding to k_{z+} are both right circularly polarized, to k_{z-}, left circularly polarized. The fields associated with a right circularly polarized wave propagating in the direction of positive $\hat{\mathbf{k}}$ rotate with the same sense as the natural precession of the magnetization (as defined by Eqn. (1.20)) and thus the k_{z+} solution has substantially greater leverage on the magnetic system than its counter-rotating k_{z-} counterpart. The interaction between the k_{z+} solution and the medium is maximum when its frequency matches the natural precessional frequency $\omega = \omega_\mathrm{H}$ (cf. Eqns. (1.30)). This value of ω corresponds to the limit $k_{z+} \to \infty$. Between $\omega = \omega_\mathrm{H}$ and $\omega = \omega_\mathrm{H} + \omega_\mathrm{M}$ the k_{z+} solution is imaginary and therefore waves cannot propagate. Finally, looking again at the low-frequency branch of the k_{z+} dispersion relation we see that beyond $k_z^* \sim 0.5$, $k_{z+} \gg k_0$ i.e. the wavelength of the waves is substantially shorter than the electromagnetic wavelength at the same frequency. This characteristic is the hallmark of a magnetostatic wave.

Returning to Eqn. (1.50) we can derive a general expression for the small-signal magnetic and electric fields corresponding to the $\boldsymbol{m} \neq 0$ solutions:
Equation (1.47) implies $\boldsymbol{k} \cdot \boldsymbol{h} = -\boldsymbol{k} \cdot \boldsymbol{m}$. Using this relationship and Eqns. (1.44), (1.45), (1.46), and (1.51), we arrive at

$$\boldsymbol{h} = \frac{\left(k_0^2 \mathbf{I} - \boldsymbol{k}\boldsymbol{k}^{\mathrm{T}}\right) \boldsymbol{m}}{k^2 - k_0^2}, \tag{1.57}$$

$$\boldsymbol{e} = -\frac{\omega \mu_0}{k^2 - k_0^2} \left(\boldsymbol{k} \wedge \boldsymbol{m}\right), \tag{1.58}$$

and can also write an expression for $\nabla \wedge \boldsymbol{h}$:

$$\nabla \wedge \boldsymbol{h} = \frac{\mathrm{i} k_0^2}{k^2 - k_0^2} \left(\boldsymbol{k} \wedge \boldsymbol{m}\right). \tag{1.59}$$

Examining these equations in the limit of large k, we see that both $\boldsymbol{e}$ and $\nabla \wedge \boldsymbol{h}$ tend to zero, whilst so long as $\boldsymbol{k} \cdot \boldsymbol{m} \neq 0$, $\boldsymbol{h}$ remains finite.[14] The $k \gg k_0$ limit of Eqns. (1.57) to (1.59) is often summarized by a three-formula description of plane magnetostatic spin waves in source free insulating magnetic media:

$$\nabla \wedge \boldsymbol{e} = \mathrm{i}\omega \tilde{\boldsymbol{\mu}} \boldsymbol{h}, \tag{1.60}$$

$$\nabla \cdot \tilde{\boldsymbol{\mu}} \boldsymbol{h} = 0, \tag{1.61}$$

$$\nabla \wedge \boldsymbol{h} = 0. \tag{1.62}$$

The first two of the expressions above are simply statements of the Maxwell relations Eqns. (1.41) and (1.43) applied to small-signal plane waves;[15] the third plays the role of a governing equation.

[14] Note that $\boldsymbol{k} \cdot \boldsymbol{m} = 0$ corresponds to the resonance condition in which $\boldsymbol{m}$ is finite, whilst $\boldsymbol{h}$ and $\boldsymbol{e}$ are zero.

[15] Note however that the definition of $\tilde{\boldsymbol{\mu}}$ (Eqn. (1.31)) includes information about the magnetic state of the host material.

1.5 Spin-wave propagation in magnetic thin films

In this section we expand on the results of §1.4 to develop an understanding of the dynamic properties of magnetostatic spin waves in the particular subset of magnetic systems which are at the focus of the experimental investigations of subsequent chapters: thin films.

1.5.1 Spin-wave mode shapes

Within the framework of the magnetostatic approximation summarized by Eqns. (1.60) to (1.62), the magnetostatic modes associated with a given magnetic geometry (i.e. shape of magnetic sample) can be obtained by describing the small-signal magnetic field $\boldsymbol{h}$ in terms of a magnetostatic scalar potential ψ:

$$\boldsymbol{h} = \nabla\psi. \tag{1.63}$$

Since $\nabla \cdot \tilde{\boldsymbol{\mu}}\boldsymbol{h} = 0$ (Eqn. (1.61)), Eqn. (1.63) implies

$$\nabla \cdot (\tilde{\boldsymbol{\mu}} \cdot \nabla\psi) = 0. \tag{1.64}$$

Combining the above result with Eqn. (1.31) leads to a general governing equation for modes propagating in a system biased by a magnetic field parallel to $\hat{\boldsymbol{k}}$:

$$\left(1 + \chi_{\mathrm{m}}^{'}\right)\left(\frac{\partial^2\psi}{\partial x^2} + \frac{\partial^2\psi}{\partial y^2}\right) + \frac{\partial^2\psi}{\partial z^2} = 0. \tag{1.65}$$

The expression above is known as Walker's equation [16].

1.5.2 Exchange-dominated spin waves (a brief aside)

As stated from the outset, in the context of the experiments which follow, our interest is in spin waves with dynamics governed by the dipolar interaction. However, before progressing further, is it appropriate to pause briefly say a few words about the exchange-dominated region of the spin-wave spectrum.

The effect of the exchange interaction on the dynamics of the spin lattice can be modelled by postulating an effective 'exchange field' $\boldsymbol{H}_{\mathrm{ex}}$:

$$\boldsymbol{H}_{\mathrm{ex}} = \lambda_{\mathrm{ex}} \nabla^2 \boldsymbol{M} \tag{1.66}$$

which is superposed on top of $\boldsymbol{H}_0$ and $\boldsymbol{h}$.[16] λ_{ex} is a (material dependent) exchange constant.

Using the exchange field formalism and Eqn. (1.65), a general expression can be obtained for the dispersion of spin waves under the influence of exchange in an infinite medium [16]:

$$\omega = \sqrt{\left(\omega_{\mathrm{H}} + \omega_{\mathrm{M}} \lambda_{\mathrm{ex}} k^2\right) \left(\omega_{\mathrm{H}} + \omega_{\mathrm{M}} \left(\lambda_{\mathrm{ex}} k^2 + \sin^2 \vartheta\right)\right)} \tag{1.67}$$

where ϑ is the propagation angle with respect to the bias field. In the limit of large k it can be seen that $\omega \propto \lambda_{\mathrm{ex}} k^2$. These exchange-dominated waves typically have wavelengths in the nanometre range and group velocities which are substantially higher than those of magnetostatic excitations.

[16] Note that the field $\lambda_{\mathrm{ex}} \nabla^2 \boldsymbol{M}$ is not the total exchange field, but the torque producing component of it. The total exchange field contains an additional term proportional and parallel to $\boldsymbol{M}$.

1.5.3 Magnetostatic spin-wave propagation in magnetic thin films

The focus of the experimental work of subsequent chapters is the propagation of plane magnetostatic spin waves in electrically insulating thin-film magnetic waveguides. The dynamics of spin waves propagating in such systems are sensitive both to the relative orientation of the magnetic bias field and the spin-wave wavevector and to the direction of the magnetic bias field relative to the thickness of the film.

The magnetostatic spin waves which propagate in thin films are divided into three dynamically distinct classes corresponding to the three mutually orthogonal possible orientations of the magnetic bias field and $\boldsymbol{k}$:

- **Magnetostatic surface spin waves** (MSSW) (also known as Damon Eschbach modes) propagate in the plane of a film, perpendicular to an in-plane bias field. These waves are associated with a small-signal magnetization which is exponentially distributed across the film thickness with a maximum at one surface [16, 18–20] (Fig. 1.8).
- **Forward volume magnetostatic spin waves** (FVMSW) propagate in the plane of a film under conditions of out-of-plane magnetic bias (Fig. 1.9).
- **Backward volume magnetostatic spin waves** (BVMSW) propagate in the plane of a film, parallel to an in-plane bias field (Fig. 1.10).

Forward and backward volume spin waves are the summation of guided plane waves reflecting from the inner surfaces of the film and their full spectrum contains an infinite array of dispersive branches, each corresponding to a different thickness mode. However, thickness modes other than the lowest order are not efficiently excited using conventional experimental techniques[17] and so for the majority of practical

[17] Though they may be indirectly excited by energetic coupling to waves in the in-plane region of the spectrum.

experimental purposes, can be neglected.

Full analytic derivation of the dispersion relations for MSSW, FVMSW and BVMSW requires lengthy mathematics which will not be presented here, instead we shall briefly survey its results and comment on their physical interpretation.

1.5.3.1 Magnetostatic surface spin waves (MSSW)

The dispersion relation for surface spin waves is given by

$$\omega = \sqrt{\omega_{\mathrm{H}} \left(\omega_{\mathrm{H}} + \omega_{\mathrm{M}}\right) + \frac{\omega_{\mathrm{M}}^2}{4} \left(1 - \mathrm{e}^{-2kd}\right)} \tag{1.68}$$

where k is the in-plane wavenumber perpendicular to the direction of the magnetic bias field and (as previously defined in Eqns. (1.27)),

$$\omega_{\mathrm{H}} = -\gamma\mu_0 H_0,$$
$$\omega_{\mathrm{M}} = -\gamma\mu_0 M_{\mathrm{S}}.$$

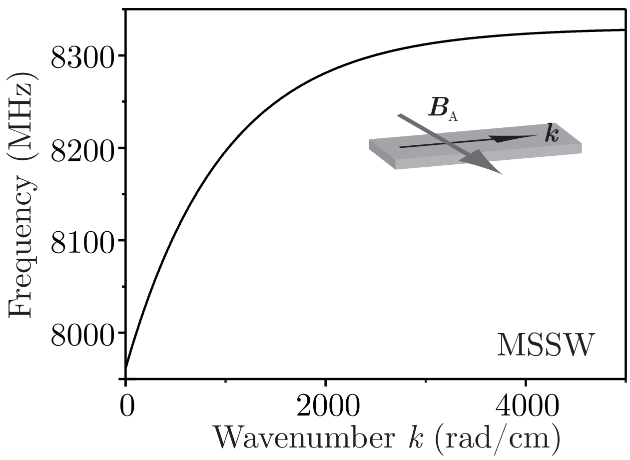

Figure 1.8: Magnetostatic surface spin waves (MSSW) (also known as Damon Eschbach modes) propagate perpendicular to an in-plane bias field in a manifold between $\omega = \sqrt{\omega_{\mathrm{H}} \left(\omega_{\mathrm{H}} + \omega_{\mathrm{M}}\right)}$ and $\omega = \omega_{\mathrm{H}} + \omega_{\mathrm{M}}/2$. Their magnetization is exponentially distributed across the film thickness with a maximum at one surface. The dispersion curve plotted above corresponds to a film of thickness 5 µm and saturation magnetization $M_{\mathrm{S}} = 140\,\mathrm{kA\,m^{-1}}$ subject to an applied magnetic bias field $B_{\mathrm{A}} = 210\,\mathrm{mT}$ ($H_0 = 210\,\mathrm{mT}/\mu_0$).

Since the in-plane dimensions of a thin film are very large in comparison with its thickness, the external magnetic field produced by magnetizing it in plane is negligible. As a result, an in-plane *applied* magnetic flux density B_A gives rise to an internal magnetic flux density $B_0 = B_\mathrm{A}$. It follows that the value of H_0 which appears in ω_H is

$$H_0 = B_\mathrm{A}/\mu_0. \tag{1.69}$$

A distinguishing feature of MSSW is a characteristic known as field displacement non-reciprocity; the magnetostatic potential fields associated with the waves are dependent on the direction of $\boldsymbol{k}$. When the direction of propagation is reversed, the mode energy shifts from one surface of the film to another. The waves exist in a manifold between a low-frequency $k = 0$ (FMR) limit at $\omega = \sqrt{\omega_\mathrm{H}\left(\omega_\mathrm{H} + \omega_\mathrm{M}\right)}$ and a high-frequency asymptote $\omega = \omega_\mathrm{H} + \omega_\mathrm{M}/2$.

In the limit of small kd (the conditions relevant to almost all practical experiments) the group velocity of MSSW is approximately

$$v_\mathrm{g} = \frac{\partial\omega}{\partial k} = \frac{\omega_\mathrm{M}}{\sqrt{\omega_\mathrm{H}\left(\omega_\mathrm{H} + \omega_\mathrm{M}\right)}}\frac{\omega_\mathrm{M} d}{4}, \tag{1.70}$$

whilst the phase velocity is given by

$$v_\mathrm{p} = \frac{\omega}{k} = \frac{1}{k}\left(\sqrt{\omega_\mathrm{H}\left(\omega_\mathrm{H} + \omega_\mathrm{M}\right)}\right) + v_\mathrm{g}. \tag{1.71}$$

Equation (1.68) is plotted in Fig. 1.8 for a magnetic film of thickness $5\,\mu\mathrm{m}$ and saturation magnetization $M_\mathrm{S} = 140\,\mathrm{kA\,m^{-1}}$ subject to an applied magnetic bias field $B_\mathrm{A} = 210\,\mathrm{mT}$.

1.5.3.2 Forward volume spin waves (FVMSW)

As we would anticipate from symmetry, the dispersion characteristics of spin waves propagating under conditions of out-of-plane magnetic bias are directionally invariant in the plane of the film. It has been shown by Kalinikos [16, 21] that the dispersion relation for (first thickness mode) FVMSW spin waves of in-plane wavenumber $k = \left|k_x^2 + k_y^2\right|$ may be approximated by

$$\omega = \sqrt{\omega_{\mathrm{H}}\left(\omega_{\mathrm{H}} + \omega_{\mathrm{M}}\left(1 - \frac{1 - \mathrm{e}^{-kd}}{kd}\right)\right)}. \tag{1.72}$$

A thin film magnetized out of plane has an effective demagnetizing field $H_{\mathrm{demag}} = -M_{\mathrm{S}}$. As a result, the value of H_0 which defines ω_{H} is related to the applied magnetic bias field B_{A} by

$$H_0 = B_{\mathrm{A}}/\mu_0 - M_{\mathrm{S}}. \tag{1.73}$$

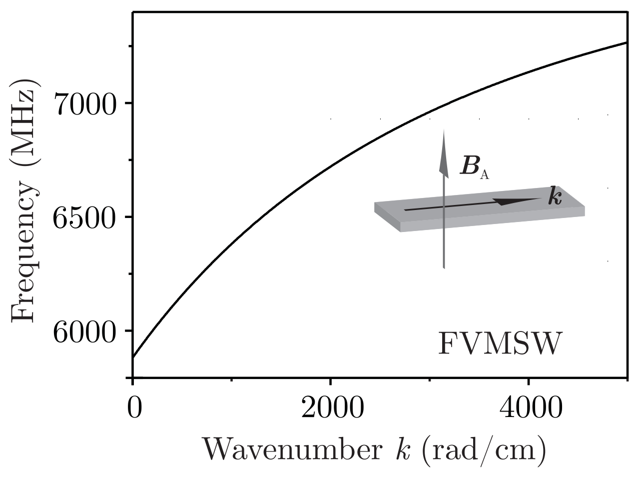

Figure 1.9: Forward volume spin waves (FVMSW) are supported by conditions of out-of-plane magnetic bias. Their low-frequency limit is $\omega = \omega_{\mathrm{H}}$, their upper frequency asymptote $\omega = \sqrt{\omega_{\mathrm{H}}\left(\omega_{\mathrm{H}} + \omega_{\mathrm{M}}\right)}$. FVMSW dispersion characteristics are invariant with direction in the plane of the film and their magnetization distribution is sinusoidal across its thickness. The dispersion curve plotted above corresponds to a film of thickness $5\,\mu\mathrm{m}$ and saturation magnetization $M_{\mathrm{S}} = 140\,\mathrm{kA\,m^{-1}}$ subject to an applied magnetic bias field $B_{\mathrm{A}} = 385\,\mathrm{mT}$ ($H_0 = 210\,\mathrm{mT}/\mu_0$).

Equation (1.72) is plotted in Fig. 1.9 for a film of thickness $5\,\mu\mathrm{m}$ and saturation magnetization $M_{\mathrm{S}} = 140\,\mathrm{kA\,m^{-1}}$ subject to an applied magnetic bias field $B_{\mathrm{A}} = 385\,\mathrm{mT}$ ($H_0 = 210\,\mathrm{mT}/\mu_0$, as for the data plotted in Fig. 1.8). In the limit of small kd the group velocity of the waves is approximately

$$v_{\mathrm{g}} = \frac{\omega_{\mathrm{M}} d}{4}, \tag{1.74}$$

whilst the phase velocity is given by

$$v_{\mathrm{p}} = \frac{\omega}{k} = \frac{\omega_{\mathrm{H}}}{k} + v_{\mathrm{g}}. \tag{1.75}$$

The upper frequency (high-k) limit of the FVMSW dispersion curve corresponds to $\omega = \sqrt{\omega_{\mathrm{H}}\left(\omega_{\mathrm{H}} + \omega_{\mathrm{M}}\right)}$, the low-frequency ($k = 0$, FMR) limit to $\omega = \omega_{\mathrm{H}}$.

1.5.3.3 Backward volume spin waves (BVMSW)

An approximate dispersion relation for (first thickness mode) BVMSW is also owed to Kalinikos [16, 21]

$$\omega = \sqrt{\omega_{\mathrm{H}}\left(\omega_{\mathrm{H}} + \omega_{\mathrm{M}}\left(\frac{1 - \mathrm{e}^{-kd}}{kd}\right)\right)}; \tag{1.76}$$

here k is the wavenumber parallel to the bias field direction and the relationship between the value of H_0 which defines ω_{H} and the magnetic bias field B_{A} applied to the film is the same as for MSSW (Eqn. (1.69)).

Equation (1.76) is plotted in Fig. 1.10 for a film of thickness $5\,\mu\mathrm{m}$ and saturation magnetization $M_{\mathrm{S}} = 140\,\mathrm{kA\,m^{-1}}$ subject to an applied magnetic bias field $B_{\mathrm{A}} = 210\,\mathrm{mT}$ ($H_0 = 210\,\mathrm{mT}/\mu_0$, as for the data plotted in Fig. 1.8 and Fig. 1.9). In the limit of small kd the group velocity of the waves is approximately

$$v_{\mathrm{g}} = -\frac{\omega_{\mathrm{H}}}{\sqrt{\omega_{\mathrm{H}}\left(\omega_{\mathrm{H}} + \omega_{\mathrm{M}}\right)}} \frac{\omega_{\mathrm{M}} d}{4}, \tag{1.77}$$

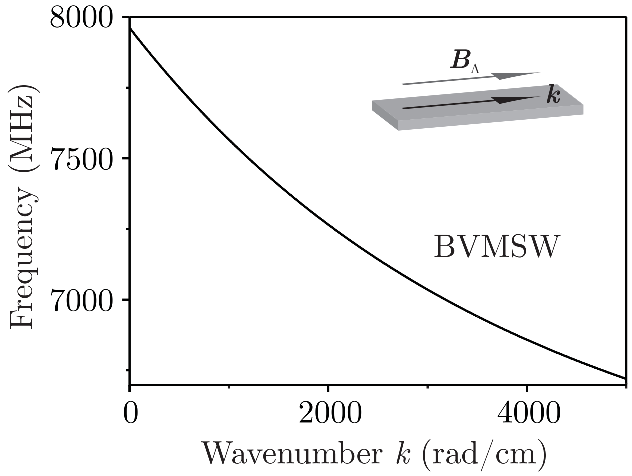

Figure 1.10: Backward volume spin waves (BVMSW) propagate parallel to an in-plane bias field. The gradient of their dispersion curve is negative so that short wavelengths are associated with low-frequency waves. The high-frequency limit of the dispersion curve corresponds to the (long-wavelength) $k = 0$ limit at $\omega = \sqrt{\omega_{\mathrm{H}}(\omega_{\mathrm{H}} + \omega_{\mathrm{M}})}$, the low-frequency asymptote is $\omega = \omega_{\mathrm{H}}$. Like forward volume waves (Fig. 1.9) BVMSW have a magnetization distribution which is sinusoidal across the film thickness. The dispersion curve plotted above corresponds to a film of thickness 5 µm and saturation magnetization $M_{\mathrm{S}} = 140\,\mathrm{kA\,m^{-1}}$ subject to an applied magnetic bias field $B_{\mathrm{A}} = 210\,\mathrm{mT}$ ($H_0 = 210\,\mathrm{mT}/\mu_0$).

whilst the phase velocity is given by

$$v_{\mathrm{p}} = \frac{1}{k}\sqrt{\omega_{\mathrm{H}}(\omega_{\mathrm{H}} + \omega_{\mathrm{M}})} + v_{\mathrm{g}}. \tag{1.78}$$

Comparing Eqn. (1.77) with Eqn. (1.78) we see that the former is always negative whilst, since kd is small and $\omega_{\mathrm{M}} \geq 0$, the latter is always positive. From this, we conclude that the group and phase velocities of the waves are in opposite directions and the higher the wavenumber of the waves (i.e. the shorter the wavelength), the *lower* the wave frequency. It is this unusual physics which earns these modes the label ‘backward’.

The high-frequency limit of the BVMSW dispersion curve corresponds to the long-wavelength $k = 0$ limit at $\omega = \sqrt{\omega_{\mathrm{H}}(\omega_{\mathrm{H}} + \omega_{\mathrm{M}})}$ (the FMR frequency), the low-frequency, high-k limit to $\omega = \omega_{\mathrm{H}}$.

Chapter 2

Experimental materials, methods, and motivations

2.1 Introduction

Building on the general description of magnetostatic spin-wave propagation presented in chapter 1, this chapter provides a detailed introduction to the experimental investigations described in chapters 3 and 4. We discuss the particular experimental materials and techniques employed and the scientific context of the work.

2.2 Materials and methods

2.2.1 An introduction to experimental spin-wave materials

Experimental spin-wave science began in ferromagnetic metals, notably cobalt, nickel, and iron films [22]. Today, though ferromagnetic resonance based analytical techniques are deployed in the magnetic characterization of a wide range of metallic structures and systems, in the experimental study of spin-wave phenomena (i.e. propagating, dispersive spin waves as opposed to FMR), by far the most important metallic material is Permalloy.

The term Permalloy (commonly abbreviated to Py) refers to the family of ferromagnetic nickel-rich face centred cubic nickel–iron alloys $Fe_xNi_{(1-x)}$, for $\sim 0.18 \leq x <\sim 0.25$. For reasons which are only partly understood, alloys having this range of stoichiometries combine very large magnetic permeability with exceptionally low magnetocrystalline anisotropy, coercivity[1] (typically $< 80\,\mathrm{kA\,m^{-1}}$ in-plane in thin films), and magnetostriction[2] (for a readable and enlightening introduction see Ref. [23]). As a result, Permalloy has long been among experimental magnetics' most important soft ferromagnetic materials. In the context of magnetic dynamics the material has made, and continues to make, a key contribution to our fundamental understanding of domain-wall dynamics [24–28] and has been instrumental in the development of magnetic memory concept technologies [29–31] and spin-torque oscillators [32, 33].

For the spin-wave dynamicist, thin-film polycrystalline Permalloy has three key attractions: it is easy to deposit using standard thermal evaporation or sputtering techniques, its chemistry is straightforward and uncontroversial and—most importantly of all—its intrinsic magnetic damping is significantly lower than that of other metals and alloys (for a useful comparison see Table 6 in Ref. [34]). This collection of attributes makes Permalloy the ideal development material for prototype spin-wave and spin-wave spintronic devices and an obvious choice for the observation of spin-wave phenomena at the micro- and nanoscales.

However, despite being low in relative terms, the spin-wave damping in Permalloy is still significant (typically spin-wave mean free paths are below $10\,\mu\mathrm{m}$) and recent years have seen an expansion in the research effort directed towards the search for lower-loss metallic and intermetallic alternatives. Iron has long been known to have potential in this context since although in polycrystalline form it is outperformed

[1] Coercivity is a measure of how 'difficult' it is to magnetize and demagnetize a material. The coercive field is the magnetic field required to reduce the magnetization from its saturation value to zero. Magnetic materials with large coercive fields are known as 'hard' magnets, those with low coercive fields, 'soft' magnets.

[2] Magnetostriction is mechanical strain (which may be positive or negative) associated with the application of a magnetic field.

by Permalloy, the damping in monocrystalline Fe is, in theory, around an order of magnitude lower. However, practical difficulties associated with growing high-quality defect-free monocrystalline films have yet to be overcome, and although Fe is far from being abandoned, the low-damping searchlight is increasingly being shone elsewhere. At present, particular attention is focused on the family of so-called Heusler compounds or 'Heusler alloys'. Heusler alloys are ferromagnetic intermetallic compounds of two types: full-Heusler compounds, which have the general formula A_2BC where A and B are transition metals and C is a main group element, and half-Heusler compounds which are of the form ABC.

Heusler compounds were discovered at the beginning of the twentieth century when the German chemist Friedrich Heusler made the observation that—despite containing no ferromagnetic elements—Cu_2MnAl was ferromagnetic [35]. A recent re-explosion of interest in Heusler systems is the result of a newer but equally remarkable insight into their properties: In 1983, de Groot et al. demonstrated that the half-Heusler compound NiMnSb could be expected to exhibit 100 % spin polarization at the Fermi level [36], a characteristic which has come to be known as half-metallicity. The potential significance of this exotic transport property for the field of spintronics was immediately recognized. Over the last twenty-five years, predictions of half-metallicity (or high spin polarization at the Fermi level) in a number of other Heusler compounds have been made (notably Co_2FeSi), and it has been shown that, in theory, some of these same compounds should also have significantly lower damping than Permalloy. Although the experimental synthesis, characterization, and optimization of these materials is in its infancy, spin polarizations in excess of 85 % have already been measured [34, 37, 38], as have very favourable damping parameters [34, 37–44].

If Heusler alloys are destined to play a starring role in the future of spin-wave science, they will do so in the footsteps of another celebrity material: the ferrimagnetic insulator yttrium iron garnet ($Y_3Fe_5O_{12}$, YIG). The spin-wave damping in monocrystalline YIG is the lowest of any known practical experimental material; two orders of magnitude smaller than that of Permalloy. The synthesis of YIG around the middle of the last century brought about a step change in the field of experimental spin-wave dynamics and the material remains unchallenged as the single most important model system for the study of fundamental spin-wave physics.

The experimental investigations at the core of this thesis both use thin-film YIG; we shall dedicate the next section of this chapter to examining its properties in detail.

2.2.2 Yttrium iron garnet (YIG)

Yttrium iron garnet is an $L = 0$, $g = 2$ (i.e. pure spin, see §1.3.1.3) electrically insulating ferrimagnet (resistivity $\rho \sim 10^{12}\,\Omega\,\mathrm{cm}$) with a cubic crystal structure (lattice constant $a_0 = 12.376\,\text{Å}$) and negligible magnetocrystalline anisotropy. Each unit cell of the material contains four formula units of $\mathrm{Y_3Fe_2^{3+}}\left(\mathrm{Fe^{3+}O_4^{2-}}\right)_3$, a total of 80 atoms. The twenty $J = 5/2$ $\mathrm{Fe^{3+}}$ magnetic ions occupy two antiferromagnetically coupled[3] lattices within the $\mathrm{O^{2-}}$ environment; one octahedral (8 ions) and one tetrahedral (12 ions). The exchange constant (as defined by Eqn. (1.66)) is $\lambda_{\mathrm{ex}} = 3 \times 10^{-16}\,\mathrm{m^2}$ [45].

Monocrystalline YIG has the narrowest ferromagnetic resonance (FMR) linewidth ΔH of any known practical experimental material, (typically $\Delta H = 40\,\mathrm{A\,m^{-1}}$ in thin-film samples), and therefore uniquely low spin-wave damping. A crude but useful quantitative estimate for the spin-wave propagation losses in thin-film samples is given by

$$A_{\mathrm{t}} = -10|\gamma\mu_0\Delta H| \log_{10} \mathrm{e}\,\mathrm{dB\,s^{-1}}, \tag{2.1}$$

which is approximately 38 dB per microsecond for the ΔH quoted above (note that γ here is in units of radians per second per Tesla).

The propagation of gigahertz-frequency magnetostatic spin waves with wavelengths in the micron to millimetre range is readily observed over centimetre distances

[3] Via superexchange, for a detailed description see Ref. [45].

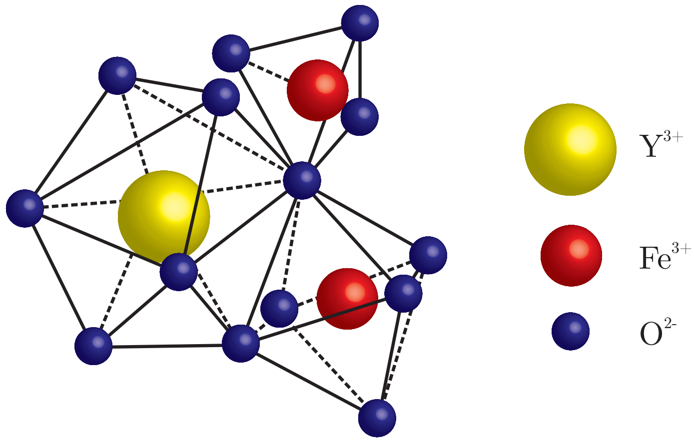

Figure 2.1: Yttrium iron garnet is an L=0 insulating ferrimagnet with a cubic crystal structure (lattice constant a_0 = 12.376 Å). Each unit cell contains four formula units of $Y_3Fe_2^{3+}\left(Fe^{3+}O_4^{2-}\right)_3$ with the twenty Fe^{3+} magnetic ions arranged in the O^{2-} environment on two antiferromagnetically coupled lattices, one octahedral (8 ions), one tetrahedral (12 ions). Monocrystalline YIG has the narrowest ferromagnetic resonance linewidth of any known practical experimental material and therefore uniquely low spin-wave damping.

in thin-film monocrystalline YIG making it an enormously enabling experimental material. In addition, the higher-order terms in the material's small-signal magnetic susceptibility are large, allowing non-linear spin-wave phenomena to be observed at input signal powers as low as 100 mW (see also §2.3.2).

In the experiments described in chapters 3 and 4, we employ monocrystalline YIG waveguides of approximate length 3 cm, width 2 mm, and thickness 5 µm. The films were produced by high-temperature liquid-phase epitaxy on gallium gadolinium garnet ($Gd_3Ga_5O_{12}$, GGG) substrates with their surface normals parallel to the $\langle 111 \rangle$ crystallographic axis. The lattice constant of GGG (12.383 Å) is very well matched to YIG, facilitating the growth of extremely high-quality stress-free films.

The saturation magnetization M_S of YIG takes a maximum value at 0 K of approximately 196 kA m^{-1}, reducing to around 140 kA m^{-1} at room temperature (298 K) and falling to zero at a Curie temperature $T_C = 559$ K. The relationship between M_S and T can be modelled by assuming that the magnetization of the material $\boldsymbol{M}$ is given by

$$\boldsymbol{M} = \boldsymbol{M}_1 + \boldsymbol{M}_2 \tag{2.2}$$

where $\boldsymbol{M}_1$ and $\boldsymbol{M}_2$ are the effective magnetizations of the iron sub-lattices, each of which originates an effective 'molecular field' $\boldsymbol{H}_{1,2}$ [16, 46]:

$$\boldsymbol{H}_1 = -\lambda_{11}\boldsymbol{M}_1 - \lambda_{12}\boldsymbol{M}_2, \tag{2.3a}$$

$$\boldsymbol{H}_2 = -\lambda_{21}\boldsymbol{M}_1 - \lambda_{22}\boldsymbol{M}_2. \tag{2.3b}$$

In the equations above the subscripts 1 and 2 identify the tetrahedral and octahedral lattices respectively, and the dimensionless coefficients λ_{ij} describe the strengths of the (nearest-neighbour) magnetic interactions within (λ_{11}, λ_{22}) and between ($\lambda_{12} = \lambda_{21}$) them. All four interactions are generally understood to be antiferromagnetic and therefore the coefficients are all positive numbers [45,46]. The cross-lattice interaction $\lambda_{12} = \lambda_{21}$ is the strongest by some considerable degree[4] and has the effect of frustrating the sub-lattices into states of ferromagnetic order.

Assuming $\boldsymbol{M}_1$ parallel to $\boldsymbol{M}$ and antiparallel to $\boldsymbol{M}_2$, Eqn. (2.2) can be reduced to a simple scalar sum

$$|\boldsymbol{M}| = M_\mathrm{S} = M_1 - M_2 \tag{2.4}$$

with

$$M_1 = |\boldsymbol{M}_1| = M_{1\mathrm{max}} B_{J_1}(f_1), \tag{2.5a}$$

$$M_2 = |\boldsymbol{M}_2| = M_{2\mathrm{max}} B_{J_2}(f_2), \tag{2.5b}$$

where $M_{1,2_\mathrm{max}}$ is the magnitude of the maximum ($T = 0\,\mathrm{K}$) effective magnetization of each sub-lattice having number density $N_{1,2}$ of Fe^{3+} $J = 5/2$ ion sites:

$$M_{1,2_\mathrm{max}} = |g\mu_\mathrm{B} N_{1,2} J|, \tag{2.6}$$

[4]Note that the cross-lattice nearest-neighbour distance $d_{12} = d_{21} = 3.46\,\text{Å}$ is shorter than the distance between adjacent ions on the tetrahedral ($d_{11} = 3.79\,\text{Å}$) and octahedral ($d_{22} = 5.37\,\text{Å}$) sub-lattices.

and $B_J\left(f_{1,2}\right)$ are the Brillouin functions

$$B_J\left(f_{1,2}\right)=\frac{2J+1}{2J}\coth\left(\frac{2J+1}{2J}f_{1,2}\right)-\frac{1}{2J}\coth\left(\frac{1}{2J}f_{1,2}\right) \tag{2.7}$$

for

$$f_1 = \tfrac{\mu_0\mu_1}{k_\mathrm{B}T}\left(H_0-\lambda_{11}M_1-\lambda_{12}M_2\right), \tag{2.8a}$$

$$f_2 = \tfrac{\mu_0\mu_2}{k_\mathrm{B}T}\left(H_0-\lambda_{21}M_1-\lambda_{22}M_2\right), \tag{2.8b}$$

where $\mu_{1,2}=|g|\mu_\mathrm{B}J$, and H_0 is the total (macroscopic) internal field.

Equations (2.5) do not have analytical solutions but can be solved graphically using the parameters listed in Table 2.1.

In an experimental context, it is often desirable to make use of an empirical approximation to YIG's M_S versus T relationship. Several approaches are possible and which is chosen depends largely on the range of temperatures of interest and the level of accuracy required. Solt has shown that a relationship of the form $M_\mathrm{S}(T)=M_\mathrm{Smax}\left(1-a_1T^{3/2}-a_2T^{5/2}\right)$ is a good model over the full temperature range 0 K to T_C [47], whilst over small temperature ranges a linear fit will often suffice.

Figure 2.2 shows an experimental M_S versus T curve (from the data of Anderson, Ref. [46]), in Fig. 2.3 these same data are plotted over the temperature range 250 K to 350 K (i.e. approximately fifty degrees Kelvin either side of room temperature). The data are well described by the linear fit

$$M_\mathrm{S}(T)=M_\mathrm{Smax}\left(1-1.2694\times10^{-3}T\right) \tag{2.9}$$

with $M_\mathrm{Smax}=224.12\,\mathrm{kA\,m^{-1}}$. Equation (2.9) predicts a room-temperature saturation magnetization $M_\mathrm{S}(298)=139.34\,\mathrm{kA\,m^{-1}}$ and a temperature effect of approximately $-0.285\,\mathrm{kA\,m^{-1}\,K^{-1}}$.

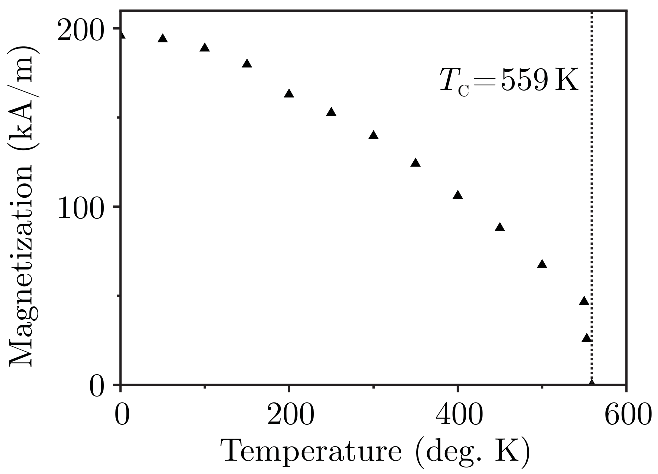

Figure 2.2: The saturation magnetization of yttrium iron garnet takes a maximum value at 0 K of approximately $196\,\mathrm{kA\,m^{-1}}$, reducing to approximately $140\,\mathrm{kA\,m^{-1}}$ at room temperature and falling to zero at a Curie temperature $T_C = 559\,\mathrm{K}$ (experimental data from Ref. [46]).

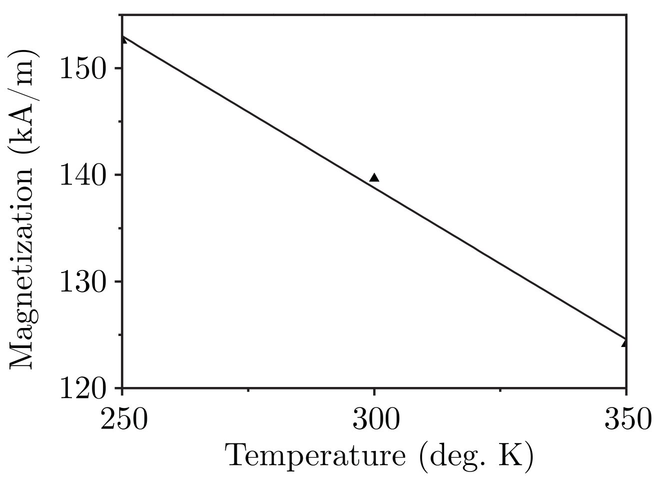

Figure 2.3: Over the temperature range 250 K to 350 K (i.e. approximately fifty degrees Kelvin either side of room temperature), the M_S versus T data shown in Fig. 2.2 are well described by a linear fit (Eqn. (2.9)).

Table 2.1: The properties of yttrium iron garnet [16].

Physical properties		
	Density (298 K)	$5172\,\mathrm{kg\,m^{-3}}$
a_0	Lattice constant (298 K)	12.376 Å
Macroscopic magnetic properties		
$M_{\mathrm{Smax}}(0)$	Saturation magnetization (0 K)	$196\,\mathrm{kA\,m^{-1}}$
$M_{\mathrm{Smax}}(298)$	Saturation magnetization (298 K)	$140\,\mathrm{kA\,m^{-1}}$
T_{C}	Curie Temperature	559 K
Microscopic magnetic properties		
Tetrahedral Iron sub-lattice		
N_1	Site density	$12.66 \times 10^{27}\,\mathrm{m^{-3}}$
g	Landé g-factor	2
J	Spin angular momentum per site	5/2
Octahedral Iron sub-lattice		
N_2	Site density	$8.44 \times 10^{27}\,\mathrm{m^{-3}}$
g	Landé g-factor	2
J	Spin angular momentum per site	5/2
Molecular field constants		
λ_{11}	Tetrahedral sub-lattice	344.59
λ_{22}	Octahedral sub-lattice	735.84
$\lambda_{12} = \lambda_{21}$	Cross-lattice	1100.3

2.2.3 The excitation and detection of spin waves in YIG

Spin waves can be excited and detected in YIG waveguides using inductive microwave antennae. The experiments of chapters 3 and 4 both employ arrangements of the type shown in Fig. 2.4(a). The antennae are short-circuited microstrip lines of a few tens of microns width lithographed 8 mm apart on the surface of an insulating substrate (typically aluminum nitride, AlN) on top of which the waveguide is placed or glued. The edges of the waveguide are sheared at around 45° so as to minimize coherent spin-wave reflections from the ends.

The particular focus of the studies presented in chapters 3 and 4 is the propagation of backward volume magnetostatic spin waves (BVMSW, §1.5.3.3). The excitation process for this category of wave is illustrated schematically in Fig. 2.4(b). When a microwave current is applied to the input antenna, the vertical component of the local magnetic field it produces exerts a time-varying torque on the spins in its vicinity, the mean precessional axes of which are aligned with the static bias field (see §1.2.2). If

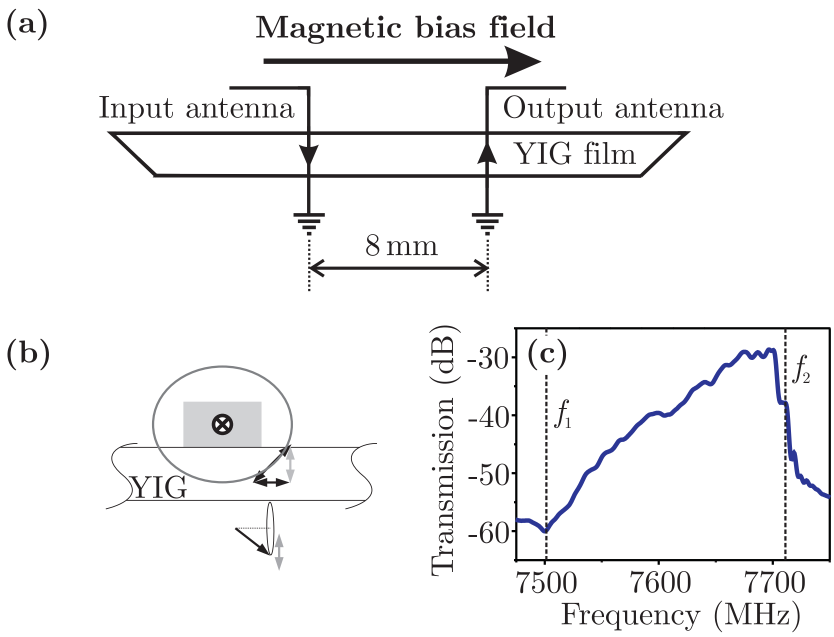

Figure 2.4: Spin waves may be excited and detected in YIG waveguides inductively using microwave antennae. (a) Schematic diagram of a typical waveguide/antenna system (plan view). A pair (input and output) of short-circuited microstrip lines are lithographed onto the surface of a dielectric substrate (typically aluminium nitride, AlN) on top of which the waveguide is placed. The edges of the waveguide are sheared at around 45° so as to minimize coherent reflections from the ends. (b) Schematic elevation of the region of the waveguide in the vicinity of the exciting antenna. The excitation process is illustrated for backward volume spin waves. The film is biased to saturation parallel to its long axis. When a microwave current is applied to the input antenna, the vertical component of the local magnetic field it produces exerts a time-varying torque on the spins in its vicinity, giving rise to a localized precessing magnetization which—if the frequency of the current falls within the spin-wave spectrum under the particular bias conditions—gives rise to a propagating wave. (c) A typical experimental BVMSW transmission characteristic of a YIG waveguide of length 8 mm subject to an on-axis magnetic bias field $B_A \simeq 200\,\mathrm{mT}$. The high-frequency limit of the spin-wave passband f_2 corresponds to the FMR frequency of the film, the low-frequency limit f_1 is determined by the antenna geometry.

the frequency of the current falls within the spin-wave spectrum under the particular biasing conditions, the local precessing magnetization which results gives rise to a propagating wave. In the BVMSW geometry, waves excited using this technique emanate from both sides of the antenna (i.e. to the left and to the right in Fig. 2.4(a)) with a relative phase of π radians [48] . The mechanism of spin-wave detection is—by symmetry—the inverse of the excitation process; when a spin wave arrives at the output antenna it induces in it a detectable microwave current.

Figure 2.4(c) shows a typical experimental BVMSW transmission characteristic for a YIG waveguide system of the type shown in Fig. 2.4(a). The data are obtained by connecting port 1 of a network analyser to the input antenna, port 2 to the output antenna, and measuring the parameter S_{21}. The high-frequency limit of the passband f_2 is the FMR frequency (the $k = 0$ spin-wave limit). The fall in transmission with reducing frequency is predominantly due to a reduction in the efficacy of the antennae as the spin-wave wavelength reduces. The low-frequency limit of the passband f_1 is determined by the antenna geometry; in general, the efficiency of excitation and detection are poor for waves having wavelengths significantly smaller than the antenna width. The insertion losses of the antennae vary depending on the geometry but are typically 3–10 dB (per antenna). The losses in the YIG are roughly constant across the passband and—for an 8 mm film section—are of order 12 dB. The background signal level of -60 to -55 dB is a measure of the direct electromagnetic interaction between the (unscreened) input and output antennae. Beating between this electromagnetic noise and the spin-wave signal typically results in spurious high-frequency texture in the data. In many experimental contexts it is sufficient to remove this texture by post-processing; however, if very precise measurements are required or measurements of very small signals are to be made the antennae must be screened.

2.3 The spin wave in context

With the benefit of the insight into spin-wave physics provided by chapter 1, we now set the scene for the experimental investigations of subsequent chapters by expanding on the observation made in the introductory chapter that spin waves propagating in thin-film magnetic materials are interesting both for their spin physics, and for their wave physics.

2.3.1 The spin wave as a magnetic phenomenon

2.3.1.1 The evolution of spin-wave science

Spin-wave physics began in 1930 with the theoretical work of Felix Bloch [49] and was elevated to the status of an experimental science in the late nineteen-forties by the discovery of ferromagnetic resonance by James Griffiths [22], and the work of Charles Kittel [50].

The synthesis of high-quality yttrium iron garnet brought about a first peak in experimental activity over the two decades between 1960 and 1980. The ability to transmit spin waves over centimetre distances in this remarkable new material inspired widespread belief in its potential to revolutionize microwave device manufacture. A range of innovative YIG based devices were produced during this period including isolators, filters, and oscillators, some of which remain in use today [51]. However, with the emergence of semiconductor technology, it soon became clear that YIG's role in the future of electronics was to be a minor, rather than a major one, and applied research activity contracted significantly. An enthusiasm for fundamental studies remained, but the scope of experimental work was restricted by the limitations of relatively coarse-grained analytical techniques.

Interest in magnon systems was reinvigorated in the early nineteen-nineties by the development and application of new experimental tools, most notably Brillouin

Light Scattering spectroscopy (BLS). BLS is an optical technique which enables highly sensitive wavevector-, time-, space-, and (in certain implementations) phase-, resolved mapping of magnon distributions and spin-wave propagation in magnetic samples [52–54]. Insights obtained and discoveries achieved through BLS have done much to stimulate the progression of both experimental and theoretical spin-wave science.

2.3.1.2 Magnonics and spintronics

Over the last decade, new fundamental understanding in combination with the increasingly widespread availability of micro- and nanofabrication has catalysed the emergence of 'magnonics': a new sub-field of spin-wave dynamics concerned specifically with fundamental and applied aspects of spin-wave propagation in magnetic thin films and nanostructures [1].

As a result of the short wavelengths characteristic of spin-wave excitations—typically microns to millimetres for magnetostatic waves and in the nanometre range for the exchange-dominated region of the spectrum—wave effects such as diffraction, interference, and geometrical mode formation can be observed in very small structures. Not only does the physics of these phenomena provide fascinating insight into fundamental magnetics, but it also attracts attention as a potential basis for magnetic devices [9, 55–62].

Latterly, the increasing visibility of magnonics has shone a spotlight on the potential importance of spin waves in the context of spintronics. Spintronics, or 'spin-transfer' electronics,[5] is the field of research concerned with the study and implementation of structures and devices which, unlike conventional electronic systems which rely exclusively on charge transport for their functionality, capitalize on spin-transport phenomena for information transfer, processing, and storage. Traditional spintronic architectures are based on the coding of information into spin-polarized

[5] Or, indeed, spin electronics.

electron currents [3–7]. Although substantial progress has been made, the development of systems based on this principle is impeded by the fact that spin-diffusion lengths—the distances over which spin information can be preserved—in practical materials are extremely short, a few hundred nanometres at best [5,8]. As a means to transport spin angular momentum over macroscopic distances at room temperature without charge transfer, spin waves open doors to spintronic information processing systems which operate with complete freedom from this constraint [2,9,63–65].

The exciting potential at the interface between magnonics and spintronics is further underlined by a broadening body of knowledge about the interplay between spin waves and charge currents. The spin-transfer torque [66], spin-pumping, and spin-Hall mechanisms together provide the means to convert back and forth between electrical voltages, spin-polarized electron currents, and spin waves [67–72]. This inter-conversion functionality paves the way for 'magnon spintronics', a new spintronic paradigm which combines the advantages of magnon based spin-information transfer and processing with the well established toolbox of electron spintronics.

Very recently, spin-wave systems have also begun to attract interest in connection with quantum-information science and processing. Though this thesis focuses entirely on the behaviour of spin waves in the classical limit, the development and exploration of systems which probe or make use of the excitations' underlying quantum mechanical personality is almost certain to play an influential role in shaping the field over the next decade. One example of a potential synergy between existing quantum information processing methodology and spin waves is in information storage and recovery. The possibility of storing and manipulating quantum information using collective states of spin ensembles has emerged as a prominent topic of interest within the quantum information community. Experimental work to date in this area has focused on systems in which the collective spin states concerned are those of ensembles of *isolated* spins [73–77]. Extending these principles to spin-wave systems—that is, systems in which the collective states are dispersive excitations of strongly coupled spin ensembles—would give access to novel and possibly advantageous storage functionalities. We might also speculate—if tentatively—that there could be much to be gained both intellectually and technologically from working to translate some of the established experimental geometries and 'tactics' of electron based quantum information science to the sphere of magnons; for example, quantum circuits which co-exploit quantum-electron and quantum-magnon dynamics could add a new and rich dimension to the future of this area of science [78].

2.3.2 The spin wave as a wave

The relationship between the dynamics of a spin wave and the environment in which it propagates is —in some aspects subtly, and in other aspects dramatically—different from other wave systems. Some differences are in underlying physics, they relate to what a spin wave *is*,[6] others are practical; they relate to what the experimentalist can *do* with spin-wave systems.

In order to alter the dispersion of a wave of a given frequency propagating through a given medium, it is necessary to make some change to the properties of the medium. In most wave systems, if the alteration is to be significant, this is a major undertaking. In the case of optical or acoustic waves for example, we are obliged to replace the wave medium with another which is physically distinct. Modifying the medium's environment—for example through the application of an electric or magnetic field, or a mechanical strain—may afford some control, but only as a second-order effect. Spin waves are unusual in that their dynamics can be directly controlled by changing the environment of the medium in which they propagate [59–61]. Relatively subtle

[6]Note that here, we do not make the claim that a spin wave acquires a special status simply by its being a magnetic wave rather than, for example, an acoustic or optical one. What is meant is that there are differences in the relationship between the parameters which define the wave in comparison with other systems. For example, the relationship between the dynamic magnetization and magnetic field distributions which define a spin wave is different from the relationship between the dynamic pressure and velocity distributions which define an acoustic one.

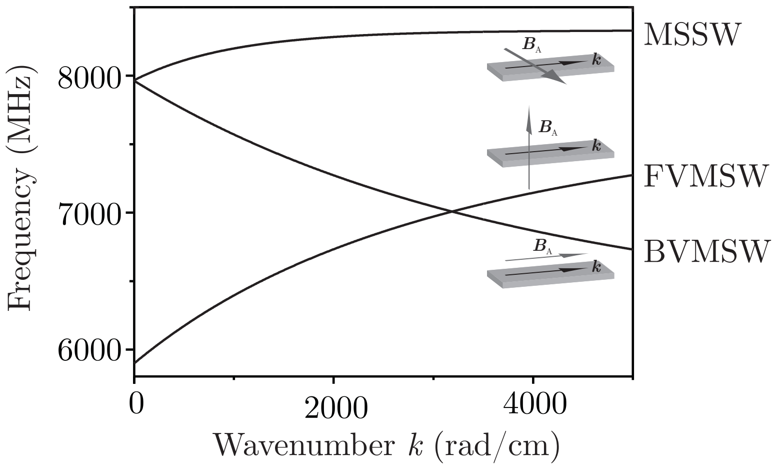

Figure 2.5: Three dispersion curves plotted using Eqns. (1.68), (1.72) and (1.76) for a YIG film of thickness 5 µm and saturation magnetization $M_S = 140\,\mathrm{kA\,m^{-1}}$. The curves correspond to magnetic bias fields oriented: in-plane and perpendicular to the spin-wave propagation direction (MSSW, upper curve), in-plane and parallel to the spin-wave propagation direction (BVMSW, middle curve), and out-of-plane (FVMSW, bottom curve). The MSSW and BVMSW curves are plotted for $B_A = 210\,\mathrm{mT}$ and the FVMSW curve for $B_A = 385\,\mathrm{mT}$ so that the internal field H_0 is the same in all three cases (see §1.5.3).

changes to the magnetic biasing conditions of thin-film spin-wave systems dramatically alter the characteristics of the signals which propagate through them. The dispersive properties of a wave of a given frequency can be transformed for example from positive (MSSW, FVMSW, §§1.5.3.1-2 and Fig. 2.5) to negative (BVMSW, §1.5.3.3 and Fig. 2.5) and its wavenumber tuned over two orders of magnitude, rapidly and reversibly using small current-controlled magnetic fields.

A further distinguishing feature of spin-wave systems is the fashion in and extent to which non-linearity flavours their dynamics. There are two sources of non-linearity in spin-wave systems: the intrinsic non-linearity of the Landau–Lifshitz equation (see §1.3.2) and material non-linearity (i.e. non-linearity in the small-signal magnetic response of a given spin-wave transmission medium). The power thresholds corresponding to the onset of non-linear behaviours in spin-wave systems are generally modest. This, combined with the richness of the spin-wave spectrum, makes it possible to observe a range of general non-linear wave effects which are very difficult to access controllably in other physical domains.

The non-linear thresholds in yttrium iron garnet are particularly low. The formation of spin-wave solitons [79], bullets (two-dimensional quasi-solitonic wavepackets) [80], and fractal [81] and chaotic [82, 83] processes can be observed in thin-film YIG samples using microwave input signal powers below 1 W. In addition, spin waves in YIG also provide a valuable model system for the experimental study of parametric amplification, and of non-linear signal-generation effects (see for example Refs. [84–86]).

To summarize, what the spin wave offers us might be described as a caricature of the wave paradigm: an exaggerated and distorted rendition of the wave behaviour we observe in other more familiar physical domains. By studying spin-wave systems we gain much more than knowledge about spin waves; we add fundamentally new depth to our understanding of the wave *concept*.

2.4 Metamaterials and the magnonic crystal

The experimental work described in chapters 3 and 4 centres around the study of spin-wave systems incorporating magnonic crystals. Magnonic crystals are the spin-wave embodiment of a general type of wave transmission structure known as an artificial crystal.

2.4.1 An introduction to the artificial crystal

The artificial crystal belongs to a category of synthetic media which have come to be known as 'metamaterials'; man-made materials with properties which are dominated (or at least strongly influenced) by an engineered mesoscopic texture or featuring which is superimposed on top of their natural atomic-scale or molecular structure. The defining attribute of an artificial crystal is an 'artificial lattice' in the form of a

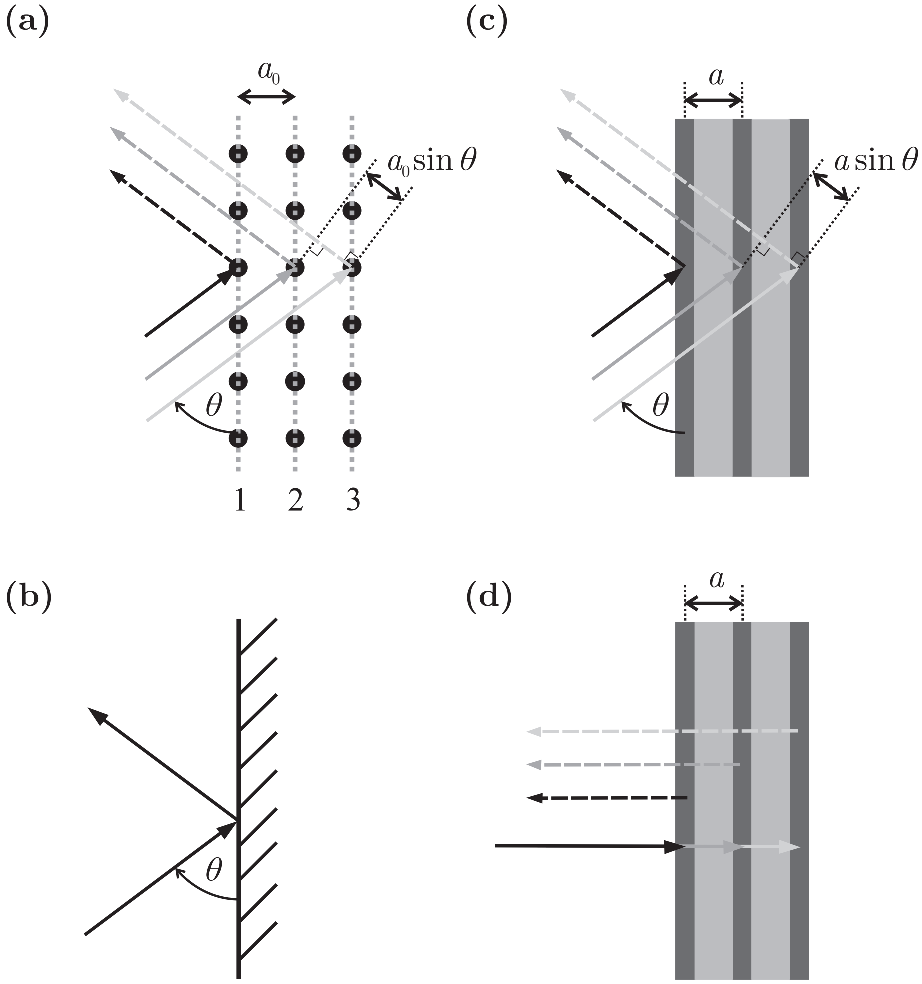

Figure 2.6: (a) The columns of black dots represent three planes, $p = 1, 2, 3$ of atoms in a real crystal. The lattice spacing is a_0. The arrow approaching from the left represents an incoming plane-wave beam from a coherent source, inclined at an angle θ to the crystal lattice. Upon striking the crystal, the beam interacts with the first plane of atoms and is partially reflected. What remains of its amplitude propagates on through the structure until it undergoes partial reflection from the second plane, and so on. The overall effect is the production of a 'total' reflected beam which is the superposition of waves which differ in effective path length by $2(p-1)a_0 \sin\theta$. (b) In the special case that the reflected waves in (a) add constructively, the net effect of the process of *distributed* reflection within the crystal is indistinguishable to the outside observer from one of *localized* reflection from a simple mirror located at the position of the first crystal plane. (c) In an artificial crystal, the role of the atomic crystal lattice of (a) is played by a mesoscale artificial one formed by layers or regions of material with different transmission properties. (d) The description and fabrication of magnonic crystals is complicated by the fact that the rules of geometrical reflection do not, in general, hold. One special context in which they do hold however, is for backward volume spin waves normally incident on a one-dimensional lattice, i.e. for $\theta = \pi/2$.

spatial periodicity in one or more of its material properties. The lattice gives rise to the appearance of interesting features in the structures' transmission spectra, notably band gaps: frequency intervals over which wave propagation is prohibited.

Band gap formation in an artificial crystal can be understood by analogy with the phenomenon of Bragg scattering encountered in the context of X-ray, neutron, and electron crystallography of natural crystals [87]. We shall explore this analogy with reference to the schematic of Fig. 2.6.

Each column of black dots connected by a grey dashed line on the right-hand side of Fig. 2.6(a), represents a plane of atoms in a real crystal. Three planes are shown ($p = 1, 2, 3$) with lattice spacing a_0. The arrow approaching from the left represents an incoming plane-wave beam of wavelength λ from a coherent source (for example an X-ray emitter) inclined at an angle θ to the crystal lattice. Upon striking the crystal, the beam interacts with the first plane of atoms and is partially reflected. What remains of the beam amplitude propagates on through the structure until it undergoes partial reflection from the second plane, and so on through the crystal. The overall effect is the production of a 'total' reflected beam that is the superposition of waves which—if we take the first plane of atoms $p = 1$ as a reference point—differ in effective path length by $2(p-1)a_0 \sin\theta$. In the special case that the waves add constructively, the net effect of the process of *distributed* reflection within the crystal is indistinguishable to the outside observer from one of *localized* reflection from a simple mirror located at the position of the first crystal plane Fig. 2.6(b). This condition is satisfied when

$$\lambda = \frac{2a_0}{n} \sin\theta \tag{2.10}$$

where $n = 1, 2, 3 \ldots$. Or, in terms of the wavenumber k of the wave

$$k = n\frac{\pi}{a_0}\frac{1}{\sin\theta}. \tag{2.11}$$

In the case of an artificial crystal, the role of the atomic crystal lattice of Fig. 2.6(a) is played by a mesoscale artificial one. The reflecting surfaces within an artificial crystal are not atomic planes, but interfaces between layers or regions of material with different transmission properties. This concept is represented in Fig. 2.6(c) for a one-dimensional artificial crystal of lattice constant a (two periods shown). For such a system, Eqn. (2.11) defines a series of band gaps centred on wavenumbers

$$k_{na} = n\frac{\pi}{a}\frac{1}{\sin\theta} \tag{2.12}$$

which are generally referred to as 'resonant' with the crystal lattice.

Several types of artificial crystal exist. Of these, optical photonic crystals are by far the most widely and intensively studied. A photonic crystal lattice is defined by refractive index variations in an optical transmission medium. The most common experimental systems operate with laser light and therefore have lattice constants of order microns [88–91]. Acoustic phononic crystals, which have lattices defined by density variations in acoustic transmission media, represent another important area of research activity. The field of phononic crystals is extremely diverse; crystals range from microscaled ultra-high-frequency constructions to audio frequency structures which are large enough to stand inside [92–97].

The field of *magnonic* crystals [61,98–107]—the particular focus of our attention—is an extremely new science. Although periodic spin-wave transmission media were studied in the late nineteen-seventies [108,109], the magnonic crystal concept was not recognized until around 2000 [100] and it was not until much more recently—perhaps the last three years—that work really began to gain momentum.

The strong directional anisotropy which characterizes the propagation of spin waves in externally biased waveguide systems makes the theoretical description of all but the simplest magnonic crystals a complex undertaking. The rules of geometrical reflection—which were implicitly assumed in the discussion of band gap formation presented above in connection with Fig. 2.6(a–c)—do not, in general, hold. One special context in which they do hold however, is for backward volume spin waves normally incident on a one-dimensional lattice, i.e. for $\theta = \pi/2$ (Fig. 2.6(d)). Under these conditions, for an artificial crystal of lattice spacing a, Eqn. (2.12) becomes

$$k_{na} = n\frac{\pi}{a}. \tag{2.13}$$

It is one-dimensional, normal incidence systems of this sort which are at the focus of the experimental work presented in chapters 3 and 4.

2.4.2 The fabrication of one-dimensional magnonic crystals

A one-dimensional magnonic crystal is essentially a spin-wave waveguide with magnetic properties which vary periodically as a function of distance along its axis. There are several ways in which this periodicity can be achieved. One option is to fabricate a waveguide composed of alternating segments of different magnetic material [105]. A second is to vary the geometry of the waveguide; either its width can be modulated [102,103], or a spatial periodicity in its thickness can be introduced [101,104,106]. Another approach involves introducing a spatial variation in the saturation magnetization of the waveguide material using, for example, surface acoustic waves [99]. A further possibility is to form a crystal by placing a homogenous waveguide in a spatially modulated magnetic field [61]. The experimental work presented in chapters 3 and 4 involves yttrium iron garnet based crystals produced using two of these four techniques.

The structure relevant to the work of chapter 3 is illustrated schematically in Fig. 2.7(a). This is a 'geometric' magnonic crystal comprising a YIG waveguide with a series of grooves patterned into its surface using a combination of lithography and hot

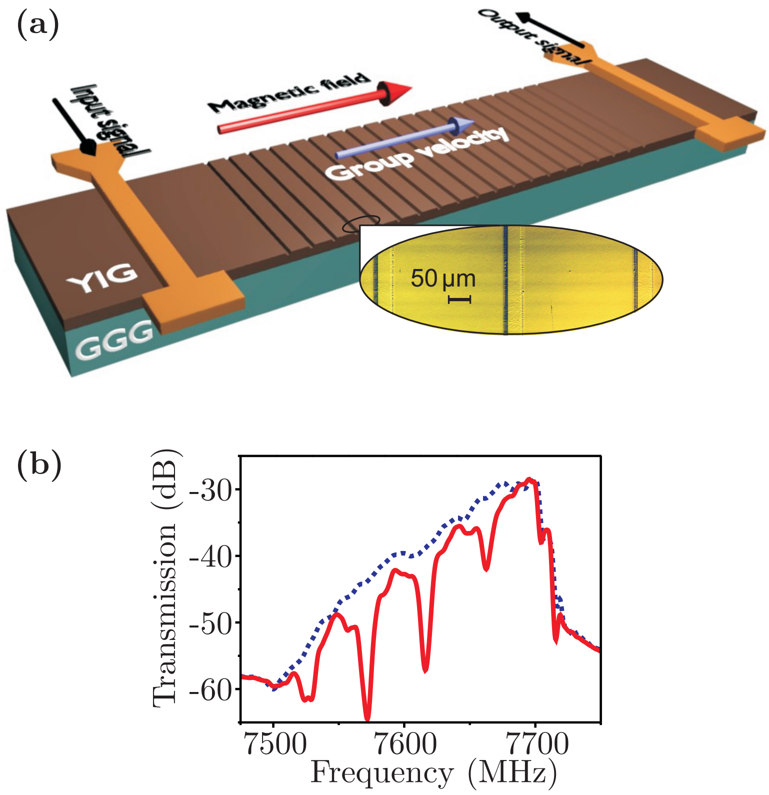

Figure 2.7: (a) The magnonic crystal employed in the experiments of chapter 3 features an etched, geometric artificial lattice. The structure comprises a YIG waveguide with a series of 10 grooves patterned into its surface using a combination of lithography and orthophosphoric acid etching. The grooves, which have a depth of 300 nm (5.5 % of the waveguide thickness), width 30 μm, and spacing 270 μm, define a crystal with a lattice constant $a = 300$ μm. Note that the schematic diagram shown here is of a crystal having 20 grooves. (b) The solid red line shows the experimental BVMSW transmission characteristics of the system of (a) for an applied magnetic bias field $B_{\mathrm{A}} \simeq 200$ mT. The blue dotted curve shows the properties of an un-patterned region of the same film. Three band gaps are clearly visible.

orthophosphoric acid etching [101]. The grooves, which have a depth of 300 nm (5.5 % of the waveguide thickness), width 30 μm, and spacing 270 μm, define a crystal with a lattice constant $a = 300$ μm. The experimental BVMSW transmission characteristics of the system are shown by the solid red line plotted in Fig. 2.7(b) for an applied magnetic bias field $B_{\mathrm{A}} \simeq 200$ mT. For reference, the blue dotted curve shows the

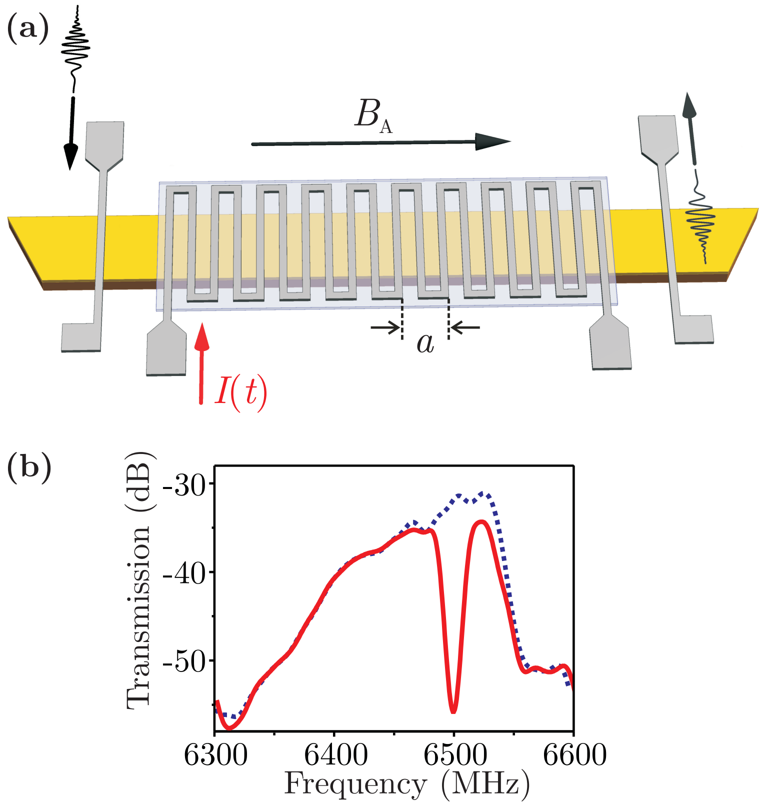

Figure 2.8: (a) The magnonic crystal used in the investigations of chapter 4 is a *dynamic* magnonic crystal (DMC). The lattice takes the form of a spatial modulation in the magnetic bias of a YIG waveguide created by the magnetic field from a current carrying 'meander' structure situated close to its surface. The lattice constant of the structure is the same as that of the etched crystal described with reference to Fig. 2.7: $a = 300\,\mu\mathrm{m}$. (b) The transmission characteristics of the DMC system with (solid, red) and without (dotted, blue) a current flowing in the meander structure for an applied magnetic bias field $B_A \simeq 210\,\mathrm{mT}$. When the current is applied a single band gap is observed.

properties of an un-patterned region of the same film. Band gaps corresponding to the first three solutions of Eqn. (2.13) are clearly visible. Note that because of the negative gradient of the BVMSW dispersion curve, the lowest-order gap is that with the highest frequency.

The magnonic crystal employed in chapter 4 is illustrated in Fig. 2.8(a). This crystal is of the fourth category alluded to above; the lattice takes the form of a spatial modulation in the magnetic bias of a YIG waveguide created by the magnetic field from a current carrying 'meander' structure situated close to its surface [61].

The transmission characteristics of the system are shown in Fig. 2.8(b), both with (solid, red) and without (dotted, blue) a current flowing in the meander structure. Here, in contrast with the structure of Fig. 2.7 just one band gap is present ($n = 1$, Eqn. (2.13)) since the lattice imposed by the field modulation has a sinusoidal—rather than a square—profile.

A key feature of the system depicted in Fig. 2.8 is the ability to turn the artificial lattice (and therefore the band gap) "on" and "off" on a timescale which is short compared with the time required for a spin-wave signal to propagate through it (approximately 300 ns). For this reason, we refer to the structure as a *dynamic* magnonic crystal (DMC). In the wider context of artificial crystals the functionality of this structure is unique. Whilst it is possible to create photonic crystals with properties that can be adjusted using external controls, the design and implementation of systems in which dramatic, rather than subtle, changes to the crystal lattice can be implemented is technically very challenging; the refractive index of photonic transmission media is not a parameter which can easily be modified reversibly, especially on optical timescales. Accordingly, as well as being an interesting structure from the specific point of view of spin-wave dynamics, this dynamic magnonic crystal provides unique experimental access to a new and largely unexplored area of *general* wave physics; the dynamic artificial crystal environment.

Chapter 3

The magnonic crystal meets the spin-wave self-oscillator

3.1 Introduction

3.1.1 The anatomy of the self-oscillator

'Self-' or 'auto-' oscillator is a general term used to describe positive-feedback structures of the form shown in Fig. 3.1. Such systems comprise a passive dynamic system with frequency response $G(\mathrm{i}\omega)$ with its output and input connected together via an active feedback network $K(\mathrm{i}\omega)$. The feedback network is designed so as to promote the generation and propagation of noise initiated signals around the loop. Depending on the characteristics of $G(\mathrm{i}\omega)$ and $K(\mathrm{i}\omega)$, these signals may be continuous or discontinuous, monochromatic or polychromatic, and either fully or quasi stable. We shall focus on continuous-wave self-oscillators which support stable, monochromatic oscillations.

The dynamic system $G(\mathrm{i}\omega)$ at the heart of a continuous-wave self-oscillator may take any form so long as (i) it is capable of supporting a continuous, finite-amplitude excitation at some $\omega \neq 0$ and (ii) the response of either it, or the feedback network,

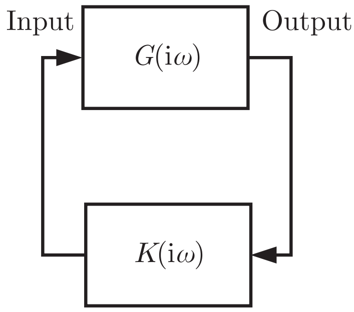

Figure 3.1: A self-oscillator is a closed-loop positive-feedback arrangement comprising two elements: a passive dynamic system with frequency response $G(\mathrm{i}\omega)$, and an active feedback network $K(\mathrm{i}\omega)$. The output and input of $G(\mathrm{i}\omega)$ are connected together via $K(\mathrm{i}\omega)$. In the case of a continuous-wave self-oscillator, the characteristics of the feedback network are such that at, and only at, a frequency ω_1, it delivers a gain $K = |K(\mathrm{i}\omega_1)|$ which exactly compensates for the loss $G = |G(\mathrm{i}\omega_1)|$ in the dynamic system, i.e. $|G(\mathrm{i}\omega_1)K(\mathrm{i}\omega_1)| = 1$, and the total loop phase shift $\angle G(\mathrm{i}\omega_1)K(\mathrm{i}\omega_1)$ is an integer multiple of 2π radians. To achieve stability at a unique frequency ω_1 the response of at least one of the elements in the loop must have a magnitude with a non-linear dependence on signal amplitude. When power is supplied to $K(\mathrm{i}\omega_1)$, noise initiated oscillations at ω_1 gradually build up around the loop. Eventually the loop signal reaches a steady-state amplitude through the action of the non-linearity.

has a magnitude with a non-linear dependence on signal amplitude.[1] The closed-loop system is arranged so that at, and only at, a single frequency ω_1, the total loop phase shift is an integer multiple of 2π radians (i.e. the signal phase is continuous around the loop) and the feedback network delivers a gain $K = |K(\mathrm{i}\omega_1)|$ which exactly compensates for the loss $G = |G(\mathrm{i}\omega_1)|$ in the dynamic system, that is,

$$G(\mathrm{i}\omega_1)K(\mathrm{i}\omega_1) = 1. \tag{3.1}$$

When power is supplied to the feedback network, noise initiated oscillations at ω_1 are preferentially amplified around the loop, and a coherent continuous signal at ω_1 rapidly builds in amplitude around it. Eventually, through the action of the non-linearity, the signal reaches a steady-state amplitude. Thenceforth, in the absence of perturbations to the loop, stable constant-amplitude oscillations persist indefinitely.

[1] Or both do, so long as the two non-linearities are non-repulsive.

3.1.2 The self-oscillator in context

Auto-oscillatory systems of the type shown in Fig. 3.1 are studied in a wide range of physical contexts. Most often, a non-linear electrical feedback network is employed which is interfaced with a linear dynamic system—for example an electrical, mechanical, or acoustic transmission structure—via input and output signal transducers (Fig. 3.3). Interest in such systems is motivated by several factors. Experimental study of the oscillation initiation and stabilization process can provide useful insight into the properties of the dynamic system in the loop. Unlike driven oscillator systems (Fig. 3.2) which rely on an external frequency source for excitation and therefore involve the *forced* oscillation of a dynamic system, the excitation of self-oscillators is entirely *unforced* and determined by the intrinsic dynamics of the components in the loop. If these dynamics change in time, the change will automatically lead to a measurable modification of the loop signal. As well as attracting general interest as a special class of signal environment, such loops therefore provide a useful means to study the

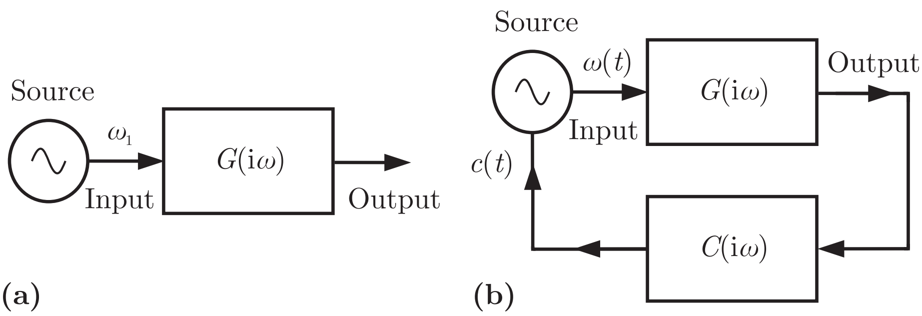

Figure 3.2: The operating characteristics of self-oscillating systems of the form shown in Fig. 3.1 are entirely distinct from those of driven oscillator systems. (a) The most simple driven oscillator is an open-loop system comprising a dynamic system $G(\mathrm{i}\omega)$ externally excited by a fixed-frequency source which operates at a frequency ω_1, generally arranged to coincide, or approximately coincide, with a resonance frequency of $G(\mathrm{i}\omega)$. (b) In closed-loop driven oscillator systems, a control system $C(\mathrm{i}\omega)$ responds to the output of $G(\mathrm{i}\omega)$ producing a control signal $c(t)$ which modifies the output characteristics of the source in such a way as to cause the closed-loop system to move toward a pre-defined operating point (generally a resonance frequency of $G(\mathrm{i}\omega)$).

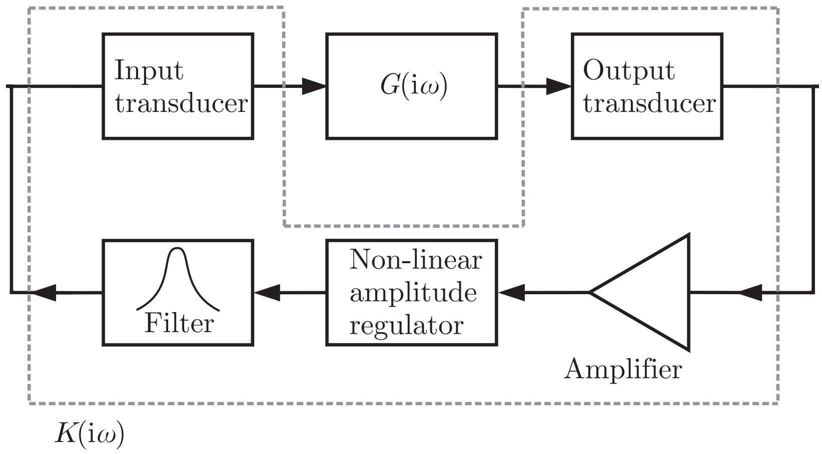

Figure 3.3: Many of the self-oscillating systems encountered in nature are spectacularly intricate mechano-chemical and/or electro-chemical structures. Those engineered by human hand tend to be rather less complex; their implementation is often motivated by an interest in the properties of the dynamic system $G(\mathrm{i}\omega)$ which might, for example be an electrical, mechanical, optical, or acoustic transmission system. Typical experimental arrangements employ a purely electrical feedback network $K(\mathrm{i}\omega)$ comprising a linear electronic amplifier, a non-linear amplitude regulator (for example a diode based clipper), and an electronic filter. In the case that $G(\mathrm{i}\omega)$ is not an electrical system, this network is interfaced with the dynamic system via input and output transducers.

dynamics of highly frequency selective (high-Q) resonant structures.[2] Studies of this sort are challenging using forced excitation owing to the difficulty of deconvolving the frequency response and stability characteristics of a driving source from the dynamics of the system under observation. Self-oscillators also find practical application in certain sensor and measurement instrumentation reliant on the frequency-tracking or monitoring of resonant phenomena [110]. The development and application of such instrumentation is an active research interest of the author, but will not be explored here [111–115].

Finally, it is interesting to note that positive-feedback oscillatory systems which reduce to the general form shown in Fig. 3.1 are commonplace in biological and bio-mechanochemical signalling systems (see for example Ref. [116] and references therein). Given Nature's uncompromising attitude to instrumentation design, this

[2] The quality factor or 'Q' of a resonance is a measure of its sharpness; it is defined as the ratio of its centre frequency to its $-3\,\mathrm{dB}$ width.

observation might be interpreted as the strongest of hints that there is much to be gained both intellectually and technologically from their study.

3.2 YIG based spin-wave self-oscillators

3.2.1 An introduction to spin-wave self-oscillators

Yttrium iron garnet based spin-wave self-oscillators—or ‘active rings’—have attracted interest within magnetics since the nineteen-nineties. Such systems not only offer unique insight into the dynamics of magnon systems, but also provide experimental access to a range of general wave phenomena which are not readily observable—or in some cases impossible to observe—in other physical domains. YIG based self-oscillators have made a significant contribution to the understanding of soliton [79, 117–119] (one dimensional self-stabilizing non-linear wave packets) and bullet [80,120] (two-dimensional soliton-like excitations) formation, as well as delivering interesting insights into fractal formation [81], and chaotic processes [82, 83].

The simplest spin-wave active-ring system comprises a slender thin-film YIG waveguide (typical thickness 4–5 μm, width 1.5–2 mm, and length 2–3 cm) with microstrip input and output spin-wave antennae positioned a distance L (typically 6–8 mm) apart on its surface. The antennae are connected via a feedback network comprising a microwave-frequency electronic amplifier, a variable attenuator to regulate the gain, and a phase shifter (phase φ). A magnetic bias field is applied to the YIG and its direction determines the class or classes of spin wave (i.e. MSSW, FVMSW, BVMSW or a combination of these) which can propagate through the magnetic system. Figure 3.4(a) is a schematic diagram of such ring arranged to support BVMSW and Fig. 3.4(b) shows the experimental spin-wave transmission characteristics of the waveguide inside it.

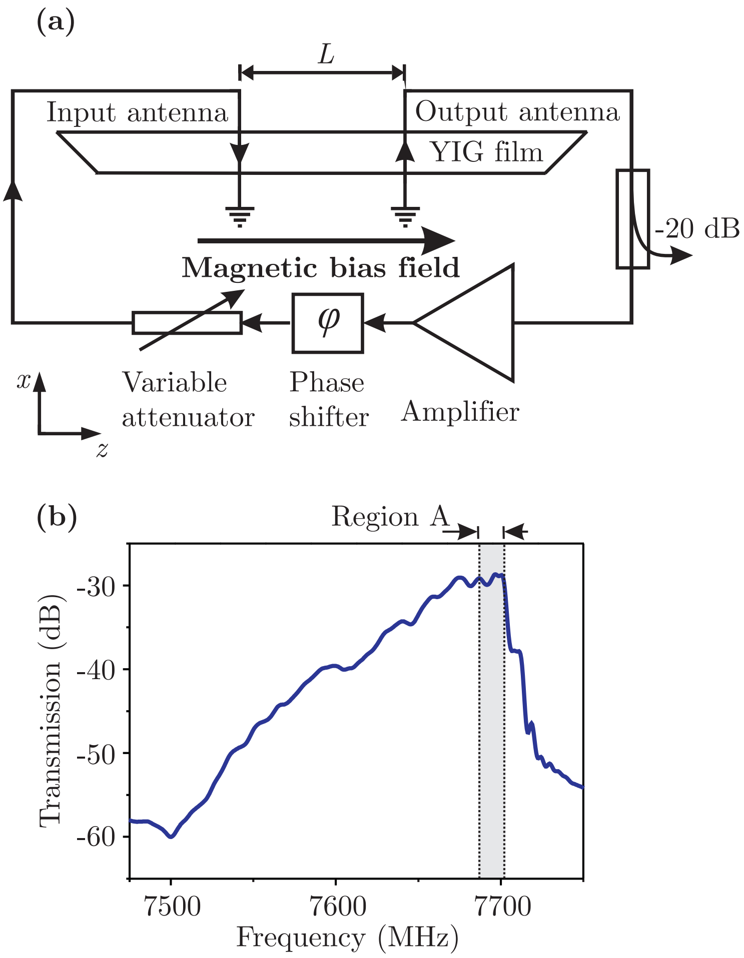

Figure 3.4: (a) Schematic diagram of a simple BVMSW active-ring system. Two microstrip antennae a distance L (typically 6–8 mm) apart excite (input, left) and detect (output, right) propagating spin waves in a thin-film YIG waveguide. A magnetic bias field is applied in-plane, parallel to the spin-wave propagation direction. (b) Experimental BVMSW transmission characteristics of a YIG waveguide arranged as in (a) subject to an applied magnetic bias field $B_A \simeq 200\,\mathrm{mT}$. These data were obtained by connecting port 1 of a network analyser to the input antenna, port 2 to the output antenna, and measuring the parameter S_{21}. The minimum loss (the sum of the insertion loss of the antennae and the spin-wave transmission loss) occurs over a band of frequencies typically of width $\sim 25\,\mathrm{MHz}$ (Region A), just below the maximum excitation frequency (the FMR frequency of the film). If the feedback gain in the loop of (a) is increased from zero by steadily reducing the attenuation in the ring, excitation initiates at a threshold value of feedback gain K_t. At this threshold, the ring signal is monochromatic and corresponds to the lowest-loss phase-feasible mode within Region A; its precise wavenumber however is essentially impossible to predict.

3.2.2 The excitation of YIG based spin-wave self-oscillators

The excitation of a simple YIG based spin-wave self-oscillator initiates at a threshold value of feedback gain K_{t}; the self-generation threshold. At this threshold, the ring signal is monochromatic, and its wavenumber $k = k_{\mathrm{d}}$ corresponds to the dominant (i.e. lowest-loss) phase-feasible mode,[3] the 'k_{d} mode'. In the ring shown in Fig. 3.4, this mode will be somewhere in the area identified by the shaded area (Region A) of the waveguide transmission characteristic.

The low non-linear threshold in YIG means that the non-linearity required to stabilize the ring can be provided by the magnetic waveguide itself (the equivalent of $G(\mathrm{i}\omega)$ in Fig. 3.1). The particular non-linear processes in the YIG which regulate the ring-signal amplitude depend strongly on the intensity of the spin-wave signal propagating in the waveguide and the biasing conditions. These two factors determine the manifold of allowable magnon frequencies and the type(s) of magnon splitting events which contribute to non-linear losses.

At low spin-wave powers, when the ring gain is equal to or close to K_{t}, the effect of the magnetic non-linearity is equivalent to an additional intensity-dependent loss in the waveguide which imposes a limit on the power of the k_{d} mode signal propagating around the ring. Under these conditions, the loop dynamics are equivalent to those of a system in which the intensity of the spin waves propagating in the waveguide has a linear dependence on the excitation power at the input antenna, and amplitude regulation is provided by a saturating electronic non-linearity in the feedback loop (cf. Fig. 3.3). If the gain is increased beyond K_{t} whilst the oscillator is running, the k_{d} mode initially acts as an energy sink, suppressing the excitation of all others.

[3] Note that in this and subsequent chapters, we deal exclusively with one-dimensional spin waves. More specifically, spin waves which propagate either parallel or antiparallel to a direction defined by the longitudinal axis of a spin-wave waveguide. We adopt the convention of defining this axis as the z-axis (as illustrated in Fig. 3.4) so that the wavevector $\boldsymbol{k} = k_z\hat{\mathbf{k}}$. To avoid unnecessary excess of bold type, we shall use the symbol k when we refer both to wave*number* ($k = |k_z|$) and wave*vector*. When it is used in the context of the latter, it should be interpreted as a scalar shorthand for the vector $\boldsymbol{k}$, i.e. $k = k_z$.

Once the gain exceeds a certain threshold however, the non-linear splitting of magnons corresponding to this mode starts to act as a pump; injecting sufficient energy into other regions of the spin-wave spectrum to initiate and sustain the oscillation of multiple phase-feasible modes around the ring. Once the ring signal has undergone the transition from the mono- to polychromatic regime, the evolution of its spectral content in response to further increase in gain K is extremely complex; it depends both on the subtleties of the magnetic properties of the waveguide and its magnetic environment, and the instantaneous spectral content of the ring signal.[4] However, notwithstanding these complexities, patterns in spectral evolution can be identified with certain specific biasing conditions and ring geometries so that—despite the quantitative uncertainty—qualitative modelling and analysis can be both successful and enlightening [79–83, 117–119].

3.3 Experimental motivations and methods

As outlined in §3.2.2, in a simple BVMSW active ring such as that shown in Fig. 3.4, the spin-wave mode excited at the self-generation threshold—the k_{d} mode—is the lowest-loss phase-feasible excitation which can propagate in the ring. From a knowledge of the transmission characteristics of the spin-wave waveguide in a given ring it is possible to estimate a frequency range within which this mode will fall. However, owing to the complex dependence of ring dynamics on a wide range of intrinsic and extrinsic experimental parameters, it is impossible to do so with precision. In a typical system, the best we might hope to achieve is to identify a frequency band of width around 25 MHz within which the mode is likely to appear. This is approximately three orders of magnitude larger than a typical mode width $\Delta\omega/2\pi = 25\,\mathrm{kHz}$. The *exact* wavenumber k_{d} is essentially impossible to predict.

[4] The spectrum of a ring signal $s(t)$ at a time $t_1 + \Delta t$ depends both on the combination $s(t_1 + \Delta t)$, $K(t_1 + \Delta t)$ and $s(t_1)$, $K(t_1)$.

Although certain aspects of spin-wave dynamics in active-ring structures have been studied extensively, the possibility of implementing and studying ring systems in which the threshold mode has a precise and well-defined wavenumber is not among them. We might expect to achieve a degree of modal selectivity by engineering the frequency response characteristics of the electrical feedback loop. However, such an approach is unexciting from the spin-wave dynamicist's perspective since it offers no new physical insight into the magnetic system at the heart of the oscillator. It is also impractical, since the ratio of the oscillator operating frequency ω to the mode width $\Delta\omega$ is typically of order 10^5, far in excess of the achievable Q of an electronic filter. A more attractive line of attack is one in which the selection of the threshold mode is achieved within the spin-wave system itself. Such an approach is not only interesting from the point of view of fundamental magnetics, but could be envisaged to find technological application in spin-wave spintronic devices.

In the experiments described in this chapter we demonstrate that by integrating a one-dimensional magnonic crystal structure into a spin-wave active ring, it is possible to force the ring to excite preferentially at a threshold mode $k_\mathrm{d} = k^*$ which takes a precise value determined by—and therefore readily predicted from—the geometrical properties of the crystal

3.3.1 Construction of the experimental magnonic crystal based spin-wave active ring

The experimental magnonic crystal based BVMSW active-ring system is shown schematically in Fig. 3.5 (note that, for reference, the exact component layout is illustrated in Fig. 3.6). Microstrip spin-wave input (left) and output (right) antennae of width $50\,\mu\mathrm{m}$, lithographed to the surface of an Aluminum Nitride (AlN) substrate, are in contact with the surface of the YIG waveguide which is subject to an on-axis magnetic bias field $B_\mathrm{A} = 202\,\mathrm{mT}$. The antennae are connected via an electrical feedback

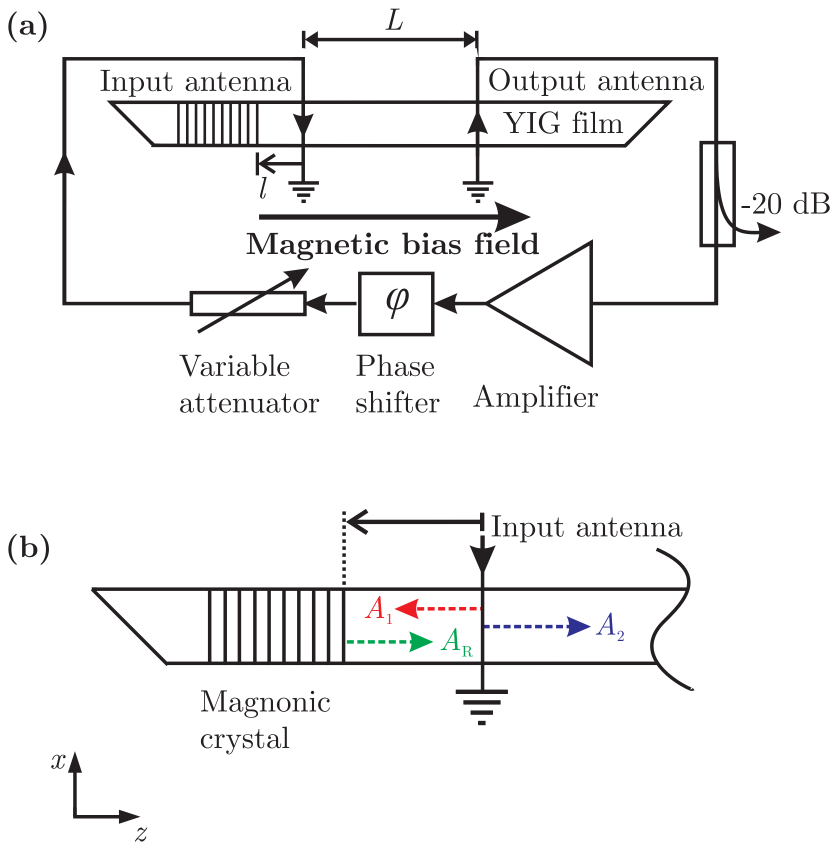

Figure 3.5: (a) Schematic diagram of the experimental BVMSW active-ring system. Two microstrip antennae (width 50 µm) a distance $L = 8\,\mathrm{mm}$ apart excite (input, left) and detect (output, right) propagating spin waves in a thin-film YIG waveguide. A magnonic crystal (lattice constant $a = 300\,\mathrm{\mu m}$) etched into the surface of the waveguide is positioned a distance l from the input antenna. The distance l can be varied over range $-3.5a < l < +3.5a$ with precision $\pm 5\,\mathrm{\mu m}$. The waveguide is subject to an applied magnetic bias field $B_{\mathrm{A}} = 202\,\mathrm{mT}$ (b) Expanded plan view (not to scale) of the region proximal to the input antenna. Half of the spin-wave power radiated from the input antenna propagates towards the output antenna (to the right in the diagram, complex amplitude A_2), the other half toward the magnonic crystal (to the left in the diagram, complex amplitude A_1). The left- and right-going signals have a relative phase of π radians. If the wavenumber k of the excited spin waves is an integer multiple of π/a the left-going signal is reflected from the magnonic crystal and a signal A_{R} propagates back toward the input antenna.

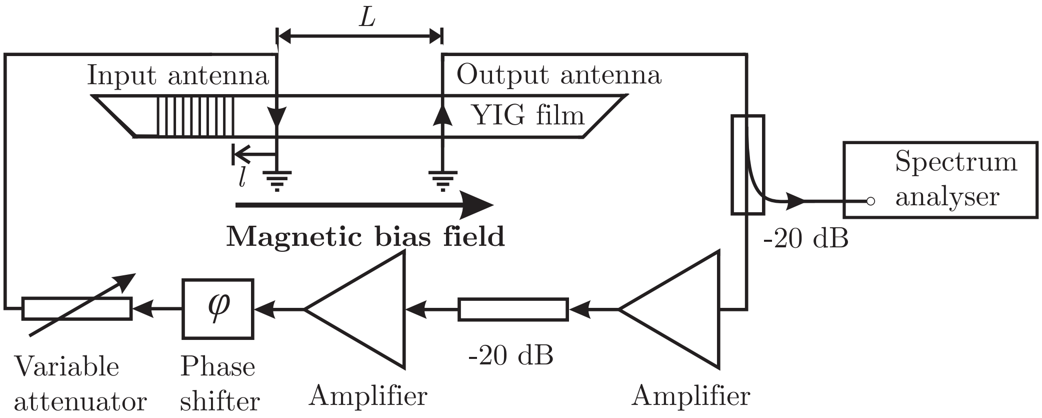

Figure 3.6: This figure shows the exact layout of components used to capture the data presented in this chapter. As can be seen, the system is identical in functionality to that shown in Fig. 3.5(a). However, rather than employing a single amplifier, two are connected in series via an attenuator (-20 dB). This configuration ensures that the non-linearity which stabilizes the ring is the magnetic non-linearity of the YIG waveguide, rather than an artefact of the electronic feedback. A spectrum analyser (Agilent E4446A, 3 Hz to 44 GHz) samples the signal in the loop via a -20 dB coupler.

network comprising a phase shifter (phase shift φ), an amplifier, a variable attenuator, and a directional coupler. The combination of the amplifier and the attenuator controls the feedback gain, whilst the coupler allows the ring signal to be sampled. The majority of the YIG waveguide is of uniform thickness ($d_0 = 5.5\,\mu\mathrm{m}$) but offset from its centre is a one-dimensional magnonic crystal comprising ten grooves of width 30 µm, depth 300 nm, and spacing 270 µm (lattice constant $a = 300\,\mu\mathrm{m}$) (see also §2.4.2). The crystal is positioned with its first groove a distance l from the input antenna. The distance l can be varied over a range $-3.5a < l < +3.5a$ with precision $\pm 5\,\mu\mathrm{m}$ by translating the waveguide relative to the antennae using a micropositioning stage.

If we assume that all of the phase shift in the electronic part of the feedback loop is included in the phase φ, the phase feasibility condition (corresponding to Eqn. (3.1)) is

$$\varphi - kL = 2\pi m \qquad \text{where} \quad m = 0, 1, 2, 3, \ldots \tag{3.2}$$

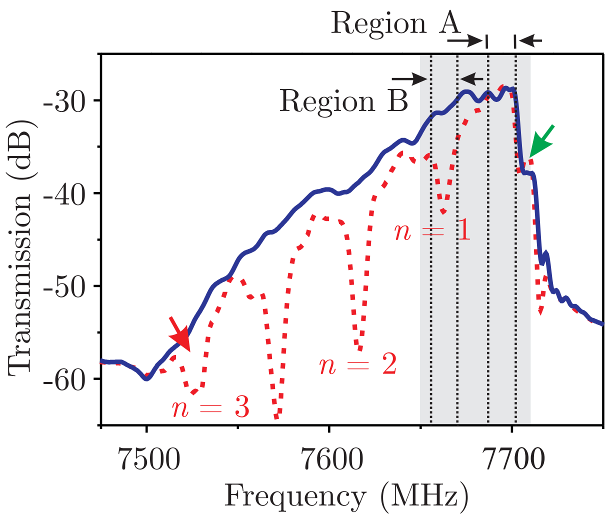

Figure 3.7: BVMSW transmission characteristics of the uniform (solid, blue) waveguide and the magnonic crystal (dotted, red) used in the study. The n^{th} order band gaps of the magnonic crystal are indicated. Region A identifies the lowest-loss region of the spin-wave passband of the uniform waveguide, Region B, the first band gap of the magnonic crystal. The depths and widths of the band gaps increase with increasing order as waves having higher wavenumbers scatter more efficiently from the grooves of the crystal. The small notch in the curves close to their high-frequency limit (green arrow) is associated with the first thickness mode of the YIG film. The gap-like structure close to the low-frequency limit of the passband (red arrow) is a measurement artefact caused by electromagnetic interaction between the spin-wave antennae.

where the negative sign of the second term on the left-hand side reflects the fact that the dispersion curve $\omega(k)$ for BVMSW has a negative gradient (see §1.5.3.3). As outlined in §2.4.2, the wavenumbers corresponding to the n^{th} BVMSW band gaps of the magnonic crystal are those which satisfy the 'Bragg' condition at normal incidence, that is:

$$k = n\frac{\pi}{a}, \qquad \text{where} \quad n = 1, 2, 3, 4, \ldots. \tag{3.3}$$

If spin waves with these k-values are incident on the crystal, they are reflected.

Figure 3.7 illustrates the BVMSW transmission characteristics of the homogeneous region of the waveguide (solid, blue) and the magnonic crystal (dotted, red). The FMR frequency is approximately 7710 MHz. Band gaps in the magnonic crystal transmission curve corresponding to $n = 1, 2, 3$ in Eqn. (3.3) are clearly visible. The depths and widths of the band gaps increase with increasing order since waves having higher wavenumbers (and therefore lower frequencies in the case of backward waves) scatter more efficiently from the grooves of the crystal [106]. Note that the small notch in the transmission curves close to their high-frequency limit indicated by the green arrow in the figure is associated with the first thickness (i.e. out-of-plane) mode of the YIG film. This feature often appears in waveguide transmission data (its depth and exact location depending on the precise parameters of the magnetic film) and has nothing to do with the presence of the magnonic crystal. The gap-like structure close to the low-frequency limit of the passband indicated by the red arrow is a measurement artefact caused by beating between superposed spin-wave and electromagnetic signals at the output antenna (see §2.2.3).

The low-loss region of the spin-wave passband just below the FMR frequency (Region A) and the first band gap of the magnonic crystal (Region B) will be the focus of the discussion which follows.

3.3.2 Excitation characteristics of the experimental magnonic crystal based spin-wave active ring

Upon excitation of the experimental active-ring system, the input antenna drives propagating spin waves both toward the output antenna (blue, complex amplitude A_2 in Fig. 3.5(b)) and toward the magnonic crystal (red, complex amplitude A_1). If the spin-wave wavenumber satisfies Eqn. (3.3), the waves incident on the magnonic crystal are reflected (green, complex amplitude A_{R}) and propagate back toward the input antenna. Note that the spacing of the antennae $L = 8\,\mathrm{mm}$ is long in comparison with the magnonic crystal lattice constant a, and of sufficient length to prevent any reflections from the output antenna back toward the magnonic crystal exerting an influence on the ring response, yet short enough that the effects of damping and decoherence along the spin-wave transmission path do not dominate the ring dynamics.

Left- and right-going waves have a relative phase of π radians [48]. It is also found experimentally that an effective phase shift of π (referenced to l), is associated with reflection from the magnonic crystal. Thus, the total phase accumulation of a reflected signal (satisfying Eqn. (3.3)) between transmission from the input antenna and arrival back at this point in the waveguide is $\varphi_l = 2k|l|$. It follows that if it can be arranged that

$$\varphi_l = 2\pi n \frac{|l|}{a} = 2\pi m, \qquad \text{where} \quad n = 1, 2, 3, 4, \ldots \quad \text{and} \quad m = 0, 1, 2, 3, \ldots, \tag{3.4}$$

the reflected signal will act to enhance the loop gain by a factor

$$H(R, l) = \frac{A_2 + A_{\mathrm{R}}}{A_2} = 1 + R\mathrm{e}^{-2\Gamma|l|}, \tag{3.5}$$

where R is an effective (complex) reflectivity of the magnonic crystal (referenced to A_2) and Γ is the per-unit-distance propagation loss. If the enhancement described by Eqn. (3.5) is sufficient to increase the effective ring gain in the vicinity of a band gap of the magnonic crystal over and above the value associated with the lowest-loss region of the passband of the uniform region of the waveguide (Region A, Fig. 3.7), then there is provided a mechanism by which a single mode—the wavenumber of which is rigidly fixed by the geometry of the magnonic crystal—may be preferentially excited at the self-generation threshold.

The maximum theoretical augmentation in loop gain attainable through wave-number selective reflection from the magnonic crystal is 3 dB. It is clear therefore from the data plotted in Fig. 3.7, that the only spin-wave modes which may be promoted to dominance using the enhancement mechanism in our particular experimental system are those which are associated with the first ($n = 1$) band gap (Region B, Fig. 3.7) since the transmission loss across the un-patterned waveguide at wavenumbers corresponding to higher-order gaps is at least 10 dB in excess of that associated with the lowest-loss region of the passband (Region A). From Eqn. (3.4), we predict an enhancement effect accessible for integer values of the ratio l/a associated with $k = k^* = \pi/a = 104.72\,\mathrm{rad\,cm^{-1}}$, which, under the conditions of the experiment, corresponds to a spin-wave frequency of 7663 MHz (Eqn. (1.76)).

3.4 Experimental results and discussion

3.4.1 Observation of wavenumber selective excitation in the magnonic crystal based spin-wave active ring

An expanded view of the transmission curves of Fig. 3.7 over the frequency range 7650–7710 MHz is shown in Fig. 3.8(a) (left ordinate axis). Overlaid, are experimental power spectra showing threshold modes corresponding to five values of the ratio l/a between approximately -3.5 ($l = -1.05$ mm) and $+3.5$ ($l = +1.05$ mm) (right ordinate axis). At each value of l, the feedback gain was increased via the attenuator (Fig. 3.6) from below the self-generation threshold (i.e. from an inactive state of the ring) to a value 5 dB above it, and a trace recorded. Each spectrum features a single peak at the frequency of the corresponding threshold mode. Note that the sharpness of the spectral peaks shown is limited by the scanning window of the spectrum analyser, their true width is ≤ 25 kHz. For integer values of l/a ($\pm 1.5\%$) the threshold modes $k_\mathrm{d} = k^*$ appear within the first band gap of the magnonic crystal (Region B). For general l/a, the wavenumber of the threshold mode k_d is determined solely by gain and phase feasibility conditions, and the modes lie in the lowest-loss region of the passband of the uniform waveguide (Region A), as in the case of the simple BVMSW ring shown in Fig. 3.4.

Figure 3.8(b) shows the dependence of the threshold mode frequency on the ratio l/a for a fixed phase shift in the feedback electronics φ (tuned for phase-feasibility in the region of k^*). Each point corresponds to a separate experiment performed using

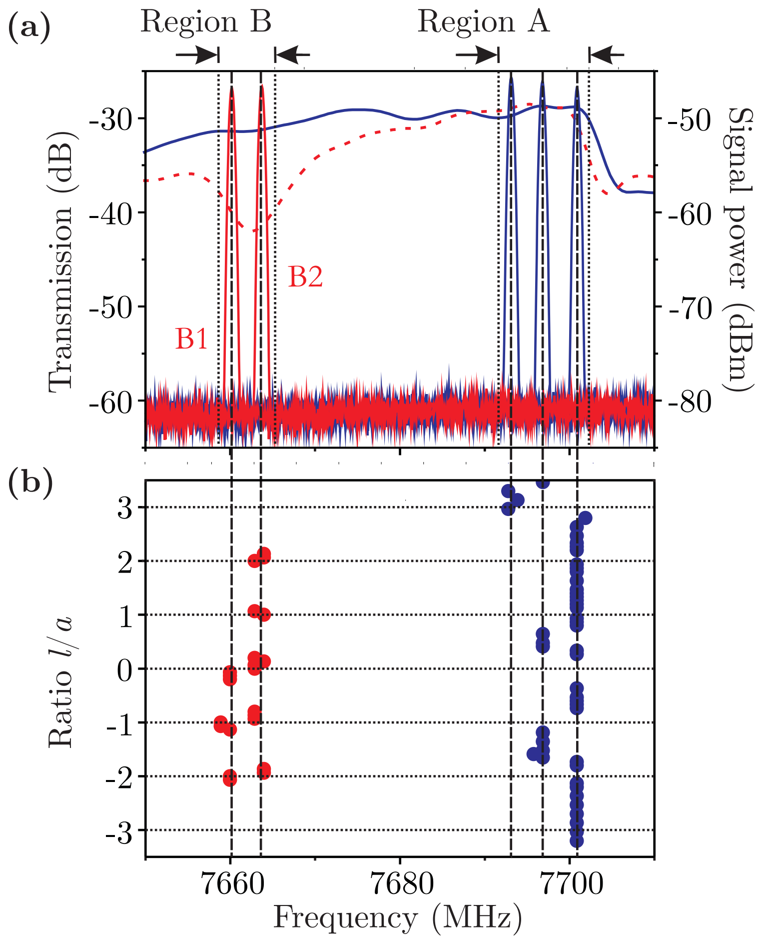

Figure 3.8: (a) The curves (left ordinate axis) show the transmission characteristics of the uniform region of the YIG waveguide (solid, blue) and the magnonic crystal (dotted, red) over the frequency range 7650–7710 MHz (the grey shaded region of Fig. 3.7). Overlaid are ring-signal power spectra captured via the -20 dB directional coupler shown in Fig. 3.6. Each spectrum comprises a single peak corresponding to the threshold mode. As indicated in (b), the three modes positioned within the lowest-loss region of the spin-wave passband (Region A) correspond to general values of the ratio l/a (blue circles), whilst the modes B1 and B2 which lie within the first band gap of the magnonic crystal at $k = k^*$ (Region B) are observed at and only at integer values (red circles). Note that dataset (b) has been compensated for the effects of small temperature variations during data collection.

an identical technique to that described in connection with the spectra of Fig. 3.8(a). The maximum positive integer value of l/a at which k^* mode promotion is observed is 2. Beyond this value, the loss associated with the signal path of the reflected wave reduces the loop gain at k^* below that for the lowest-loss mode associated with the uniform region of the waveguide. The horizontal dotted lines indicate integer values of l/a while the vertical dashed lines identify the datapoints with the individual Region A and Region B modes shown in Fig. 3.8(a).

Note that the data plotted in Fig. 3.8(b) were collected at a slightly lower temperature than those of Fig. 3.8(a). In order to compensate for these different conditions, a uniform horizontal shift of $-3\,\mathrm{MHz}$ has been applied to the Fig. 3.8(b) dataset. The theoretical curves of Fig. 3.9 illustrate that this shift is consistent with a temperature difference of less than 1 K. Plotted in Fig. 3.9 are the theoretical BVMSW dispersion curves for the YIG sample used in our experiments calculated using Eqn. (1.76) and Eqn. (2.9) for $T = 298\,\mathrm{K}$ (black) and $T = 297\,\mathrm{K}$ (grey). To achieve a good fit to experimental data ($k = k^* = 104.72\,\mathrm{rad\,cm^{-1}}$ at 7663 MHz for $T = 298\,\mathrm{K}$) the bias field has been used as a fitting parameter (data are plotted for $B_\mathrm{A} = 201.525\,\mathrm{mT}$, rather than the nominal value $B_\mathrm{A} = 202\,\mathrm{mT}$). The vertical offset between the two lines is approximately 3.6 MHz.

Each distinct accessible mode of the active-ring system corresponds to a unique solution of Eqn. (3.1). Since the phase accumulation around the loop is directly proportional to the wavenumber, in an ideal system, for fixed electronic phase shift φ, we would expect to observe just two threshold modes: one at integer l/a corresponding to k^*, and one for general l/a at a single but undefined k-value in the low-loss region of the passband of the un-patterned part of the waveguide (Region A, Fig. 3.8). In the experiments, several modes (3) are observed in Region A for non-integer l/a. The multiplicity of modes is attributed to the fact that owing to the tolerances of the growth process, the thickness of the YIG waveguide varies slightly along its length.

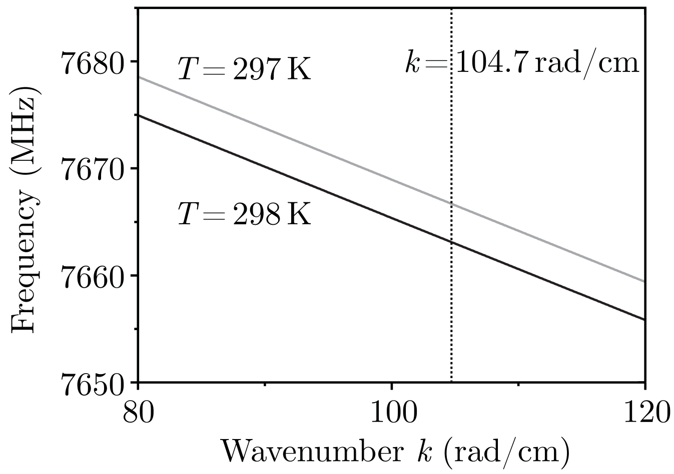

Figure 3.9: Theoretical BVMSW dispersion curves for the YIG waveguide used in our experiments showing the effect of temperature variations. The curves are plotted using Eqn. (1.76) and Eqn. (2.9) for $T = 298\,\mathrm{K}$ (black) and $T = 297\,\mathrm{K}$ (grey). To achieve a good fit to experimental data ($k = k^* = 104.72\,\mathrm{rad\,cm^{-1}}$ at $7663\,\mathrm{MHz}$ for $T = 298\,\mathrm{K}$) the bias field has been used as a fitting parameter (data are plotted for $B_\mathrm{A} = 201.525\,\mathrm{mT}$, rather than the nominal value $B_\mathrm{A} = 202\,\mathrm{mT}$).

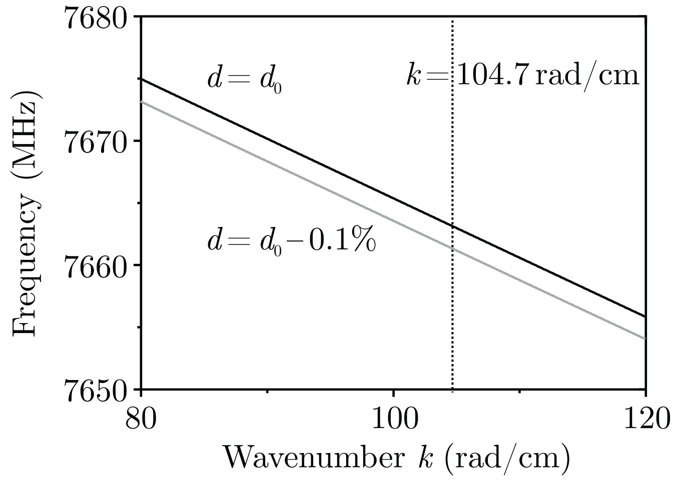

Figure 3.10: Theoretical BVMSW dispersion curves for the YIG waveguide used in our experiments showing the influence of non-uniform film thickness. The curves are plotted using Eqn. (1.76) and Eqn. (2.9) for $T = 298\,\mathrm{K}$, $B_\mathrm{A} = 201.525\,\mathrm{mT}$ and waveguide thicknesses of $d = d_0 = 5.5\,\mu\mathrm{m}$ (black) and $d = d_0 - 0.1\,\% = 5.4945\,\mu\mathrm{m}$ (grey). The vertical offset between the curves is $1.7\,\mathrm{MHz}$.

The dispersion relationship $\omega(k)$ for spin waves travelling between the antennae therefore depends on the particular 8 mm section of YIG waveguide in the loop, and thus the value of l, providing a secondary mechanism for the phase accumulation around the loop to vary independently of φ.[5] In order to quantify the effect of thickness variations, in Fig. 3.10 we compare the theoretical dispersion curves for $d = d_0 = 5.5\,\mu\text{m}$ (black) and $d = 5.4945\,\mu\text{m}$ (grey) under the conditions of our experiments (the $d = d_0$ curve is identical to the $T = 298\,\text{K}$ curve of Fig. 3.9). The calculated data demonstrate that a change in effective thickness of just 0.1 % is sufficient to shift the frequency corresponding to the resonant wavenumber k_a by 1.7 MHz.

The mode selection capability of the magnonic crystal system is observed at $l = 0$ and extends to negative integer values of l/a (i.e. values corresponding to the magnonic crystal entering the region between the antennae). A single mode within the $n = 1$ band gap, labelled B2 in Fig. 3.8(a) is associated with $l/a = +1, +2$. This mode is considered the 'strict' k^* mode. At $l/a = 0, -1, -2$ a second mode, labelled B1 in the same figure, is also observed. The presence of mode B1 is attributed to a combination of the effects of non-uniform film thickness discussed above, a high effective signal enhancement efficiency associated with $l/a = 0, -1, -2$ loop configurations and, in the case of $l/a = -1, -2$, bi-directional reflection of spin waves at the input antenna. It is likely that in the region of $l/a = 0, -1, -2$, there is non-negligible signal enhancement over a range of spin-wave wavenumbers within the $n = 1$ band gap including that corresponding to mode B1, which—by virtue of the non-uniform thickness effect—satisfies phase-feasibility at certain values of l/a. Confirmation of this hypothesis would demand spatially resolved characterization of spin-wave propagation in the ring. Such a study might in future be undertaken using Brillouin light scattering spectroscopy but is beyond the scope of the experiments presented here.

[5] Partial reflection of spin waves at the output antenna potentially introduces a further unmodelled source of phase shift (and effective loss) in the loop but this effect—if present at all—is insufficiently pronounced to affect the experimental results.

3.4.2 Polychromatic excitation spectra of the magnonic crystal based spin-wave active ring

For interest, Figs. 3.11 and 3.12 show the excitation spectra of the magnonic crystal based active ring for a non-integer value of $l/a = 0.93$ (Fig. 3.11), and $l/a = 0$ (Fig. 3.12), as the feedback gain is varied from a value K_0 in the monomode, low-gain regime (a)—the focus of the work presented in this chapter—to a value 20 dB above this level (f). Given the considerations of §3.2.2 we should not expect to be able to draw detailed conclusions from these datasets; however, it is interesting to compare the two. One particular qualitative distinction stands out: in the multimode regime at

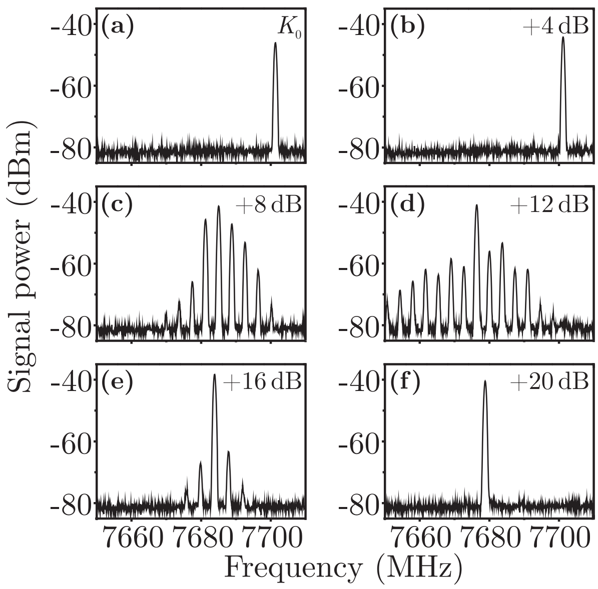

Figure 3.11: Excitation spectra of the magnonic crystal based active ring (Fig. 3.6) for $l/a = 0.93$ (i.e. non-integer l/a) as the feedback gain is varied from a value K_0 a little above the self-generation threshold (a) to a value 20 dB above this (f). The frequency of the dominant mode (the single mode observed in (a) and (b)) lies in the lowest-loss region of the spin-wave passband of the waveguide included in the loop (Region A, Fig. 3.7). Monomode excitation persists ((a) and (b)) until a second threshold beyond which non-linear splitting processes drive excitations at multiple k values. The subsequent evolution of the spectrum includes multi- and monomode regimes ((c) to (f)). Note that the sharpness of the spectral peaks shown is limited by the scanning window of the spectrum analyser, their true width is ≤ 25 kHz.

$K = K_0 + 8\,\mathrm{dB}$, in the $l/a = 0.93$ case (Fig. 3.11(c)) there is a single cluster of modes in the lowest-loss region of the passband of the waveguide around 7700 MHz (Region A, Fig.3.7). In the corresponding case for the $l/a = 0$ configuration (Fig. 3.12(c)) a second group appears in the vicinity of the geometrically enhanced mode k^*. This suggests that the process of spectral 'pumping' which leads to the excitation of multiple modes is limited to the low-loss region of the waveguide passband (Region A, Fig. 3.7) in the former case, but occurs both over this region and in the vicinity of k^* (Region B, Fig. 3.7) in the latter.

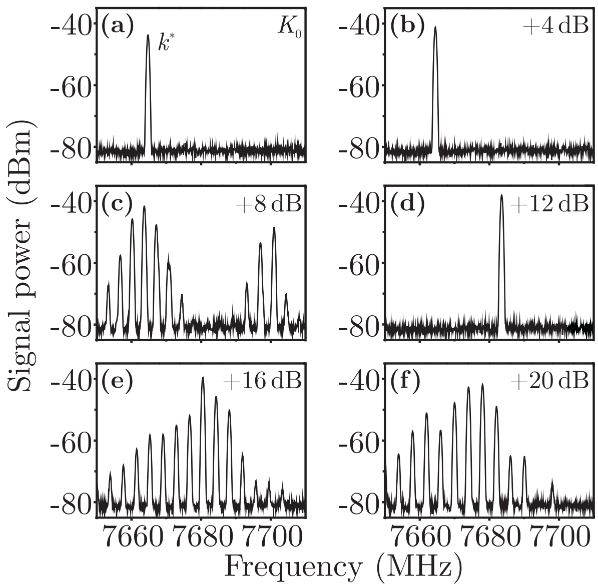

Figure 3.12: Excitation spectra of the magnonic crystal based active ring (Fig. 3.6) for $l/a = 0$ as the feedback gain is varied from a starting value K_0 a little above the self-generation threshold (a) to a value 20 dB above this (f). It is interesting to compare these data with those shown in Fig. 3.11 (collected for the same ring for non-integer l/a). In the multimode regime at $K = K_0 + 8\,\mathrm{dB}$ in the $l/a = 0.93$ case (Fig. 3.11(c)) there is a single cluster of modes in the lowest-loss region of the passband of the waveguide around 7700 MHz (Region A, Fig.3.7). In the corresponding case in the data above a second group appears in the vicinity of the geometrically enhanced mode k^*. Note that the sharpness of the spectral peaks shown is limited by the scanning window of the spectrum analyser, their true width is $\leq 25\,\mathrm{kHz}$.

3.4.3 Concluding remarks

In the experimental investigations presented in this chapter we have explored a YIG based BVMSW spin-wave active ring incorporating a one-dimensional magnonic crystal. We have demonstrated that a signal enhancement mechanism reliant on the wavenumber dependent reflectivity of the crystal and the ring geometry can be used to force the ring to excite preferentially at a mode determined by, and therefore readily predicted from, the geometrical properties of the crystal.

The outcomes of our experiments hint that spin-wave active-ring systems incorporating magnonic crystals may be an interesting new direction in fundamental and applied magnonics. Such systems might be expected to make a contribution both to the general field of self-oscillators and to our understanding of spin-wave propagation and scattering processes in magnonic crystals.

An obvious extension of the work reported in this chapter would broaden investigations to magnonic crystal based ring systems having different geometries and subject to different biasing conditions, both in mono- and polychromatic excitation regimes. Such studies could unlock new insight into the relationship between the mesoscopic structure of magnonic crystals and the magnon scattering events which occur inside them at high signal powers. The same work might be anticipated to lead to the development of active rings having mode-selection rules and functionality which are of general relevance and interest to self-oscillator science.

Moreover, on a practical level, the particular wavenumber selective signal enhancement mechanism we have observed could lend functionality to spin-wave self-oscillator systems in future magnonic and spintronic devices, such as fixed-frequency sources, logic structures, and sensors [121, 122].

Chapter 4

Time reversal by dynamic magnonic crystal (DMC)

4.1 Introduction

Using software based signal processing, the conversion between a time-dependent signal $A(t)$ and a time-reversed version of this signal $A(-t)$ is—so long as the signal can be captured and stored electronically—a trivial procedure. Whilst the detail of the operation is technically impressive; it has little to offer those in search of interesting physics. However, the possibility of realizing the same conversion through direct physical means—i.e. via a process with a physical description which *implies* the implementation of the operation $A(t) \rightarrow A(-t)$—is very intellectually enticing indeed. The idea not only encapsulates an intriguing scientific possibility, but raises profound philosophical questions about the structure of the temporal canvas upon which our physical world is painted [123].

4.1.1 The mathematics of time reversal

The process of time reversal is equivalent to the inversion of a signal's spectrum about a reference frequency [124]. This is a fact best appreciated by considering the Fourier domain description of an arbitrary signal envelope $A(t)$:

$$A(t) = \sum_{-\infty}^{\infty} A_m \mathrm{e}^{\mathrm{i}(\omega_\mathrm{R} - \omega_m)t} \tag{4.1}$$

where ω_R is a reference frequency which may take any value (including zero), and the sum is over all the spectral components ω_m. The time-reversed envelope is then described by

$$A(-t) = \sum_{-\infty}^{\infty} A_m \mathrm{e}^{-\mathrm{i}(\omega_\mathrm{R} - \omega_m)t} \tag{4.2}$$

from which we see that the operation $t \to -t$ is indistinguishable from the operation $(\omega_\mathrm{R} - \omega_m) \to -(\omega_\mathrm{R} - \omega_m)$ i.e. an inversion of the spectrum about ω_R. It follows that if a time-reversed signal $A(-t)$ is to be produced directly from a signal $A(t)$, we require a physical process capable of achieving spectral transformation; that is, either a piece of *non*-linear or *non*-stationary physics.

All experimentally verified time-reversal mechanisms which pre-date the work described in this chapter depend upon non-linear mixing for their operation (see for example Refs. [86, 125–127]). Although elegant pieces of physics, the study and practical application of these techniques is complicated by the fact that the majority of real materials exhibit only weak non-linearity. Such processes (which include for example optical four-wave mixing) require large energy densities and/or operate through the exploitation of resonant enhancement or absorption phenomena which place fundamental restrictions on their bandwidth. Despite these challenges, potential non-stationary routes to time reversal have, until very recently, remained entirely unexplored.

4.1.2 Time reversal in the artificial crystal environment

With the turn of the last century came an emerging interest within the optics community in creating dynamic photonic crystals: photonic crystal structures with time-dependent properties [124, 128–135]. It was soon established that such systems could theoretically provide the means to perform spectral operations including frequency transformations (i.e. the shifting of optical energy from one frequency to another) in perfectly linear wave transmission media. In particular, a number of linear mechanisms of time reversal based on, for example, Bloch oscillations [134], and refractive index- or loss- tuning of coupled cavity waveguides were proposed [124, 128]. As well as attracting attention as specific and interesting developments in the context of theoretical photonics, this work served to underline a more general point: that time-varying artificial crystal environments—a new direction in the science of wave dynamics and wave-based signal processing—present unique opportunities for the manipulation of propagating waves. However, the practical challenges associated with the realization of dynamic photonic crystal structures (see §2.4) mean that the optical signal processing mechanisms alluded to above remain, as yet, beyond experimental reach.

This chapter describes the use of a dynamic magnonic crystal to achieve the experimental realization of an entirely general, linear, non-stationary time-reversal mechanism based on the dynamic control of an artificial crystal structure [62]. The physical basis for the mechanism is a previously unforeseen phenomenon of oscillatory energy exchange between wave modes coupled by the artificial crystal lattice.

4.2 An experimental dynamic magnonic crystal

A photograph of the experimental spin-wave system, illustrated schematically in Fig. 4.1(a), is shown in Fig. 4.1(b). The one-dimensional dynamic magnonic crystal (DMC) comprises a planar metallic meander structure (period $a = 300\,\mu\text{m}$, total

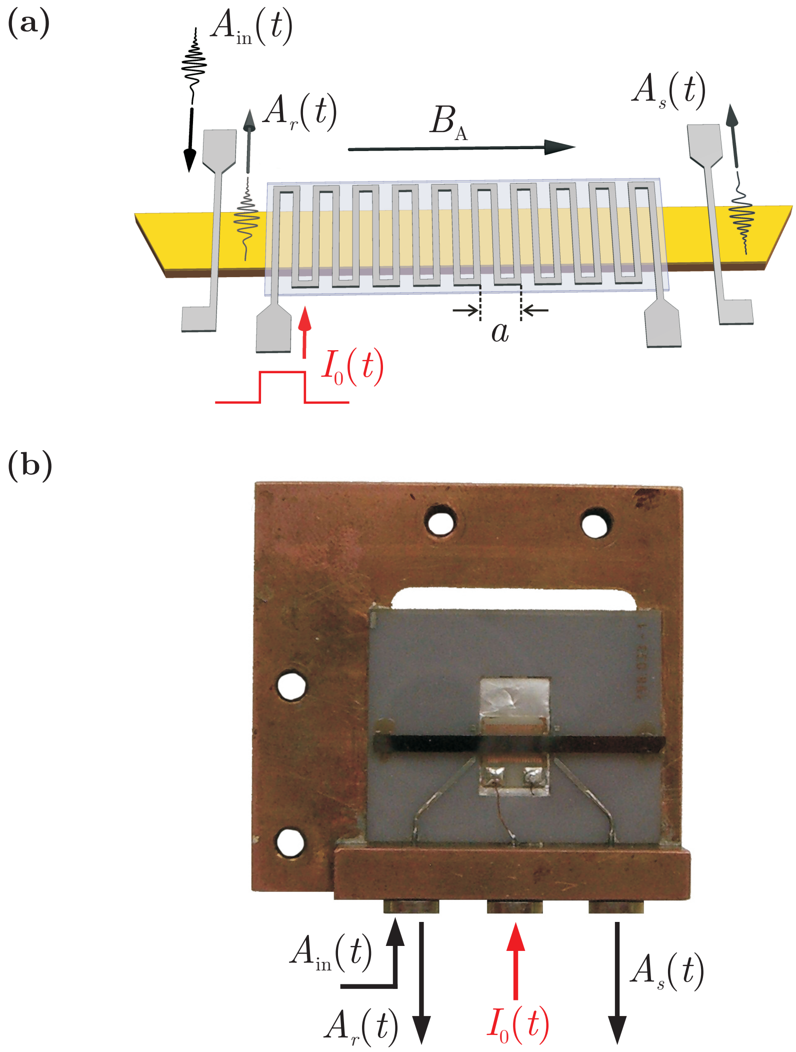

Figure 4.1: (a) Schematic diagram of the experimental spin-wave system. The dynamic magnonic crystal (DMC) comprises a metallic meander structure with 20 periods of lattice constant a (10 shown) separated from the surface of a YIG spin-wave waveguide by a 100 µm SiO_2 spacer layer. Microstrip input (left) and output (right) antennae are in contact with the surface of the film and a magnetic bias field B_{A} is applied along the axis of the waveguide so as to support the propagation of BVMSW. In the absence of a current flowing through the meander structure, the transmission characteristics of the system are those of a uniform YIG waveguide and the DMC is “off”. If a current $I_0(t)$ is applied, the spatially periodic magnetic field it produces leads to a variation in the spin-wave transmission characteristics of the waveguide with spatial periodicity a, and thus the appearance of a band gap in the transmission spectrum (Fig. 4.2). (b) A photograph of the experimental DMC system mounted in a copper sample holder. The brown stripe running from left to right is the YIG waveguide which is glued to the grey dielectric square (AlN). (Note that the YIG waveguide through which the spin waves propagate is on the underside of the stripe). The meander structure is visible underneath the waveguide, as are the microstrip input and output antennae.

length $L_c = 6\,\mathrm{mm}$) separated from the surface of a YIG waveguide of thickness $5\,\mu\mathrm{m}$ by a $100\,\mu\mathrm{m}$ SiO_2 spacer layer. Microstrip spin-wave antennae are provided at each end of the crystal ($L = 8\,\mathrm{mm}$ apart), and a static magnetic bias field $B_A = 180\,\mathrm{mT}$ is applied along the spin-wave propagation direction. In the absence of an applied current, the meander structure has negligible effect on spin-wave propagation through the waveguide and the DMC is "off". The spin-wave dispersion relationship $\omega(k)$ and transmission characteristic corresponding to this state are shown by the dotted blue

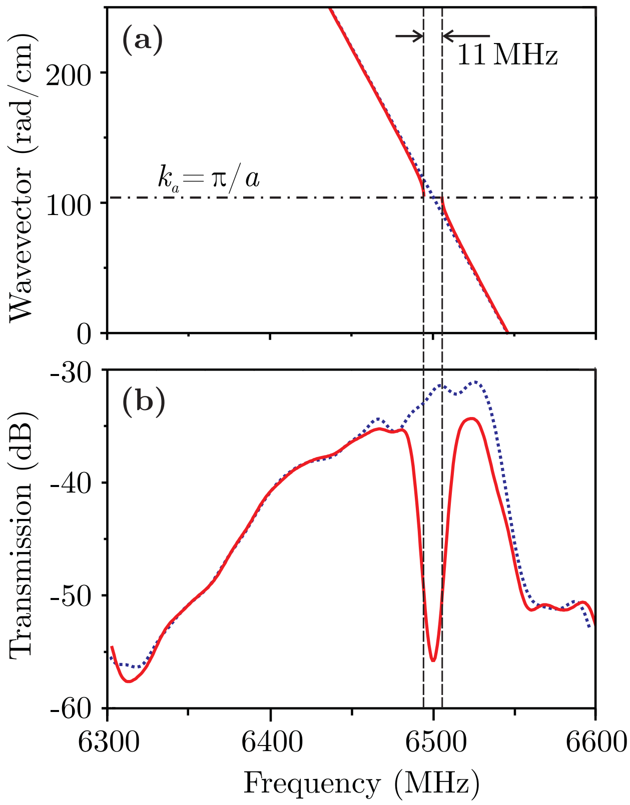

Figure 4.2: (a) Theoretical spin-wave dispersion relationship for the DMC system in the "off" (dotted, blue) and "on" (solid, red) states. These data assume a theoretical spin-wave group velocity of $v_g = 2.74 \times 10^4\,\mathrm{m\,s^{-1}}$ obtained using Eqn. (1.77). (b) Spin-wave transmission characteristics of the experimental system with the DMC in the "off" state (no current applied to the meander structure, dotted, blue) and in the "on" state (static current of 1 A in the meander structure, solid, red). In the latter case there is a band gap corresponding to the wavevector $k_a = \pi/a$ centred on $\omega_a = 2\pi \cdot 6500\,\mathrm{MHz}$. The $-3\,\mathrm{dB}$ width of the gap is around $2\pi \cdot 30\,\mathrm{MHz}$, its width at $-20\,\mathrm{dB}$ is approximately $2\pi \cdot 11\,\mathrm{MHz}$.

lines in Figs. 4.2(a) and 4.2(b). However, if a current $I_0(t)$ is applied to the meander structure, the resulting magnetic field (amplitude $\Delta B_\mathrm{A} \propto I_0$) spatially modulates the waveguide's magnetic bias. Under these conditions, the DMC is "on" and has a band gap corresponding to the wavevector $k_a = \pi/a \simeq 105\,\mathrm{rad\,cm^{-1}}$ which appears as a discontinuity in the spin-wave dispersion relationship centred on the resonance frequency $\omega(k_a) = \omega_a = 2\pi \cdot 6500\,\mathrm{MHz}$ (solid red line, Fig. 4.2(a)). The band-gap width is determined by ΔB_A ($\sim 1\,\mathrm{mT}$) and thus the amplitude of the current I_0.

Note that the SiO_2 spacer layer between the YIG and the meander structure is essential to the proper functioning of the crystal. The purpose of the spacer is to prevent direct inductive interaction between spin waves propagating in the waveguide and the metallic surface. If the meander structure is placed directly onto the YIG, such interaction is pronounced: the structure takes on the role of a receiver and secondary antenna and the system ceases to function as a magnonic crystal. Since the stray magnetic field[1] created by the spin waves in the YIG decays exponentially from its surface whilst the magnitude of the magnetic field created by a DC current in the meander structure falls off as the inverse of the distance from it, the thin spacer layer is an efficient means to remove the induction problem without unduly compromising the field modulation available to define the crystal.

4.3 Theoretical description of geometrically induced mode coupling in the DMC system

If a spin wave with wavevector $k_s \approx k_a = \pi/a$ is incident on the DMC whilst it is "on", it undergoes simple reflection, creating a valley in the experimental transmission curve (solid red line, Fig. 4.2(b)). However, if the crystal is *switched* from "off" to "on" whilst such a wave is *inside*, a coupling between the incident wave mode and

[1] That is, the magnetic field outside of the film.

secondary modes with wavevectors $k_r = k_s \pm 2k_a$ is brought about. This coupling is strong when the eigenfrequencies of the waves, $\omega_s = \omega(k_s)$ and $\omega_r = \omega(k_r)$, are close to each other, i.e. for $k_s \approx k_a$ and thus *counter-propagating* waves $k_r = k_s - 2k_a \approx -k_a$.

By analogy with a pair of interacting harmonic oscillators, the dynamics of the complex amplitudes c_s and c_r of the interacting incident and secondary modes can be modelled by a pair of coupled equations [136]

$$\frac{\mathrm{d}c_s}{\mathrm{d}t} = \mathrm{i}\omega_s c_s + \mathrm{i}\Omega_a c_r, \tag{4.3a}$$

$$\frac{\mathrm{d}c_r}{\mathrm{d}t} = \mathrm{i}\omega_r c_r + \mathrm{i}\Omega_a c_s. \tag{4.3b}$$

Or, in matrix form

$$\frac{\mathrm{d}\boldsymbol{c}}{\mathrm{d}t} = \mathbf{W}\boldsymbol{c} \tag{4.4}$$

with

$$\mathbf{W} = \mathrm{i}\begin{pmatrix} \omega_s & \Omega_a \\ \Omega_a & \omega_r \end{pmatrix} \qquad \boldsymbol{c} = \begin{pmatrix} c_s \\ c_r \end{pmatrix}$$

where Ω_a is a coupling constant numerically equal to the half-width of the crystal band gap. The eigenfrequencies of Eqn. (4.4) are the eigenvalues of the matrix $\mathbf{W}$:

$$\omega_{1,2} = \overline{\omega} \pm \sqrt{\Omega_a^2 + \delta\omega^2} = \overline{\omega} \pm \Omega \tag{4.5}$$

where $\overline{\omega} = (\omega_s + \omega_r)/2$ is the average frequency of the waves, and $\delta\omega = (\omega_s - \omega_r)/2$ is their frequency mismatch. Equation (4.5) describes the dispersion relation for a *static* magnonic crystal in the "on" state with a band gap of width $2\Omega_a$ centred on the resonance frequency $\omega_s = \omega_r = \omega_a$. In the case that the crystal is switched "on" whilst the spin wave is inside, at the moment of switching ($t = 0$), the amplitude of the incident wave takes a maximum value ($c_s = 1$), whilst the coupled secondary wave is absent ($c_r = 0$). Solving Eqns. (4.4) with these initial conditions enables us to determine how the power $P_{s,r} = |c_{s,r}|^2$ of each wave changes with time:

$$P_s(t) = \cos^2(\Omega t) + \frac{\delta\omega^2}{\Omega^2}\sin^2(\Omega t)\,, \tag{4.6a}$$

$$P_r(t) = \frac{\Omega_a^2}{\Omega^2}\sin^2(\Omega t). \tag{4.6b}$$

The equations above describe *periodic* energy exchange at frequency Ω between confined, geometrically-coupled incident (k_s) and secondary (k_r) modes. The maximum power fraction transferred to the k_r mode $R_{\max} = \Omega_a^2/\Omega^2 = \Omega_a^2/(\Omega_a^2 + \delta\omega^2)$ is of order unity for waves within the band gap ($|\delta\omega| < \Omega_a$) and is achieved after a characteristic energy exchange time

$$T = \frac{\pi}{2\Omega} = \frac{\pi}{2\sqrt{\Omega_a^2 + \delta\omega^2}}, \tag{4.7}$$

or odd integer multiplies thereof. If the dynamic crystal is switched "off" at $t = \tau$, eliminating the coupling, the modes, now independent and no longer confined to the crystal, propagate out of it in opposite directions at their respective frequencies ω_s and ω_r. Accordingly, since the energy originally entered the crystal at ω_s, the mechanism provides a means to bring about frequency conversion—energy transfer from an incident mode of frequency ω_s to a secondary mode of frequency ω_r—in a linear wave medium.

Since the process of frequency conversion is efficient only over a narrow range of wavevectors $k_s \approx k_a$, the dispersion relations for the incident and secondary waves can be closely approximated by first order Taylor expansions,

$$\omega_s = \omega(k_s) = \omega_a + v_{\mathrm{g}}(k_s - k_a), \tag{4.8a}$$

$$\omega_r = \omega(k_r) = \omega_a - v_{\mathrm{g}}(k_r + k_a), \tag{4.8b}$$

where $v_{\mathrm{g}} = \partial\omega(k)/\partial k$ is the group velocity at $k = k_a$ (Eqn. (1.77)). Given the relation between the coupled wavevectors $k_r = k_s - 2k_a$, and assuming a symmetric dispersion law $\omega(k) = \omega(-k)$, Eqns. (4.8) allow us to obtain an expression for the relationship between the frequencies of the coupled modes

$$\omega_r = 2\omega_a - \omega_s, \tag{4.9}$$

i.e. the incident and secondary mode frequencies are related by *inversion* of their detuning $|\delta\omega|$ from the resonance frequency ω_a.

The process of oscillatory energy exchange and frequency inversion is illustrated schematically in Fig. 4.3. The lines plotted on the axes of the top panel represent the spin-wave dispersion curve for incident (positive k, solid black line) and secondary waves (negative k, dotted blue line) for $|k| \sim |k_a|$. The solid black dots indicate the wavevectors $\pm k_a$ corresponding to the band-gap centre frequency ω_a. The black triangle identifies an incident mode, assumed to be inside the crystal at $t = 0$ when the DMC is switched "on". The open blue circle marks the corresponding secondary mode of wavevector $k_r = k_s - 2k_a$ to which this incident mode is coupled. In the lower panel, the heights of the peaks centred on k_s (black) and k_r (blue) represent the power in the incident and secondary modes. Almost complete energy exchange occurs every T seconds for as long as the DMC remains "on".

It is important to stress that other than defining the dynamic properties of the incident and secondary waves, the form of the spin-wave dispersion curve has no influence on the mode coupling phenomenon. It should be understood that the negative slope of the BVMSW dispersion curve—though unusual—is no more than a practical detail of our model wave system. The result we describe is applicable without modification to waves of any physical nature with any monotonic, symmetric (i.e. $\omega(k) = \omega(-k)$) dispersion relation.

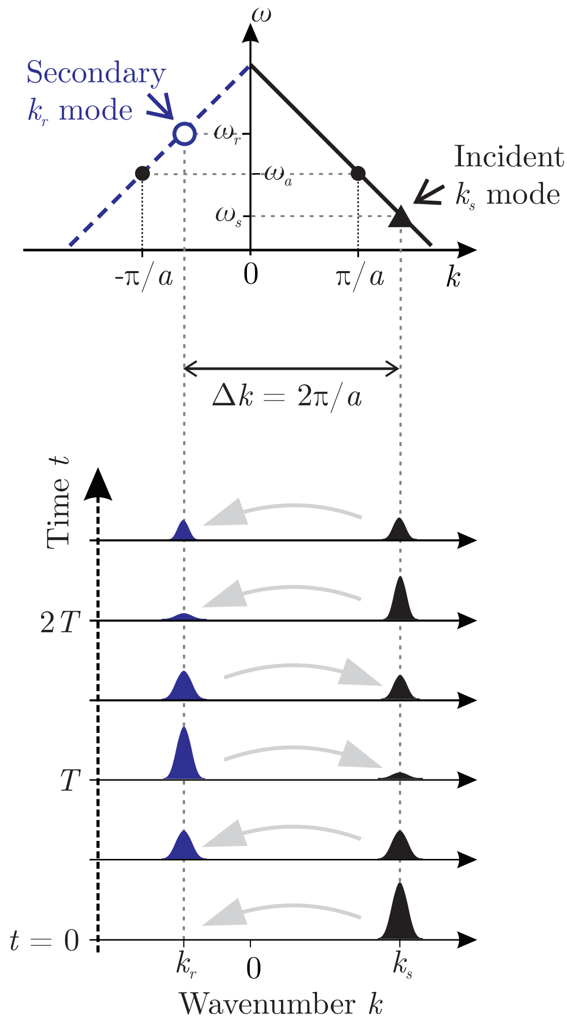

Figure 4.3: Inter-modal energy exchange in the DMC system. The diagonal lines in the upper panel represent the spin-wave dispersion curve. Solid dots (black) mark the wave-vectors $\pm k_a$ corresponding to the band-gap centre frequency ω_a. If the DMC is switched "on" at $t = 0$ whilst an incident mode $k_s \approx k_a$, frequency ω_s (black triangle) is inside, this mode is coupled to a secondary mode $k_r = k_s - 2k_a$, frequency ω_r (blue open circle). In the lower panel, the heights of the peaks centred on k_s (black) and k_r (blue) represent the power in the incident and secondary modes. Almost complete energy exchange occurs every T seconds for as long as the coupling persists.

4.4 Experimental investigation of spin-wave mode coupling in the DMC system

4.4.1 Experimental methods

Experimental investigations into the geometrical mode coupling mechanism were performed using an approximately rectangular current pulse $I_0(t)$ of duration τ (rise and fall times $\Delta\tau \approx 5\,\mathrm{ns}$) to briefly switch the DMC "on" whilst an incident spin-wave signal packet of centre frequency ω_s and duration T_d excited by a microwave drive signal (A_in, Fig. 4.1) was contained within it.[2] A schematic diagram of the full experimental setup is shown in Fig. 4.4.

When the DMC is switched "on" ($t = 0$), transfer of energy from the incident k_s mode into the secondary k_r mode initiates (Fig. 4.3), both of these modes being confined to the crystal. Following the deactivation of the coupling at $t = \tau$, the k_s mode propagates to the output spin-wave antenna, producing a transmitted signal of power $A_s \propto P_s(\tau)$, whilst the k_r mode travels to the input antenna, originating a reversed signal of power $A_r \propto P_r(\tau)$ (see Fig. 4.1).[3] The microwave power applied to the input antenna was maintained constant at $1\,\mathrm{mW}$, so that the spin-wave signal powers in all experiments were at least two orders of magnitude lower than those known to be required to observe the effects of non-linear terms in YIG's small-signal magnetic susceptibility. So as to minimize the influence of thermal effects on the data, experiments were conducted with a $500\,\mu\mathrm{s}$ repetition rate.

[2] So long as the spectral extent of the spin-wave packet is restricted to the band gap of the magnonic crystal in the "on" state, and its spatial extent allows it to be confined within the DMC structure, the results discussed are invariant with the packet duration.

[3] In the absence of damping and with perfect antenna efficiency we would have simply, $A_{s,r} = P_{s,r}(\tau)$.

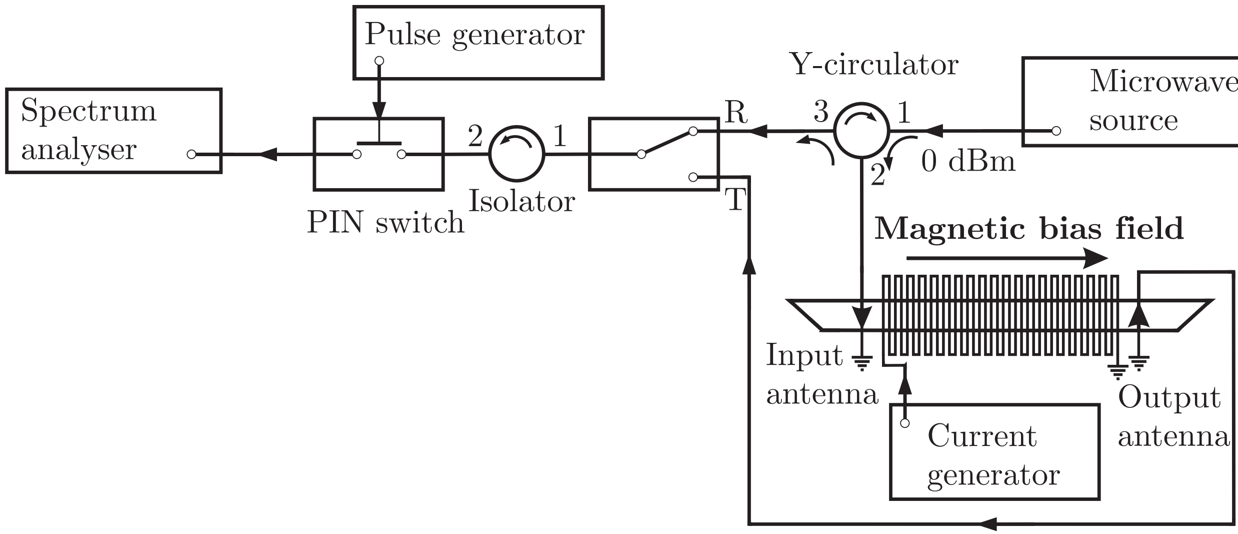

Figure 4.4: Schematic diagram of the experimental arrangement used for the investigation of frequency conversion and inter-modal energy exchange in the DMC system. Spin-wave packets of duration T_{d} were produced using an externally triggered microwave source (Agilent 8673B Synthesized Signal Generator) and applied by means of a broadband 3-port (1 = input, 2 = output, 3 = return) Y-circulator to the input antenna. After a delay sufficient to allow the packets to propagate to the centre of the DMC waveguide, a rectangular current pulse of duration τ was applied to the DMC meander structure from a current pulse generator (Agilent 8114A) through a matching network (not shown). A low-impedance manual switch was used to route either the transmitted (T) or reversed (R) signal from the output antenna to a spectrum analyser (Agilent E4446A, 3 Hz to 44 GHz). A PIN switch triggered by a pulse generator was used to gate the input to the spectrum analyser in such a way as to prevent the radiated electromagnetic signal from the input antenna reaching the instrument.

4.4.2 Observation of frequency conversion in the DMC system

Figure 4.5 shows measured frequencies of transmitted (k_s) and reversed (k_r) signals for input spin-wave signal packets of duration $T_\mathrm{d} = 200\,\mathrm{ns}$ (spectral width $\sim 2\pi \cdot 5\,\mathrm{MHz}$) at two values of the coupling duration τ. It can be seen that the frequency of the transmitted signal is unchanged by interaction with the crystal. The reversed signal frequency is, as anticipated by the theory outlined above, related to that of the incident signal by an inversion of its detuning $|\delta\omega|$ from the band-gap centre frequency ω_a and is independent of τ. The data are a near-perfect fit to the theory of Eqn. (4.9) providing strong evidence for its validity.

Further evidence of the frequency inversion phenomenon is presented in Fig. 4.6. The data plotted as open blue circles on Fig. 4.6(a) (left ordinate axis) show the measured reversed signal frequency ω_r as a function of the carrier frequency ω_s for a coupling duration $\tau = 25\,\mathrm{ns}$. The solid blue circles (right ordinate axis) indicate the corresponding reversed signal power demonstrating that, as predicted by Eqns. (4.6), the efficiency of the energy exchange process is maximum at $\omega_s = \omega_a = \omega_r$ and

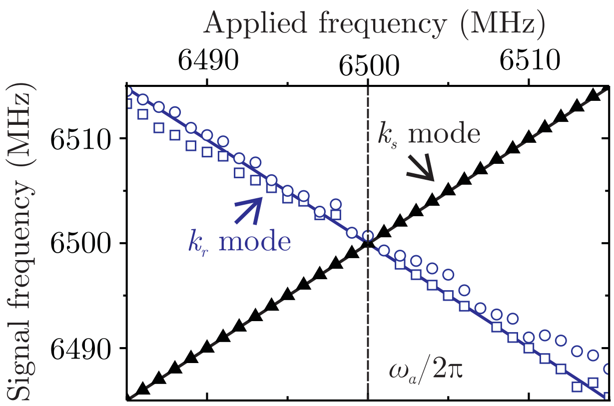

Figure 4.5: Reversed (k_r, blue open symbols) and transmitted (k_s, black triangles) signal frequencies as a function of applied signal carrier frequency. Reversed signal data are shown at $I_0 = 1\,\mathrm{A}$ for two values of coupling duration: $\tau = 25\,\mathrm{ns}$ (circles) and $\tau = 20\,\mathrm{ns}$ (squares). Transmitted signal datapoints for both values of τ are represented by a single triangular symbol. Solid lines show the theory of Eqn. (4.9).

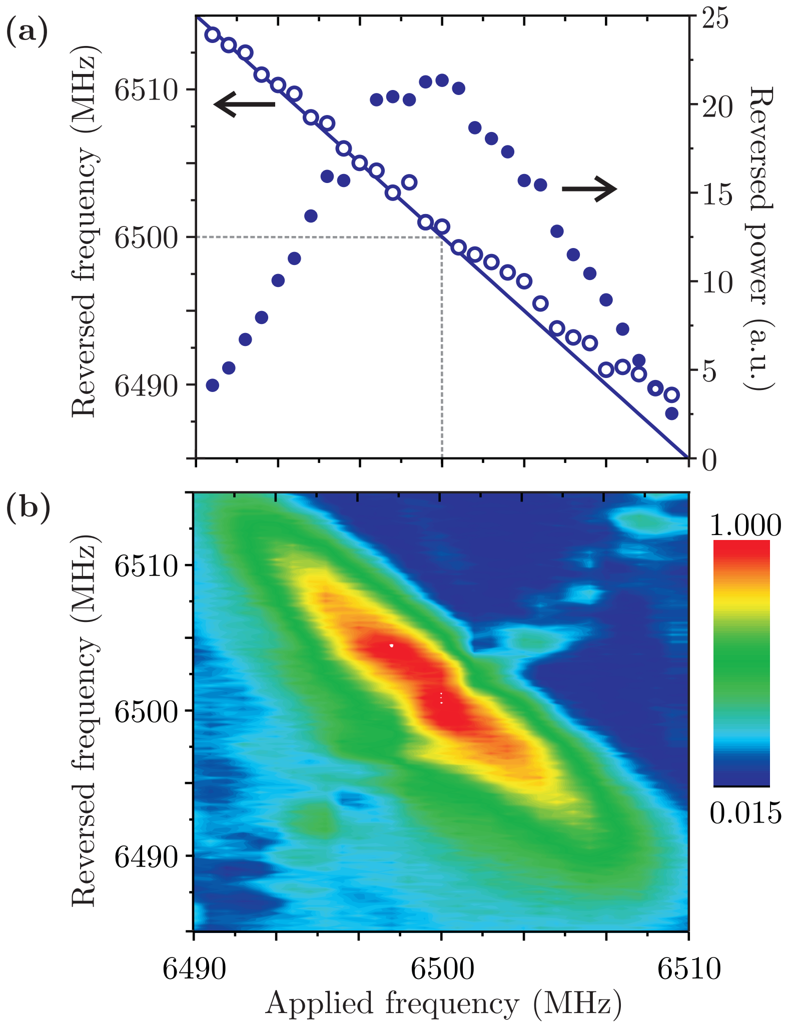

Figure 4.6: (a) When the carrier wavevector k_s of the incident spin-wave signal packet is detuned from the resonance value of $k_a = \pi/a$ which corresponds to a frequency $\omega_a = 2\pi \cdot 6500\,\mathrm{MHz}$, the detuning of the reversed signal (the secondary mode), is inverted about this value (left ordinate axis, open circular symbols, see also Fig. 4.5). The solid line is the theoretical curve of Eqn. (4.9). The efficiency of the energy exchange process is maximum at the resonance condition and decreases symmetrically with increasing $|\delta\omega|$. (b) Two-dimensional map of reversed signal spectra as a function of incident signal carrier frequency ω_s (31 spectra taken at 1 MHz intervals). Dark red indicates the highest signal intensities, dark blue the lowest, the intervening scale is linear. The diagonal stripe of high signal intensity running from the upper-left to the lower-right corner is clear evidence of frequency inversion. The weak, broken diagonal stripe which can be identified running from the bottom left to the top right is due to conventional reflection of the incident signal from the metallic meander structure and inhomogeneities in the spin-wave waveguide. The data of both (a) and (b) correspond to a coupling duration $\tau = 25\,\mathrm{ns}$.

decreases symmetrically with increasing $|\delta\omega|$. Figure 4.6(b) shows a two-dimensional map of the reversed signal spectra from which the data displayed in Fig. 4.6(a) were extracted.

4.4.3 Observation of oscillatory energy exchange in the DMC system

The oscillatory nature of the energy exchange process within the DMC system was confirmed by measuring, for a constant incident signal power and frequency $\omega_s = \omega_a$, the powers of both the reversed ($A_r \propto P_r(\tau)$) and transmitted ($A_s \propto P_s(\tau)$) signals as the coupling duration τ was varied and computing their ratio

$$\kappa(\tau) = \frac{P_r(\tau)}{P_s(\tau)} = \frac{\Omega_a^2 \tan^2(\Omega\tau)}{\Omega^2 + \delta\omega^2 \tan^2(\Omega\tau)}\,, \tag{4.10}$$

which—bar a constant factor—is independent of damping.

The antiphase temporal variation of the incident and secondary mode powers predicted by Eqns. (4.6), is confirmed by the experimental data of Fig. 4.7(a) for the resonance case $\omega_s = \omega_r = \omega_a$. The closed black triangular symbols and open blue circular symbols indicate the transmitted and reversed powers, P_s and P_r, as the coupling duration is varied. Note that the lines connecting the datapoints are purely to guide the eye.

Although there is convincing agreement between the trend of the data shown in Fig. 4.7(a) and that predicted by the simple model of Eqns. (4.6) several unmodelled features of the results warrant clarification. The reduction in the signal amplitudes with increasing τ occurs as a result of damping. Damping is also partly responsible for the small horizontal offset between the minima of the transmitted curve and the maxima of the reversed curve; the power of the reversed signal is described by a function of the form $P_r \sim \sin^2(\Omega\tau)\,\mathrm{e}^{-2\Gamma\tau}$, where Γ is a damping constant, it follows that for $\Gamma \neq 0$, the maxima are shifted to smaller τ. A second contribution to the apparent phase shift between the two curves comes from the weak reflection of spin waves from the meander structure and inhomogeneities in the waveguide. The presence of these spurious reflections (which have a power that is approximately invariant with τ and one order of magnitude smaller than that of the reversed signal) is also consistent with the non-zero minima observed in the reversed curve. A further mechanism for a vertical offset in reversed signal data arises from the finite spread of energy exchange times T (Eqn. (4.7)) over the spectral width of the input spin-wave signal.

Figure 4.7(b) shows the power ratio of the reversed and transmitted signals of

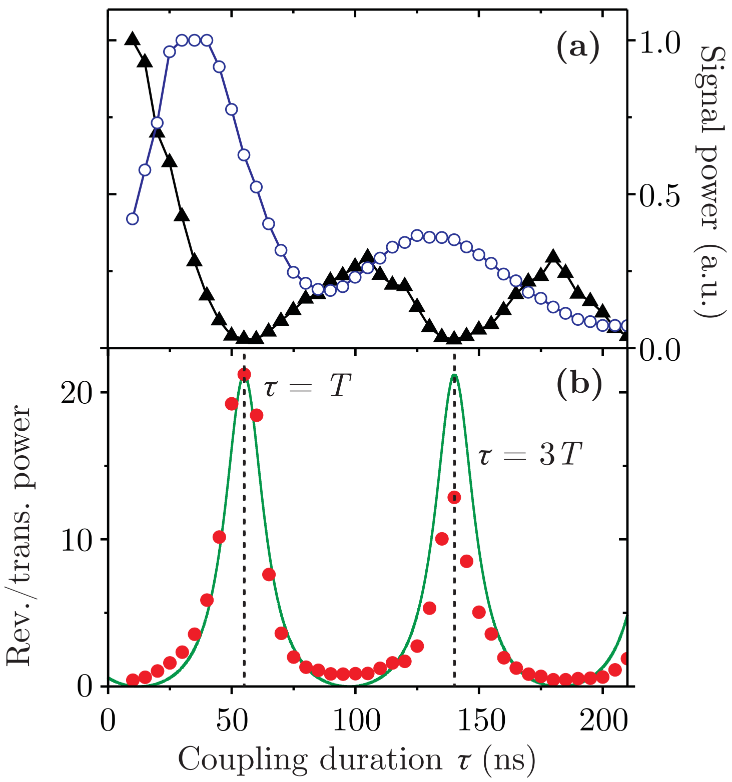

Figure 4.7: (a) Experimental reversed (P_r, open blue circles) and transmitted (P_s, black triangles) signal powers as a function of coupling duration τ for $\omega_s = \omega_r = \omega_a$. (b) Ratio of reversed to transmitted signal powers as a function of τ; circular symbols (red) are points corresponding to the experimental data of (a), the solid curve (green) is the theory of Eqn. (4.10).

Fig. 4.7(a) (red circular symbols) and the corresponding theory ($\kappa = P_r/P_s$, solid green line). As can be seen, there is good agreement between the two trends; the peaks correspond to coupling times τ equal to odd integer multiples of T (Eqn. (4.7)), troughs to even integer multiples. The theoretical curve in Fig. 4.7(b) is plotted using Eqn. (4.10). The fit is achieved by assuming a band-gap half-width $\Omega_a = 2\pi{\cdot}5.53\,\mathrm{MHz}$, a small detuning $\delta\omega = 0.03\,\%$, and an effective coupling duration $\tau_{\mathrm{eff}} = \tau - 2\Delta\tau$ where $2\Delta\tau = 12.5\,\mathrm{ns}$ to account for the effect of the finite rise and fall times of the DMC current pulse and the imperfect high-frequency matching of the DMC meander structure to the current source. The plot is also scaled to match the experimental and theoretical maximum ratios (absolute values being dependent on losses and antenna efficiencies). The difference in the heights of the two peaks in the experimental data of Fig. 4.7(b) occurs as a result of the finite duration of the input spin-wave signal. For a signal of finite spectral width, the true power of the reversed signal is the integration of Eqn. (4.6b) over all frequency components $\delta\omega$ of the input signal. Since these components have a range of different characteristic energy exchange times T (Eqn. (4.7)) the integral reduces with increasing τ.

Note that the value of the coupling constant $\Omega_a = 2\pi \cdot 5.53\,\mathrm{MHz}$ derived from fitting the theory of Eqn. (4.10) to the experimental data reflects the measured half-width of the static crystal band gap at approximately $-20\,\mathrm{dB}$ (Fig. 4.2). This is consistent with the fact that the coupling mechanism is only pronounced when the incident mode is strongly confined by the crystal.

4.4.4 Investigating the dependence of the secondary mode power on coupling duration in the DMC system

For a fixed incident mode power, Eqns. (4.6) predict that the frequency dependence of the secondary mode power varies with the coupling duration τ. In order to observe this dependence experimentally, an input spin-wave packet of duration 150 ns (spectral width $\sim 2\pi \cdot 6.67\,\mathrm{MHz}$) and carrier frequency $\omega_s = \omega_a = 2\pi \cdot 6500\,\mathrm{MHz}$ was employed. The power spectrum of the reversed signal (A_r, Fig. 4.1) was recovered for values of τ in the range 15–210 ns. The results of this experiment are plotted in Fig. 4.8(a). For comparison, Fig. 4.8(b) shows the corresponding theoretical calculation using the parameters obtained from the data of Fig. 4.7(b). As can be seen, the theory accurately predicts the key features of the data, namely the high signal intensity at $\omega_r = \omega_a$ which extends from the shortest measured coupling duration ($\tau = 15\,\mathrm{ns}$) to around $\tau = 90\,\mathrm{ns}$, and the branching of the spectra at approximately $\tau = 90\,\mathrm{ns}$ and $\tau = 180\,\mathrm{ns}$. The primary cause of the deviation between the experimental data shown in Fig. 4.8(a) and the theory of Fig. 4.8(b) at long coupling times τ is leakage of energy from the DMC during the coupling interval; an inevitable feature of any experiment using an artificial crystal of non-infinite length. The leakage starts to strongly influence the data when τ exceeds the time t_e taken for the waves to travel from the middle of the crystal to its edge (i.e. the time required for waves which were originally at the centre of the crystal to propagate out of it). A crude approximation for t_e, $t_\mathrm{e} \approx L_\mathrm{c}/2v_\mathrm{g}$ results in a figure of 110 ns which is consistent with the appearance of the data. Note however, that the evolution of the signals is, in reality, complicated by the fact that the severity of the leakage is frequency dependent since with the crystal "on", the group velocity of waves inside it depends on their frequency relative to the centre of the band gap.

Figures 4.8(c) and 4.8(d) are sections through the data of Fig. 4.8(a) (red circular symbols) and Fig. 4.8(b) (blue curves) at $\tau = 50\,\mathrm{ns}$ and $\tau = 105\,\mathrm{ns}$ respectively. The most likely explanation for the asymmetry in the experimental data of Fig. 4.8(d) is a slight discrepancy between the input signal centre frequency and the resonance frequency of the DMC and/or a weak wavevector dependence of the characteristics of the microstrip antennae.

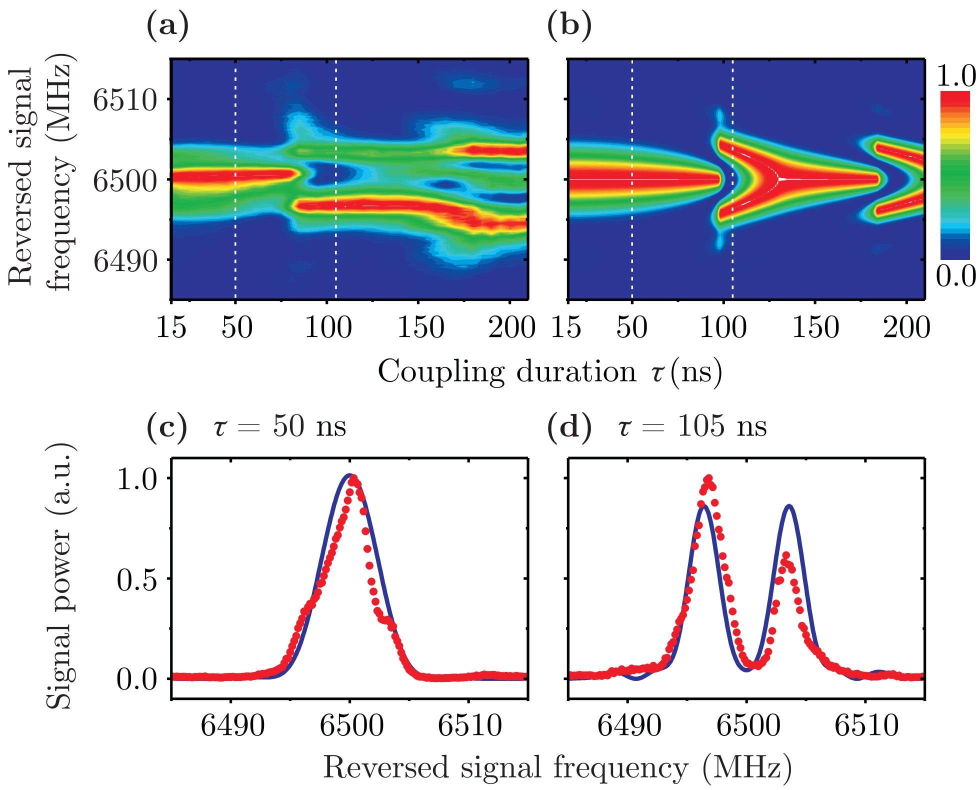

Figure 4.8: (a) Reversed ($A_r \propto P_r(\tau)$, Fig. 4.1) signal spectra as a function of the coupling duration τ for an input spin-wave signal of duration 150 ns, carrier frequency $\omega_s = \omega_a = 2\pi \cdot 6500$ MHz. Red is indicative of the highest signal intensities, dark blue the lowest, the intervening colour scale is linear. Each spectrum is individually normalized to its maximum value. (b) Theoretical calculation of the data of (a) using parameters obtained from the data of Fig. 4.7. Panels (c) and (d) show sections of the experimental data of (a) (red circular symbols) and (b) (blue curves) at $\tau = 50$ ns and $\tau = 105$ ns respectively (vertical dashed lines, (a) and (b)).

4.4.5 Visualizing interacting waves in the DMC system

To further clarify the features of the mode coupling mechanism, Fig. 4.9 shows theoretical spatio-temporal maps of the interacting waves in the artificial crystal system for different coupling durations τ. In each of the panels,[4] the power of the incident (k_s, red) and secondary (k_r, blue) modes is plotted as a function of time (vertical axes) and position (horizontal axes) and the dashed horizontal lines indicate the time interval τ. An ideal, lossless system with $\omega_s = \omega_r = \omega_a$ is assumed. The first two panels correspond to τ values equal to odd (a) and even (b) integer multiples of T. In the former case, when the coupling is deactivated all of the wave power resides in the secondary k_r mode which propagates back to the input antenna, in the latter, the converse is true. At intermediate values of τ, the energy is shared between the k_s and k_r modes. For the special case that τ is an odd integer multiple of $0.5T$, the

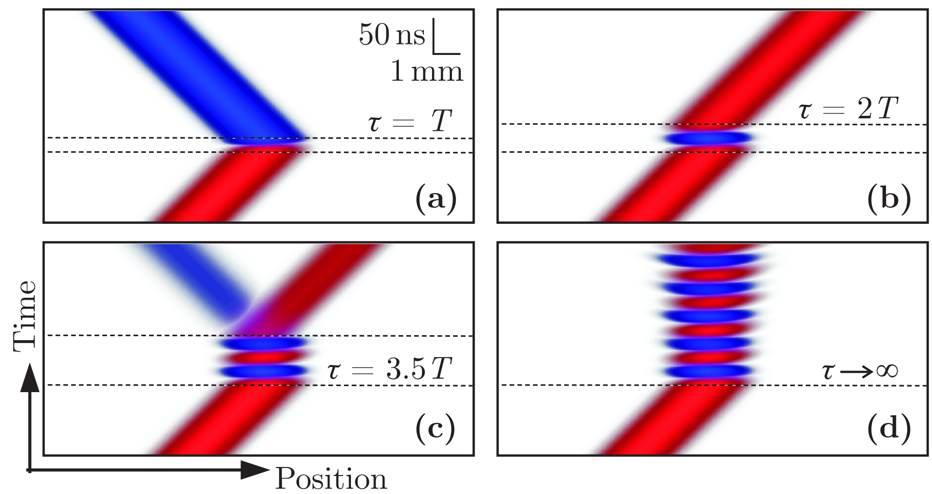

Figure 4.9: Theoretical spatio-temporal maps of interacting waves in DMC system for different coupling durations τ at $\omega_s = \omega_r = \omega_a$. Each panel shows the space- (horizontal) time (vertical) dependence of the wave power. Red and blue colours correspond to the incident (k_s) and secondary (k_r) waves respectively and the intensity of the colour represents the wave power. Dashed horizontal lines indicate the time interval τ during which the DMC is “on”. (a) $\tau = T$. (b) $\tau = 2T$. (c) $\tau = 3.5T$ (50:50 beamsplitter). (d) $\tau \to \infty$.

[4] Graphics with thanks to Dr. V. S. Tiberkevich.

wave energy is divided equally between the two counter-propagating waves and the system acts as a 50:50 beamsplitter (panel (c)). In the limit $\tau \to \infty$ the incident wave energy is effectively "stopped"; it remains confined to the crystal and repeatedly oscillates between the k_s and k_r modes (panel (d)).

4.5 Experimental investigation of time reversal in the DMC system

4.5.1 Experimental methods

The experimental investigations presented in §4.4 confirm both the oscillatory nature of the mode coupling phenomenon in the DMC system and its capacity to transfer energy from a forward propagating incident mode of frequency ω_s to a reverse propagating secondary mode with a frequency $\omega_r = 2\omega_a - \omega_s$ (Eqn. (4.9)). As discussed in §4.1.1, the reversal of the time profile of a propagating signal or wavepacket is equivalent to inversion of its spectrum about a reference frequency. Accordingly, the process of spectral inversion (see Fig. 4.10) of the input spin-wave signal packet about ω_a implies time reversal.

At first—given the results presented in the previous section—the issue of obtaining direct experimental evidence of time reversal might appear a trivial one. An obvious approach suggests itself: to apply a spin-wave signal with an asymmetric time profile to the DMC system, recover the waveform generated by the DMC induced coupling process, and confirm by visual inspection that the operation has taken place. However, in practice, such an approach is rendered infeasible by the fact that the per-unit-distance attenuation of the spin-wave signals in the YIG is significant (see §2.2.2). If a spin-wave signal packet undergoes time reversal in the DMC system, the total effective propagation distance corresponding to each point in its time profile decreases

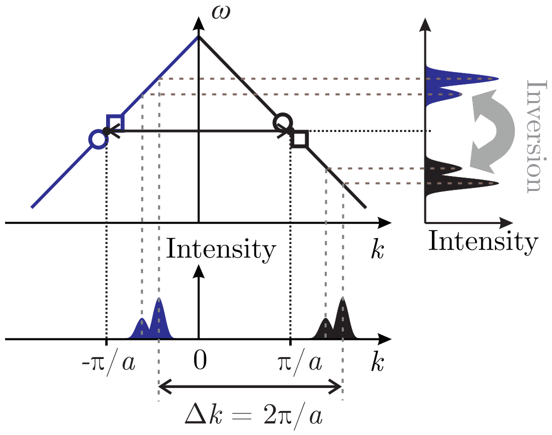

Figure 4.10: Schematic diagram illustrating the process of frequency inversion in the DMC system. The diagonal lines (blue and black) represent the spin-wave dispersion curve which is near-perfectly linear over the range of spin-wave frequencies of interest. Incident signal waves have positive wavevectors (black), whilst reversed waves have negative wavevectors (blue). The two groups of waves are counter-propagating. The small solid black dots indicate the resonance (band-gap centre) frequency ω_a which corresponds to the wavevectors $\pm k_a = \pm\pi/a$. The black open circle and square illustrate two spectral components of an incident signal waveform. The spatially periodic magnetic modulation of the waveguide's magnetic bias field brought about by the application of the current pulse to the DMC meander structure couples these components to corresponding components of a reversed waveform (blue open circle and square). The difference between the wavevectors of the incident and reversed waves is determined by the lattice constant of the DMC so that the spectrum of the reversed waveform is uniformly shifted to the left by $\Delta k = 2\pi/a = 2k_a$ (lower panel). This uniform shift in k-space results in spectral inversion (right panel). The resonance frequency ω_a provides the axis of inversion since at ω_a, $\omega_s = \omega_r = \omega_a$.

linearly with time from the leading edge.[5] As a result, unless the packet has a very narrow spatial extent, its time profile will undergo severe distortion. Since a narrow spatial extent implies a broad spectrum, this requirement is in conflict with the need to restrict the spectrum of the signal to the DMC band gap.

In our experiments, the difficulty presented by propagation losses was overcome by splitting the input signal into two independently controlled pulses; pulse A and pulse B. By comparing the reversed signals generated in three experiments: one with both pulse A and pulse B present, one with pulse A only present, and one with pulse B only present, it was possible to confirm the execution of time reversal. Figure 4.11 shows the experimental arrangement used for these investigations [62].

[5] That is, if the total spatial extent is z_{p}, the leading edge effectively travels a distance $2z_{\mathrm{p}}$ further than the trailing edge.

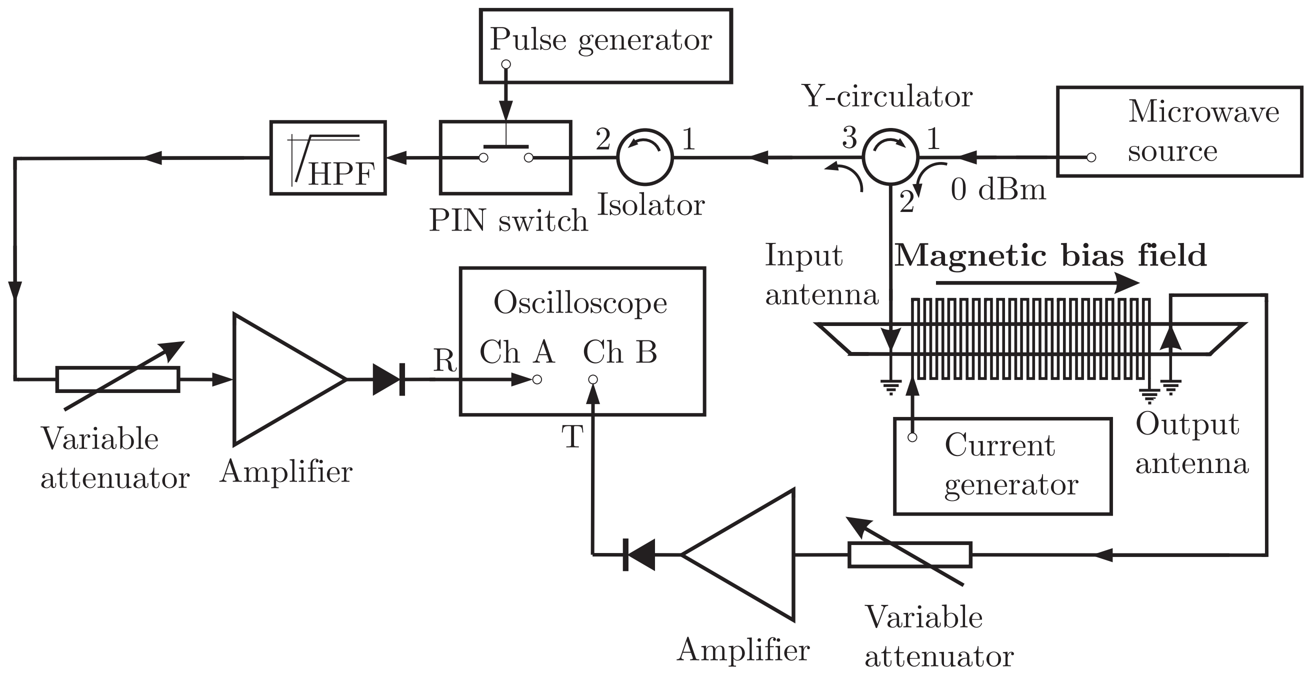

Figure 4.11: The experimental arrangement used for making the time-reversal measurements is similar to that employed in the frequency inversion investigations (Fig. 4.4). The train of spin-wave pulses was produced using an externally triggered microwave source (Agilent 8673B Synthesized Signal Generator) and applied by means of a broadband 3-port (1 = input, 2 = output, 3 = return) Y-circulator to the input antenna. After a delay sufficient to allow the pulse train to travel to the centre of the DMC system, a rectangular current pulse of duration 25 ns was applied to the DMC meander structure from a current pulse generator (Agilent 8114A) through a matching network (not shown). The spin-wave signal transmitted through the structure was routed to one channel of an oscilloscope (B) via a microwave amplifier coupled to a variable attenuator (to vary the gain) and a broadband detector diode. The reversed signal was connected to a second channel (A) of the oscilloscope via an amplification and rectification circuit comprising the same components as in the transmitted signal path plus a PIN switch to gate out the electromagnetic signal, and a high-pass filter (1–10 GHz) to remove low-frequency switching artefacts.

4.5.2 Experimental observation of time reversal in the DMC system

In our time-reversal experiments, the input spin-wave signal comprised two identical spin-wave pulses of carrier frequency $\omega_a = 2\pi \cdot 6500\,\mathrm{MHz}$. Experiments were undertaken with a range of pulse durations (T_d), spacings (T_s), and coupling times τ. The best results (judged on the basis of the appearance of the time-reversed signals) were obtained for $T_\mathrm{d} = 70\,\mathrm{ns}$, $T_\mathrm{s} = 40\,\mathrm{ns}$, and $\tau = 25\,\mathrm{ns}$.

Panel (a) of Fig. 4.12 shows—for reference—the time profiles of input (black) and transmitted (red) signals detected in the absence of DMC activation. If the first of the two input pulses, pulse A, is switched off, the first pulse in the transmitted signal, pulse T1 disappears. Similarly, the switching off of input pulse B leads to the disappearance of the second transmitted envelope, pulse T2.

The reversed signals displayed in blue in panel (b) of Fig. 4.12 were obtained by applying the microwave pulse train to the spin-wave input antenna and allowing it to propagate to the centre of the experimental system before switching the DMC "on" via the application of a current pulse of duration $\tau = 25\,\mathrm{ns}$ to the meander structure. When both spin-wave pulses are applied, two corresponding reversed pulses, pulse R1 and pulse R2, are observed (upper frame). Here however, unlike the transmitted signals, the switching off of the first input pulse, pulse A, results in the disappearance of the *second* reversed pulse, pulse R2. The corresponding situation, when pulse B is absent—the disappearance of the first reversed signal, pulse R1—is illustrated in the lower frame. This behaviour provides direct evidence of time reversal.

The relative intensity of the two reversed signals in Fig. 4.12(b) is consistent with the issue of propagation distance dependent attenuation discussed in §4.5.1: the second pulse, pulse R2, has a longer effective propagation distance in the YIG than pulse R1 and is therefore attenuated more significantly.

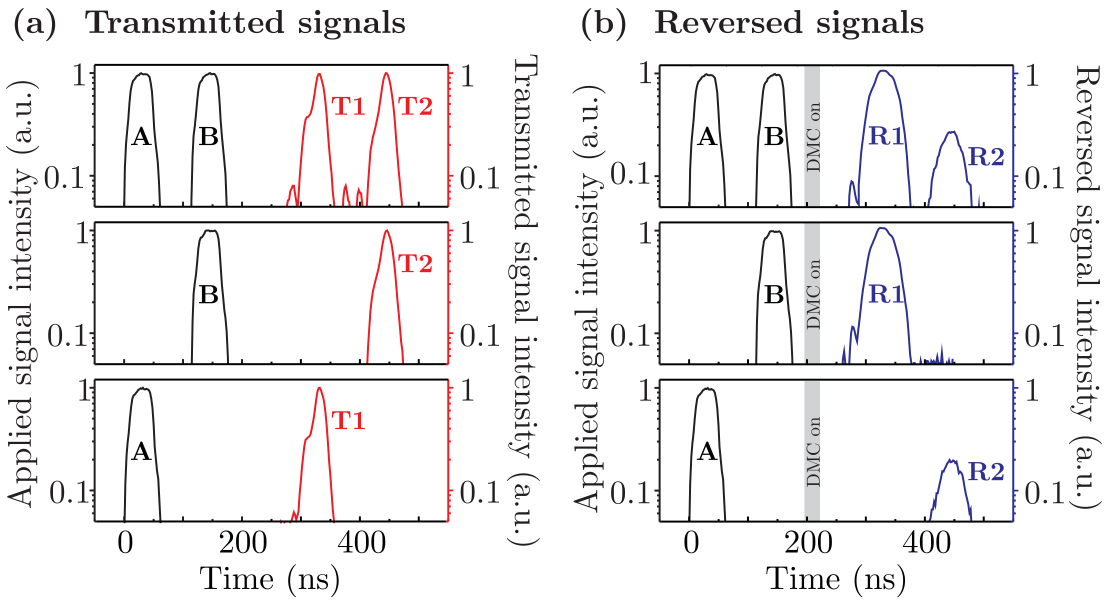

Figure 4.12: Experimental demonstration of time reversal in the dynamic magnonic crystal system was achieved using a train of two spin-wave pulses of carrier frequency $\omega_a = 2\pi \cdot 6500$ MHz, width 70 ns, and spacing 40 ns. The applied signals, which are shown in black in panels (a) and (b), are the envelopes of those supplied by the microwave generator. With no current applied to the DMC meander structure, the transmitted spin-wave signals (red, panel (a), upper frame) appear after a delay of ~ 300 ns. When the first of the two input pulses (pulse A) is switched off, the first transmitted pulse (pulse T1) is absent (middle frame). When the second input pulse (pulse B) is absent, the second transmitted pulse (pulse T2) disappears. The reversed spin-wave signals obtained after briefly switching the magnonic crystal "on" are shown in blue in panel (b). The shaded area indicates the time interval corresponding to the "on" state of the DMC. In the case that two spin-wave pulses are applied, two corresponding reversed pulses (R1 and R2) are observed (upper frame). However unlike the transmitted signals, when the first of the two pulses (pulse A) is absent it is the second reversed pulse, (pulse R2) which is found to disappear and vice versa, confirming time reversal.

4.6 Concluding remarks

In summary, the experimental work presented in this chapter has established the existence of a mode coupling mechanism in a dynamic artificial crystal and shown that this mechanism provides a means to perform the spectral transformation and time reversal of propagating signals and wavepackets. The mechanism, which is a principle of application to waves of any nature, is characterized by oscillatory energy exchange between counter-propagating wave modes coupled by the artificial crystal lattice. Data obtained using our experimental dynamic magnonic crystal have been shown to support a theoretical description of the coupling mechanism which models the coupled waves as interacting harmonic oscillators. The relationship between the frequencies of the coupled modes is determined by the crystal geometry, and the rate of energy exchange between them is controlled by the width of the crystal band gap and their frequency mismatch.

The work provides confirmation that non-stationary artificial crystal systems provide a means to realize complex spectral transformations such as time reversal which until now have only been demonstrated through the exploitation of non-linear wave media. As well as representing an interesting development in the understanding of general wave dynamics in metamaterial systems, the effect potentially finds widespread technological application. In the particular context of spin-wave dynamics, our experimental results directly demonstrate that dynamically controlled magnonic crystal systems open doors to sophisticated spin-information processing functionality which might be exploited in future magnonic and spintronic devices [62, 137].

The work might also be viewed as an intriguing hint that further investigation of dynamic media in which waves can be manipulated on timescales which are short in comparison with their characteristic propagation times—an as yet largely unexplored area of research—may lead to further interesting and potentially technologically relevant new insights into general wave dynamics.

Chapter 5

Concluding comments

Over the course of the last four chapters, we have progressed from a general description of magnetostatic spin waves through to a discussion, in chapters 3 and 4, of the findings of two very particular experimental investigations into their dynamic properties.

It is hoped that we have been successful in relating both the detail of the specific results we have obtained, and their wider scientific context. In this concluding section, we briefly comment on the work as a whole.

In chapter 3, we explored a marriage of concepts: the spin-wave active ring and the magnonic crystal. We described an experimental active ring incorporating a magnonic crystal and demonstrated that a signal enhancement mechanism reliant on the wavenumber dependent reflectivity of the crystal structure could be used to force it to excite preferentially at a mode having a single well-defined wavenumber. The wavenumber selective signal enhancement mechanism we observed potentially finds application in magnonic and spintronic devices, and, more generally, the outcomes of the work suggest that magnonic crystal based active rings may be a worthwhile new direction in experimental spin-wave studies.

In chapter 4, we explored a mechanism of oscillatory energy exchange between wave modes coupled by a dynamic artificial crystal. This mechanism was investigated experimentally using a dynamic magnonic crystal and it was demonstrated that it provides a means to realize the spectral transformation and time reversal of propagating signals and wavepackets. As well as representing a specific development in the field of spin-wave dynamics, this work has a more general significance as experimental confirmation that non-stationary artificial crystal systems open doors to the realization of complex spectral transformations such as time reversal in linear wave transmission media.

The starring role in both of our experimental investigations was played by the magnonic crystal.

Though the field of magnonic crystals is young, it is rapidly gaining recognition as one with much to contribute to our understanding not only of spin-wave dynamics, but of *general* wave dynamics in artificial crystal and metamaterial systems. As discussed in chapter 2, at present, the development of magnonic crystals is predominantly a one-dimensional science. The inherent complexities of directionally dependent spin-wave dispersion mean that the theoretical modelling of two- and three- dimensional structures is challenging, and their experimental realization even more so. However, with this challenge comes the promise of a new physical toybox: systems which offer original insight into fundamental magnetics, potential application in spintronic devices, and a unique and enlightening perspective on the physics of wave propagation.

The magnonic crystal embodies a superb example of what both the *spin* and the *wave* of spin wave have to offer us. It is with more than a little excitement that we look to its future.

Bibliography

[1] See for example the cluster issue on magnonics, J. Phys. D: Appl. Phys., **43**, (2010).

[2] Y. Kajiwara, K. Harii, S. Takahashi, J. Ohe, K. Uchida, M. Mizuguchi, H. Umezawa, H. Kawai, K. Ando, K. Takanashi, S. Maekawa and E. Saitoh, Transmission of electrical signals by spin-wave interconversion in a magnetic insulator, Nature, **464** 262, (2010).

[3] For a general introduction to spintronics see for example, S. A. Wolf, D. D. Awschalom, R. A. Buhrman, J. M. Daughton, S. von Molnár, M. L. Roukes, A. Y. Chtchelkanova and D. M. Treger, Spintronics: a spin-based electronics vision for the future, Science, **294** 1488, (2001).

[4] M. Ziese and Martin J. Thornton (Eds.), *Spin Electronics* (Springer, Berlin, 2001).

[5] J. F. Gregg, Spintronics: a growing science, Nature Mater., **6** 798, (2007).

[6] A. Fert, Nobel Lecture: origin, development, and future of spintronics, Rev. Mod. Phys., **80** 1517, (2008).

[7] P. A. Grünberg, Nobel Lecture: from spin waves to giant magnetoresistance, Rev. Mod. Phys., **80** 1531, (2008).

[8] A. Schmehl et al., Epitaxial integration of the highly spin-polarized ferromagnetic semiconductor EuO with silicon and GaN, Nature Mater., **6** 882, (2007).

[9] A. A. Serga, A. V. Chumak and B. Hillebrands, YIG magnonics, J. Phys. D: Appl. Phys., **43** 264002, (2010).

[10] A. D. Karenowska, J. F. Gregg, A. V. Chumak, A. A. Serga and B. Hillebrands, Spin information transfer and transport in hybrid spinmechatronic structures, J. Phys.: Conf. Ser., **303** 012018, (2011).

[11] P. G. de Gennes, P. A. Pincus, F. Hartmann-Boutron and J. M. Winter, Nuclear magnetic resonance modes in magnetic material I: Theory, Phys. Rev., **129** 1105, (1963).

[12] R. Coldea, D. A. Tennant, E. M. Wheeler, E. Wawrzynska, D. Prabhakaran, M. Telling, K. Habicht, P. Smeibidl and K. Kiefer, Quantum criticality in an ising chain: experimental evidence for emergent E8 symmetry, Science, **8** 5962, (2010).

[13] S. Blundell, *Magnetism in Condensed Matter* (Oxford University Press, Oxford, 2001).

[14] J. Stör and H. C. Siegmann, *Magnetism, from Fundamentals to Nanoscale Dynamics* (Springer-Verlag, Berlin, 2006).

[15] L. Néel, Anisotropie magnétique superficielle et surstructures d'orientation, J. Phys. Radium, **15** 225, (1954).

[16] D. D. Stancil, *Theory of Magnetostatic Waves* (Springer-Verlag, New York, 1993).

[17] D. Polder, On the theory of ferromagnetic resonance, Phil. Mag. (Series 7), **40** 99, (1949).

[18] B. Hillebrands and K. Ounadjela (Eds.), *Spin dynamics in confined magnetic structures I*, Topics Appl. Phys. **83** (Springer, Berlin, 2002), p 35–64.

[19] R. W. Damon and J. R. Eshbach, Magnetostatic modes of a ferromagnet slab, J. Phys. Chem. Solids, **19** 308, (1961).

[20] J. R. Eshbach and R. W. Damon, Surface magnetostatic modes and surface spin waves, Phys. Rev., **118** 1208, (1960).

[21] B. A. Kalinikos, Excitation of propagating spin waves in ferromagnetic films, Microw. Opt. Antennas, IEE Proc. H, **127** 1, (1980).

[22] J. H. E. Griffiths, Anomalous high-frequency resistance of ferromagnetic metals, Nature, **158** 610, (1946).

[23] L. F. Yin, D. H. Wei, N. Lei, L. H. Zhou, C. S. Tian, G. S. Dong, X. F. Jin, L. P. Guo, Q. J. Jia and R. Q. Wu, Magnetocrystalline anisotropy in Permalloy revisited, Phys. Rev. Lett., **97** 067203, (2006).

[24] J. Miguel, J. Sánchez-Barriga, D. Bayer, J. Kurde, B. Heitkamp, M. Piantek, F. Kronast, M. Aeschlimann, H. A. Dürr and W. Kuch, Time-resolved magnetization dynamics of cross-tie domain walls in permalloy microstructures, J. Phys.: Condens. Matter, **21** 496001, (2009).

[25] M. Kläui, Head-to-head domain walls in magnetic nanostructures, J. Phys.: Condens. Matter, **20** 313001, (2008).

[26] M. Hayashi, L. Thomas, C. Rettner, R. Moriya and S. S. P. Parkin, Direct observation of the coherent precession of magnetic domain walls propagating along permalloy nanowires, Nature Physics, **3** 21, (2007).

[27] M. Hayashi, L. Thomas, Ya. B. Bazaliy, C. Rettner, R. Moriya, X. Jiang and S. S. P. Parkin, Influence of current on field-driven domain wall motion in Permalloy nanowires from time resolved measurements of anisotropic magnetoresistance, Phys. Rev. Lett., **96** 197207, (2006).

[28] G. S. D. Beach, C. Nistor, C. Knutson, M. Tsoi and J. L. Erskine, Dynamics of field-driven domain-wall propagation in ferromagnetic nanowires, Nature Mater., **4** 741, (2005).

[29] L. Thomas, R. Moriya, C. Rettner and S. S.P. Parkin, Dynamics of magnetic domain walls under their own inertia, Science, **24** 1810, (2010).

[30] S. S. P. Parkin, M. Hayashi and Luc Thomas, Magnetic domain-wall racetrack memory, Science, **320** 190, (2008).

[31] M. Hayashi, L. Thomas, R. Moriya, C. Rettner and S. S. P. Parkin, Current-controlled magnetic domain-wall nanowire shift register, Science, **320** 209, (2008).

[32] V. E. Demidov, S. Urazhdin, V. Tiberkevich, A. Slavin and S. O. Demokritov, Control of spin-wave emission from spin-torque nano-oscillators by microwave pumping, Phys. Rev. B, **83** 060406(R), (2011).

[33] I. N. Krivorotov, N. C. Emley, J. C. Sankey, S. I. Kiselev, D. C. Ralph and R. A. Buhrman, Time-domain measurements of nanomagnet dynamics driven by spin-transfer torques, Science, **307** 228, (2005).

[34] S. Trudel, O. Gaier, J. Hamrle and B. Hillebrands, Magnetic anisotropy, exchange and damping in cobalt-based full-Heusler compounds: an experimental review, J. Phys. D: Appl. Phys., **43** 193001, (2010).

[35] F. Heusler, Über die Synthese ferromagnetischer Manganlegierungen, Verhandlungen der Deutschen Physikalischen Gesellschaft, **5** 217, (1903).

[36] R. A. de Groot, F. M. Mueller, P. G. van Engen and K. H. J. Buschow, New class of materials: Half-metallic ferromagnets, Phys. Rev. Lett., **50** 2024, (1983).

[37] R. Shan, H. Sukegawa, W. H. Wang, M. Kodzuka, T. Furubayashi, T. Ohkubo, S. Mitani, K. Inomata and K. Hono, Demonstration of half-metallicity in Fermi-level-tuned Heusler alloy $Co_2FeAl_{0.5}Si_{0.5}$ at room temperature, Phys. Rev. Lett., **102** 246601, (2009).

[38] Y. Sakuraba, M. Hattori, M. Oogane, Y. Ando, H. Kato, A. Sakuma, T. Miyazaki and H. Kubota, Giant tunneling magnetoresistance in Co_2MnSi/Al–O/Co_2MnSi magnetic tunnel junctions, Appl. Phys. Lett., **88** 192508, (2006).

[39] T. Kubota, S. Tsunegi, M. Oogane, S. Mizukami, T. Miyazaki, H. Naganuma and Y. Ando, Half-metallicity and Gilbert damping constant in $Co_2Fe_xMn_{1-x}Si$ Heusler alloys depending on the film composition, Appl. Phys. Lett., **94** 122504, (2009).

[40] M. Oogane R. Yilgin, M. Shinano, S. Yakata, Y. Sakuraba, Y. Ando and T. Miyazaki, Magnetic damping constant of Co_2FeSi Heusler alloy thin film, J. Appl. Phys., **101** 09J501, (2007).

[41] R. Yilgin, M. Oogane, Y. Ando and T. Miyazaki, Gilbert damping constant in polycrystalline Co_2MnSi Heusler alloy films, J. Magn. Magn. Mater., **310** 2332, (2007).

[42] M. Oogane, T. Wakitani, S. Yakata, R. Yilgin, Y. Ando, A. Sakuma and T. Miyazaki, Magnetic damping in ferromagnetic thin films, Jpn. J. Appl. Phys., **45** 3889, (2006).

[43] R. Yilgin, M. Oogane, S. Yakata, Y. Ando and T. Miyazaki, Intrinsic Gilbert damping constant in Co_2MnAl Heusler alloy films, IEEE Trans. Mag., **41** 2799, (2005).

[44] S. Mizukami, D. Watanabe, M. Oogane, Y. Ando, Y. Miura, M. Shirai and T. Miyazaki, Low damping constant for Co_2FeAl Heusler alloy films and its correlation with density of states, J. Appl. Phys., **105** 07D306, (2009).

[45] V. Cherepanov, I. Kolokolov and V. L'vov, The saga of YIG: Spectra, thermodynamics, interaction and relaxation of magnons in a complex magnet, Phys. Rep., **229** 81, (1993).

[46] E. E. Anderson, Molecular field model and the magnetization of YIG, Phys. Rev., **134** A1581, (1964).

[47] I. H. Solt Jr., Temperature dependence of YIG magnetization, J. Appl. Phys., Suppl. to **33** 1189, (1962).

[48] T. Schneider, A. A. Serga, T. Neumann, B. Hillebrands and M. P. Kostylev, Phase reciprocity of spin-wave excitation by a microstrip antenna, Phys. Rev. B, **77** 214411, (2008).

[49] F. Bloch, Zur Theorie des Ferromagnetismus, ZS. f. Phys., 206, (1930).

[50] C. Kittel, Interpretation of anomalous Larmor frequencies in ferromagnetic resonance experiment, Phys. Rev., **71** 270, (1947).

[51] See for example, W. S. Ishak, Magnetostatic wave technology: a review, Proc. IEEE, **76** 171, (1988).

[52] B. Hillebrands and K. Ounadjela (Eds.), *Spin dynamics in confined magnetic structures I*, Topics Appl. Phys. **83** (Springer, Berlin, 2002), p 65–92.

[53] T. Neumann, T. Schneider, A.A. Serga and B. Hillebrands, An electro-optic modulator-assisted wave vector-resolving Brillouin light scattering setup, Rev. Sci. Instrum., **80** 053905, (2009).

[54] F. Fohr, A.A. Serga, T. Schneider, J. Hamrle and B. Hillebrands, Phase sensitive Brillouin scattering measurements with a novel magneto-optic modulator, Rev. Sci. Instrum., **80** 043903, (2009).

[55] H. Schultheiss, S. Schäfer, P. Candeloro, B. Leven, B. Hillebrands and A. N. Slavin, Observation of coherence and partial decoherence of quantized spin waves in nano-scaled magnetic ring structures, Phys. Rev. Lett., **100** 047204, (2008).

[56] K. Perzlmaier, M. Buess, C. H. Back, V. E. Demidov, B. Hillebrands and S. O. Demokritov, Spin-wave eigenmodes of permalloy squares with closure domain structure, Phys. Rev. Lett., **94** 057202, (2005).

[57] C. Mathieu, J. Jorzick, A. Frank, S. O. Demokritov, B. Hillebrands, A. N. Slavin, B. Bartenlian, C. Chappert, D. Decanini, F. Rousseaux and E. Cambril, Lateral quantization of spin waves in micron size magnetic wires, Phys. Rev. Lett., **81** 3968, (1998).

[58] T. Schneider, A. A. Serga, A. V. Chumak, C. V. Sandweg, S. Trudel, S. Wolff, M. P. Kostylev, V. S. Tiberkevich, A. N. Slavin and B. Hillebrands, Nondiffractive subwavelength wave beams in a medium with externally controlled anisotropy, Phys. Rev. Lett., **104** 197203, (2010).

[59] S. O. Demokritov, A. A. Serga, A. André, V. E. Demidov, M. P. Kostylev and B. Hillebrands, Tunneling of dipolar spin waves through a region of inhomogeneous magnetic field, Phys. Rev. Lett., **93** 047201, (2004).

[60] A. A. Serga, T. Neumann, A. V. Chumak and B. Hillebrands, Generation of spin-wave pulse trains by current-controlled magnetic mirrors, Appl. Phys. Lett., **94** 112501, (2009).

[61] A. V. Chumak, T. Neumann, A. A. Serga, B. Hillebrands and M. P. Kostylev, A current-controlled, dynamic magnonic crystal, J. Phys. D: Appl. Phys., **42** 205005, (2009).

[62] A. V. Chumak, V. S. Tiberkevich, A. D. Karenowska, A. A. Serga, J. F. Gregg, A. N. Slavin and B. Hillebrands, All-linear time reversal by a dynamic magnonic crystal, Nature Commun., **1** 141, (2010).

[63] M. P. Kostylev, A. A. Serga, T. Schneider, B. Leven and B. Hillebrands, Spin-wave logical gates, Appl. Phys. Lett., **87** 153501, (2005).

[64] T. Schneider, A. A. Serga, B. Leven, B. Hillebrands, R. L. Stamps and M. P. Kostylev, Realization of spin-wave logic gates, Appl. Phys. Lett., **92** 022505, (2008).

[65] R. Hertel, W. Wulfhekel and J. Kirschner, Domain-wall induced phase shifts in spin waves, Phys. Rev. Lett., **93** 257202, (2004).

[66] L. Berger, Emission of spin waves by a magnetic multilayer traversed by a current, Phys. Rev. B, **54** 9353, (1996).

[67] C. W. Sandweg, Y. Kajiwara, K. Ando, E. Saitoh and B. Hillebrands, Enhancement of the spin pumping efficiency by spin wave mode selection, Appl. Phys. Lett., **97** 252504, (2010).

[68] S. O. Valenzuela and M. Tinkham, Direct electronic measurement of the spin Hall effect, Nature, **442** 176, (2006).

[69] E. Saitoh, M. Ueda, H. Miyajima and G. Tatara, Conversion of spin current into charge current at room temperature: Inverse spin-Hall effect, Appl. Phys. Lett., **88** 182509, (2006).

[70] J. E. Hirsch, Spin Hall effect, Phys. Rev. Lett., **83** 1834, (1999).

[71] M. I. Dyakonov and V. I. Perel, Current-induced spin orientation of electrons in semiconductors, Phys. Lett. A, **35** 459, (1971).

[72] M. I. Dyakonov and V. I. Perel, Possibility of orienting electron spins with current, JETP Lett., **13** 467, (1971).

[73] M. Blencowe, Quantum RAM, Nature, **468** 44, (2010).

[74] T. Duty, Towards superconductor-spin ensemble hybrid quantum systems, Physics, **3** 80, (2010).

[75] D. I. Schuster et al., High-cooperativity coupling of electron-spin ensembles to superconducting cavities, Phys. Rev. Lett., **105** 140501, (2010).

[76] H. Wu et al., Storage of multiple coherent microwave excitations in an electron spin ensemble, Phys. Rev. Lett., **105** 140503, (2010).

[77] J. H. Wesenberg, A. Ardavan, G. A. D. Briggs, J. J. L. Morton, R. J. Schoelkopf, D. I. Schuster and K. Mølmer, Quantum computing with an electron spin ensemble, Phys. Rev. Lett., **103** 070502, (2009).

[78] D. I. Schuster, *Circuit Quantum Electrodynamics* (Thesis, Yale University, 2007).

[79] B. A. Kalinikos, N. G. Kovshikov and C. E. Patton, Self-generation of microwave magnetic envelope soliton trains in Yttrium Iron Garnet thin fims, Phys. Rev. Lett., **80** 4301, (1998).

[80] A. A. Serga, S. O. Demokritov, B. Hillebrands and A. N. Slavin, Self-generation of two-dimensional spin-wave bullets, Phys. Rev. Lett., **92** 117203, (2004).

[81] M. Wu, B. A. Kalinikos, L. D. Carr and C. E. Patton, Observation of spin-wave soliton fractals in magnetic film active feedback rings, Phys. Rev. Lett., **96** 187202, (2006).

[82] M. Wu, A. M. Hagerstrom, A. Kondrashov and B. Kalinikos, Excitation of chaotic spin waves through modulational instability, Phys. Rev. Lett., **102** 237203, (2009).

[83] A. M. Hagerstrom, W. Tong, M. Wu, B. A. Kalinikos and R. Eykholt, Excitation of chaotic spin waves in magnetic film feedback rings through three-wave nonlinear interactions, Phys. Rev. Lett., **102** 207202, (2009).

[84] A. A. Serga, A. V. Chumak, A. André, G. A. Melkov, A. N. Slavin, S. O. Demokritov and B. Hillebrands, Parametrically stimulated recovery of a microwave signal stored in standing spin-wave modes of a magnetic film, Phys. Rev. Lett., **99** 227202, (2007).

[85] G. A. Melkov, A. A. Serga, V. S. Tiberkevich, Yu. V. Kobljanskij and A. N. Slavin, Nonadiabatic interaction of a propagating wave packet with localized parametric pumping, Phys. Rev. E., **63** 066607, (2001).

[86] G. A. Melkov, A. A. Serga, V. S. Tiberkevich, A. N. Oliynyk and A. N. Slavin, Wave front reversal of a dipolar spin wave pulse in a nonstationary three-wave parametric interaction, Phys. Rev. Lett., **84** 3438, (2000).

[87] See for example the classic paper, W. L. Bragg, The diffraction of short electromagnetic waves by a crystal, Proc. Camb. Phil. Soc., **17** 43, (1913).

[88] For a general introduction to photonic crystals see for example, J. D. Joannopoulos, P. R. Villeneuve and S. Fan, Photonic crystals: putting a new twist on light, Nature, **386** 143, (1997).

[89] S.-Y. Lin, E. Chow, V. Hietala, P. R. Villeneuve and J. D. Joannopoulos, Experimental demonstration of guiding and bending of electromagnetic waves in a photonic crystal, Science, **282** 274, (1998).

[90] S. John, Strong localization of photons in certain disordered dielectric superlattices, Phys. Rev. Lett., **58** 2486, (1987).

[91] E. Yablonovitch, Inhibited spontaneous emission in solid-state physics and electronics, Phys. Rev. Lett., **58** 2059, (1987).

[92] C. Croënne, E. D. Manga, B. Morvan, A. Tinel, B. Dubus, J. Vasseur and A.-C. Hladky-Hennion, Negative refraction of longitudinal waves in a two-dimensional solid-solid phononic crystal, Phys. Rev. B, **83** 054301, (2011).

[93] S. Yang, J. H. Page, Z. Liu, M. L. Cowan, C. T. Chan and P. Sheng, Focusing of sound in a 3D phononic crystal, Phys. Rev. Lett., **93** 024301, (2004).

[94] F. Cervera, L. Sanchis, J. V. Sánchez-Pérez, R. Martínez-Sala, C. Rubio, F. Meseguer, C. López, D. Caballero and J. Sánchez-Dehesa, Refractive acoustic devices for airborne sound, Phys. Rev. Lett., **88** 023902, (2002).

[95] Z. Liu, X. Zhang, Y. Mao, Y. Y. Zhu, Z. Yang, C. T. Chan and P. Sheng, Locally resonant sonic materials, Science, **289** 1734, (2000).

[96] M. S. Kushwaha, P. Halevi, G. Martínez, L. Dobrzynski and B. Djafari-Rouhani, Theory of acoustic band structure of periodic elastic composites, Phys. Rev. B, **49** 2313, (1994).

[97] R. Martínez-Sala, J. Sancho, J. V. Sánchez, V. Gómez and J. Llinares, Sound attentuation by sculpture, Nature, **378** 241, (1995).

[98] G. Gubbiotti, S. Tacchi, M. Madami, G. Carlotti, A. O. Adeyeye and M. Kostylev, Brillouin light scattering studies of planar metallic magnonic crystals, J. Phys. D: Appl. Phys., **43** 264003, (2010).

[99] A. V. Chumak, P. Dhagat, A. Jander, A. A. Serga and B. Hillebrands, Reverse Doppler effect of magnons with negative group velocity scattered from a moving Bragg grating, Phys. Rev. B, **81** 140404(R), (2010).

[100] Yu. V. Gulyaev and S. A. Nikitov, Magnonic Crystals and spin waves in periodic structures, Doklady Physics, **46** 687, (2001).

[101] A. V. Chumak, A. A. Serga, S. Wollf, B. Hillebrands and M. P. Kostylev, Design and optimization of one-dimensional ferrite-film based magnonic crystals, J. Appl. Phys., **105** 083906, (2009).

[102] K.-S. Lee, D.-S. Han and S.-K. Kim, Physical origin and generic control of magnonic band gaps of dipole-exchange spin waves in width-modulated nanostrip waveguides, Phys. Rev. Lett., **102** 127202, (2009).

[103] A. V. Chumak, P. Pirro, A. A. Serga, M. P. Kostylev, R. L. Stamps, H. Schultheiss, K. Vogt, S. J. Hermsdoerfer, B. Laegel, P. A. Beck and B. Hillebrands, Spin-wave propagation in a microstructured magnonic crystal, Appl. Phys. Lett., **95** 262508, (2009).

[104] A. V. Chumak, A. A. Serga, S. Wollf, B. Hillebrands and M. P. Kostylev, Scattering of surface and volume spin waves in a magnonic crystal, Appl. Phys. Lett., **94** 172511, (2009).

[105] Z. K. Wang, V. L. Zhang, H. S. Lim, S. C. Ng, M. H. Kuok, S. Jain and A. O. Adeyeye, Observation of frequency band gaps in a one-dimensional nanostructured magnonic crystal, Appl. Phys. Lett., **94** 083112, (2009).

[106] A. V. Chumak, A. A. Serga, B. Hillebrands and M. P. Kostylev, Scattering of backward spin waves in a one-dimensional magnonic crystal, Appl. Phys. Lett., **93** 022508, (2008).

[107] Yu. V. Gulyaev, S. A. Nikitov, L. V. Zhivotovskii, A. A. Klimov, Ph. Tailhades, L. Presmanes, C. Bonningue, C. S. Tsai, S. L. Vysotskii and Yu. A. Filimonov, Ferromagnetic films with magnon bandgap periodic structures: magnon crystals, JETP Lett., **77** 567, (2003).

[108] J. P. Parekh and H.-S. Tuan, Reflection of magnetostatic forward volume waves by a shallow-grooves grating on a YIG film, IEEE Trans. Microw. Theory Tech., **26** 1039, (1978).

[109] C. G. Sykes, J. D. Adam and J. H. Collins, Magnetostatic wave propagation in a periodic structure, Appl. Phys. Lett., **29** 388, (1976).

[110] F. N. H. Robinson, Nuclear resonance absorption circuit, J. Sci. Instrum., **36** 481, (1959)

[111] A. D. Karenowska and J. F. Gregg, Position sensor, UK Pat. GB2435518, Appl. (2006), (granted 2009 with international derivatives pending).

[112] A. D. Karenowska and J. F. Gregg, Mechanical oscillator (for applications in control, measurement, automation and spinmechatronics), UK Pat. Appl. No. GB0900747.7, (2009) and PCT Appl. PCT/GB2010/000061, (2010).

[113] A. D. Karenowska, J. F. Gregg and C.-C. Coussios, Acoustic oscillator, UK Pat. Appl. No. GB0900745.1, (2009) and PCT Appl. PCT/GB2010/000069, (2010).

[114] A. D. Karenowska and J. F. Gregg, Delay-line self-oscillator, UK Pat. Appl. No. GB0900746.9, (2009) and PCT Appl. PCT/GB2010/000068, (2010).

[115] A. D. Karenowska and J. F. Gregg, Remote sensor device, UK Pat. Appl. No. GB0900744.4, (2009) and PCT Appl. PCT/GB2010/000065, (2010).

[116] A. Pikovsky, M. Rosenblum and J, Kirths, *Synchronization: A universal concept in nonlinear sciences* (Cambridge Univ. Press, Cambridge, 2001).

[117] A. B. Ustinov, B. A. Kalinikos, V. E. Demidov and S. O. Demokritov, Generation of dense spin-wave soliton trains in active ring resonators, Phys. Rev. B, **80** 052405, (2009).

[118] M. Wu and C. E. Patton, Experimental observation of Fermi-Pasta-Ulam recurrence in a nonlinear feedback ring system, Phys. Rev. Lett., **98** 047202, (2007).

[119] S. O. Demokritov, A. A. Serga, V. E. Demidov, B. Hillebrands, M. P. Kostylev and B. A. Kalinikos, Experimental observation of symmetry-breaking nonlinear modes in an active ring, Nature, **426** 159, (2003).

[120] A. A. Serga, M. P. Kostylev and B. Hillebrands, Formation of guided spin-wave bullets in ferrimagnetic film stripes, Phys. Rev. Lett., **101** 137204, (2008).

[121] A. D. Karenowska, A. V. Chumak, A. A. Serga, J. F. Gregg and B. Hillebrands, Employing magnonic crystals to dictate the characteristics of auto-oscillatory spin-wave systems, J. Phys.: Conf. Ser., **303** 012007, (2011).

[122] A. D. Karenowska, A. V. Chumak, A. A. Serga, J. F. Gregg and B. Hillebrands, Magnonic crystal based forced dominant wavenumber selection in a spin-wave active ring, Appl. Phys. Lett., **96** 082505, (2010).

[123] See for example, P. C. W. Davis, *The Physics of Time Asymmetry* (Univ. California Press, California, ed. 2, 1976), Introduction.

[124] M. F. Yanik and S. Fan, Time reversal of light with linear optics and modulators, Phys. Rev. Lett., **93** 173903, (2004).

[125] See for example, Ya. B. Zel'dovich, N. F. Pilipetsky and V. V. Shkunov, *Principles of Phase Conjugation* (Springer-Verlag, Berlin, 1985).

[126] A. Korpel and M. Chatterjee, Nonlinear echoes, phase conjugation, time reversal, and electronic holography, Proc IEEE, **69** 1539, (1981).

[127] E.G. Sauter, *Nonlinear Optics* (Wiley, New York, 2006).

[128] S. Sandhu, M. L. Povinelli and S. Fan, Stopping and time reversing a light pulse using dynamic loss tuning of coupled-resonator delay lines, Opt. Lett., **32** 3333, (2004).

[129] E. J. Reed, M. Soljačić and J. D. Joannopoulos, Color of shock waves in photonic crystals, Phys. Rev. Lett., **90** 203904, (2003).

[130] J. Bravo-Abad and M. Soljačić, Photonic crystals go dynamic, Nature Mater., **6** 799, (2007).

[131] Y. Tanaka, J. Upham, T. Nagashima, T. Sugiya, T. Asano and S. Noda, Dynamic control of the Q factor in a photonic crystal nanocavity, Nature Mater., **6** 862, (2007).

[132] M. Notomi and S. Mitsugi, Wavelength conversion via dynamic refractive index tuning of a cavity, Phys. Rev. A, **73** 051803(R), (2006).

[133] Z. Gaburro, Photon energy lifter, Opt. Express, **14** 7270, (2006).

[134] S. Longhi, Stopping and time reversal of light in dynamic photonic structures via Bloch oscillations, Phys. Rev. E, **75** 026606, (2007).

[135] A. Khorshidahmad and A. G. Kirk, Wavelength conversion by interband transition in a double heterostructure photonic crystal cavity, Opt. Lett., **34** 3035, (2009).

[136] See for example, I. G. Main, *Vibrations and Waves in Physics* (Cambridge Univ. Press, Cambridge, ed. 2, 1984), Ch. 8.

[137] A. D. Karenowska, V. S. Tiberkevich, A. V. Chumak, A. A. Serga, J. F. Gregg, A. N. Slavin and B. Hillebrands, Oscillatory energy exchange between waves coupled by a dynamic artificial crystal, Phys. Rev. Lett., *forthcoming.*